Modeling of the magnetoelectric properties of anisotropic transition metal oxides

Ahmed Al Baalbaky

▶ **To cite this version:**

Ahmed Al Baalbaky. Modeling of the magnetoelectric properties of anisotropic transition metal oxides. Materials. Normandie Université, 2017. English. NNT : 2017NORMR095 . tel-01735031

HAL Id: tel-01735031
https://theses.hal.science/tel-01735031

Submitted on 15 Mar 2018

HAL is a multi-disciplinary open access archive for the deposit and dissemination of scientific research documents, whether they are published or not. The documents may come from teaching and research institutions in France or abroad, or from public or private research centers.

L'archive ouverte pluridisciplinaire **HAL**, est destinée au dépôt et à la diffusion de documents scientifiques de niveau recherche, publiés ou non, émanant des établissements d'enseignement et de recherche français ou étrangers, des laboratoires publics ou privés.

Normandie Université

THÈSE

Pour obtenir le diplôme de doctorat

Spécialité SCIENCES DES MATÉRIAUX

Préparée au sein de l'Université de Rouen-Normandie

Modélisation des propriétés magnéto-électriques d'oxydes de métaux de transition anisotropes

Présentée et soutenue par

Ahmed AL BAALBAKY

Thèse soutenue publiquement le 21/12/2017 devant le jury composé de		
M. Jean-Marc Grenèche	Directeur de recherches CNRS, Université du Maine	Rapporteur
M. Christophe Chatelain	Maître de conférences-HDR, Université de Lorraine	Rapporteur
M. Ivan Labaye	Maître de conférences, Université du Maine	Examinateur
Mme Sylvie Hébert	Directrice de recherches CNRS, ENSICAEN	Examinatrice
M. Raymond Frésard	Professeur, ENSICAEN	Examinateur
M. Denis Ledue	Professeur, Université de Rouen-Normandie	Directeur de thèse

Thèse dirigée par Denis Ledue, laboratoire GPM, CNRS.

UNIVERSITÉ DE ROUEN NORMANDIE

ED PSIME

GPM Groupe de Physique des Matériaux

UNIVERSITÉ DE ROUEN-NORMANDIE

ÉCOLE DOCTORALE PSIME

Physique, Sciences de l'Ingénieur, Matériaux, Energie

THÈSE

pour obtenir le grade de

Docteur de l'Université de Rouen-Normandie

Discipline : PHYSIQUE

Spécialité : SCIENCES DES MATÉRIAUX

Présentée et soutenue publiquement le 21-12-2017 par

Ahmed AL BAALBAKY

Modélisation des propriétés magnéto-électriques d'oxydes de métaux de transition anisotropes

Thèse dirigée par Denis LEDUE

Version finale

Membres du Jury :

M. Jean-Marc GRENÈCHE	Directeur de recherches CNRS, Université du Maine	Rapporteur
M. Christophe CHATELAIN	Maître de conférences-HDR, Université de Lorraine	Rapporteur
M. Ivan LABAYE	Maître de conférences, Université du Maine	Examinateur
Mme Sylvie HÉBERT	Directrice de recherches CNRS, ENSICAEN	Examinatrice
M. Raymond FRÉSARD	Professeur, ENSICAEN	Examinateur
M. Denis LEDUE	Professeur, Université de Rouen-Normandie	Directeur de thèse

Author's declaration

I declare that the work in this dissertation was carried out in accordance with the requirements of the University's Regulations and Code of Practice for Research Degree Programs and that it has not been submitted for any other academic award. Except where indicated by a specific reference in the text, the work is my own work. Work done by the aid of a collaborator is indicated. Any views expressed in this dissertation are those of the author.

DATE: .....

SIGNED: .....

Acknowledgements

First of all, I would like to offer my gratitude to my thesis director, Prof. Denis Ledue, for his valuable discussions and the time he spent to learn me many bases in magnetism as well as in Monte Carlo simulations during the past three years. Also I would like to thank him for correcting the manuscript and for his valuable suggestions which improved the quality of this thesis.

I am very grateful to Mr. Renaud Patte for his important contribution in all the programming part of my work and for his excellent experience in solving the different programming problems that I faced.

I offer my gratitude to our collaborator Yaroslav Kvashnin who has a very important contribution in this work through his DFT calculations. Of course I'm very thankful to Dr. Nader Yaacoub because this nice DFT collaboration was done through his scientific acquaintances.

I would like to thank Dr. Jean-Marc Grenèche and Dr. Christophe Chatelain for accepting reviewing this work and providing me with their valuable suggestions and remarks. Also I thank Dr. Sylvie Hébert, Dr. Ivan Labaye and Prof. Raymond Frésard for accepting to participate in the jury of my defense and providing me with their very interesting discussions.

I also offer my gratitude to the Centre Régional Informatique et d'Applications Numériques de Normandie (CRIANN) for giving me the opportunity to access their computational resources and to perform all the simulations presented in this work.

Of course I would like to thank the project LABEX EMC3 for their financial support which was the basis to accomplish this work.

Finally, I would like to thank my family, my friends and all the members of GPM.

Contents

List of Figures

List of Tables

Abbreviations

TM	**T**ransition **M**etal
2D	**T**wo **D**imensional
3D	**T**hree **D**imensional
FM	**F**erro**M**agnetic
AFM	**A**nti**F**erro**M**agnetic
DFT	**D**ensity **F**unctional **T**heory
MC	**M**onte **C**arlo
GS	**G**round **S**tate
ME	**M**agneto**E**lectric
DM	**D**zyaloshinskii-**M**oriya
FC	**F**ield-**C**ooled
ZFC	**Z**ero-**F**ield-**C**ooled
w.r.t	**w**ith **r**espect **t**o

Physical Constants

Boltzmann constant	k_B	$=$	0.08617342	$\mathrm{meV/K}$
Bohr magneton	μ_B	$=$	0.05788381066	$\mathrm{meV/T}$
Vacuum permeability	μ_0	$=$	$4\pi \times 10^{-7}$	$\mathrm{T.m/A}$
Landé factor	g	$=$	2	

Symbols

a	lattice parameter	$(\mathring{A})$
c	lattice parameter	$(\mathring{A})$
T	Temperature	(K)
J	Exchange interaction	(meV)
E	Energy	(meV)
m	Magnetic moment	(μ_B/atom)
$\vec{B}$	Magnetic field	(T)
$\vec{E}$	Electric field	$(\mathrm{V/m})$
S	Spin	
P	Polarization	
χ	Linear magnetic susceptibility	

Introduction

Multiferroics represent an appealing class of multifunctional materials that simultaneously exhibit several ferroic orders such as ferroelectricity, ferromagnetism and ferroelasticity. The class of these multiferroics is also extended to include antiferroic orders such as antiferroelectricity and antiferromagnetism. They are considered as multifunctional materials because they possess physical properties that are useful in applications. The importance of these multifunctional materials is the existence of a cross-coupling between the magnetic and electric orders, termed magnetoelectric coupling. This coupling enables the control of the ferroelectricity by magnetic fields and also the tuning of magnetization by electric fields. Such magnetoelectric coupling is very important for device applications such as storing information in non-volatile memories. It has been argued that the presence of electrons in the d-orbitals in some transition metal oxides (favorable for magnetism) inhibits hybridization with the p-orbitals of the surrounding oxygen-anions and thus a cation displacement (necessary for ferroelectricty). On the other hand, a ferroelectric material has to be a good insulator so that mobile charges do not neutralize ferroelectric polarization, but most ferromagnets are said to be conductor. Thus it is not obvious to find ferroelectric-magnets which present a direct magnetoelectric coupling. However, it was found that the transition metal oxide $\mathrm{CuCrO_2}$ has a strong magnetoelectric coupling which attracts a lot of researchers attentions in the last few years. $\mathrm{CuCrO_2}$ with the delafossite structure is considered as a prototype quasi two dimensional antiferromagnetic triangular lattice. It is a p-type transparent semiconductor which exhibits high electric conductivity as well as thermoelectric properties.

In this fundamental work, we investigate the magnetoelectric properties of $\mathrm{CuCrO_2}$ by means of Monte Carlo simulations and *ab initio* calculations. The validity of the

results presented in this thesis was verified through their qualitative agreements with the experimental measurements.

This thesis consists of four chapters organized as follows

- Chapter 1 is devoted to give a brief background on magnetism as well as descriptions about the multiferroic $\mathrm{CuCrO_2}$ and what is done in literature on this system.
- Chapter 2 describes the principle of Monte Carlo method and the physical models used in our simulations.
- Chapter 3 is divided into two main parts. The first part presents the DFT calculations that estimate the values of the exchange interactions and single ion anisotropy constants in $\mathrm{CuCrO_2}$. The second part shows our Monte Carlo simulation results of the magnetic and ferroelectric properties in $\mathrm{CuCrO_2}$ based on the extracted DFT parameters.
- Chapter 4 presents the Monte Carlo simulation results of the effect of magnetic dilution on the magnetoelectric properties of $\mathrm{CuCr_{1-x}Ga_xO_2}$ $(0 \leq x \leq 0.3)$.
- Finally, we sum up the main results presented in this dissertation in a general conclusion, ending with some perspectives that could be done on this system.

CHAPTER 1

Generalities

Transition metal oxides are compounds composed of oxygen atoms bound to transition metals. They are commonly used for catalytic activities and semiconductors. In particular, the transition metal oxide $\mathrm{CuCrO_2}$ has recently received a lot of attention after the discovery of its p-type transparent conductivity and magnetically driven ferroelectricity controlled by an applied magnetic field. This chapter is devoted to a general overview about some physical bases in magnetism. Then we present detailed explanations about $\mathrm{CuCrO_2}$ and its magnetic and ferroelectric properties.

1.1 Background

Materials are said to be magnetic if they have a response to an applied external magnetic field. The origin of magnetism in these materials lies in the orbital and spin momentum of electrons. Magnetism can be divided into two main groups. The first group consists of magnetic materials where there is no interaction between their magnetic moments known as paramagnets and diamagnets. The second group includes magnetic materials like ferromagnets, antiferromagnets, ferrimagnets, speromagnets, sperimagnets ... in which their magnetic moments are coupled to each others. This coupling is known as the exchange interaction and is rooted to the overlap of electrons orbitals in conjunction with Pauli's exclusion principle. Whether it is a ferromagnet, antiferromagnet or ferrimagnet, exchange interactions order the individual moments with their neighboring atoms below

a certain temperature called the critical temperature. This ordering is parallel in ferromagnetic materials, producing a net non-zero magnetization below the critical temperature called *Curie temperature* T_C. However, in the case of antiferromagnetism, the ordered magnetic moments give a net zero magnetization below the critical temperature termed *Néel temperature* T_N.

1.1.1 Magnetic moment

By definition, the magnetic moment $(\vec{m})$ is a vector quantity which results from the motion of the electric charge (orbital angular momentum $\vec{L}$) and the spin angular momentum $(\vec{S})$ defined as

$$\vec{m} = -g_J \mu_B \vec{J} \tag{1.1}$$

where g_J is the Landé factor, μ_B is the Bohr magneton and $\vec{J}$ being the total angular momentum defined by

$$\vec{J} = \vec{L} + \vec{S} \tag{1.2}$$

In transition metal (TM) oxides such as $\mathrm{CuCrO_2}$, the orbital angular momentum for the $3d$ $\mathrm{Cr^{3+}}$ ions is quenched $\left(\langle \vec{L} \rangle = \vec{0}\right)$, and therefore the magnetic moment of each magnetic ion is

$$\vec{m} = -g_s \mu_B \vec{S} \tag{1.3}$$

with $g_s (\equiv g) = 2$.

1.1.2 Magnetic interactions

The magnetic energy is divided into different contributions such as exchange energy E_{ex}, dipolar interaction energy E_{dip}, anisotropic energy E_a, and Zeeman energy E_Z associated to an applied external magnetic field. Thus globally, total energy E_{tot} can be written as

$$E_{tot} = E_{ex} + E_{dip} + E_a + E_Z \tag{1.4}$$

In the following, we will define each contribution of this energy.

1.1.2.1 Exchange interactions

Exchange interactions are the couplings responsible for the magnetic ordering below the critical temperature in a magnetic material. Such interactions directly enter into competition with the thermal agitation. Above the critical temperature (T_C or T_N), the effect of temperature becomes more important than any order imposed by the effect of these interactions and therefore the magnetic ordering is lost (paramagnetic state). Exchange interactions exist in different mechanisms depending on the material under consideration (metals differ from insulators). The most important mechanisms are explained below.

Direct exchange interaction (Metals)

Direct exchange interaction arises from a direct overlap of the electronic wave functions of the neighboring atoms (ions) in metals. It gives a strong but short range coupling which decreases rapidly as the ions are separated.

RKKY interaction (Metals)

RKKY interaction named after Ruderman, Kittel, Kasuya and Yosida [1–3] is an indirect exchange interaction which couples magnetic moments over relatively large distances. It is the dominant exchange interaction in rare-earth metals where there is little or no direct overlap between the wave functions of the neighboring electrons. In this case, the interaction between two magnetic moments is mediated by the polarization of the conduction electrons.

Super-exchange interaction (Insulators)

Super-exchange or Kramers-Anderson super-exchange interaction [4] is an another form of the indirect exchange interaction which is dominant in insulators especially in TM oxides. It describes the interaction between magnetic cations of the same charge that are far from each other to be connected by a direct exchange interaction, but coupled over a larger distance through a non-magnetic anion. Accordingly, in the present study of the TM oxide $\mathrm{CuCrO_2}$, all the exchange interactions are of the super-exchange type taking place between $\mathrm{Cr^{3+}}$ ions through the intermediary non-magnetic oxygen and copper ions.

Let $\vec{S}_i$ and $\vec{S}_j$ be the spins of two neighboring magnetic atoms i and j, then the exchange energy can be expressed as

$$E_{ex} = -\sum_{\langle i,j \rangle} J_{ij} \vec{S}_i \cdot \vec{S}_j \tag{1.5}$$

with J_{ij} stands for the exchange interaction between interacting spins $\vec{S}_i$ and $\vec{S}_j$. $J_{ij} > 0$ indicates a ferromagnetic interaction, which tends to align the spins parallel; $J_{ij} < 0$ indicates an antiferromagnetic interaction, which tends to align the spins anti-parallel. Eq. (1.5) is known as the Heisenberg Hamiltonian if $\vec{S}_i$ and $\vec{S}_j$ are 3D vectors.

Dzyaloshinskii-Moriya exchange interaction (Insulators)

Some antiferromagnetic materials possess a lowering symmetry (inversion symmetry breaking) resulting from a canted magnetic ordering below T_N. Such symmetry breaking leads to an additional kind of exchange interaction called the *Dzyaloshinskii-Moriya* (DM) interaction or the *antisymmetric exchange* interaction [5]. This antisymmetric DM interaction is the relativistic correction of the usual super-exchange interactions and its strength is proportional to the spin-orbit coupling. The energy contribution of this interaction can be expressed as

$$E_{DM} = -\sum_{\langle i,j \rangle} \vec{D}_{ij} \cdot (\vec{S}_i \times \vec{S}_j) \tag{1.6}$$

with $\vec{D}_{ij}$ being the DM interaction vector as shown in Fig. 1.1. This energy is minimized when $\vec{S}_i$ is perpendicular to $\vec{S}_j$ within a plane perpendicular to $\vec{D}_{ij}$. Thus this antisymmetric exchange interaction favors canted spin structures. Such interaction is important for understanding the mechanism of induced electric polarization in the recently discovered classes of multiferroics.

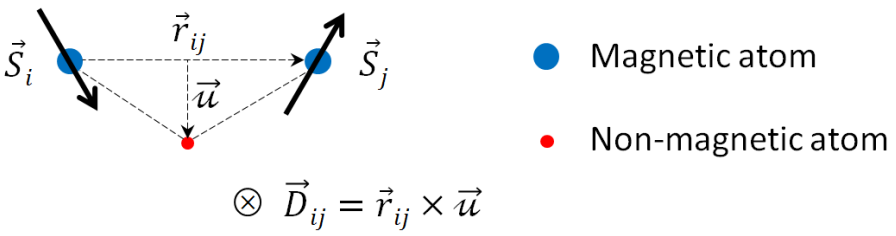

FIG. 1.1. Schematic illustration of the DM interaction.

Biquadratic exchange interaction (Insulators)

This is another type of the indirect exchange interaction that generally exists in rare-earths and considered to be a correction term to the super-exchange interaction when extending the calculations of Kramers [6] from third to fifth-order perturbation theory as proposed by Anderson [4, 7]. Its energy contribution can be represented by

$$E_{Biq} = -\beta \sum_{\langle i,j \rangle} \left(\vec{S}_i \cdot \vec{S}_j \right)^2 \tag{1.7}$$

with β being the strength of the biquadratic term.

1.1.2.2 Dipolar interaction

Considering two magnetic moments $\vec{m}_i$ and $\vec{m}_j$ separated by a distance r_{ij} as shown in Fig. 1.2, their dipolar energy can be expressed as

$$E_{ij} = \frac{\mu_0}{4\pi r_{ij}^3} \left(\vec{m}_i \cdot \vec{m}_j - \frac{3}{r_{ij}^2} \left(\vec{m}_i \cdot \vec{r}_{ij} \right) \left(\vec{m}_j \cdot \vec{r}_{ij} \right) \right). \tag{1.8}$$

Such energy pair is minimized when both $\vec{m}_i$ and $\vec{m}_j$ are aligned parallel to each others along the direction of $\vec{r}_{ij}$. However for an ensemble of magnetic dipoles, dipolar interaction induces frustration in the system because it is not possible to satisfy all the energy pairs. Note that dipolar interaction is small between two magnetic moments of few μ_B compared to the exchange energy — like in our case of $CuCrO_2$: $m_{Cr^{3+}} = 3\mu_B$ — and can be neglected. However, it becomes more important between ferromagnetic nanoparticles owning magnetic moments of $10^3 - 10^5$ μ_B.

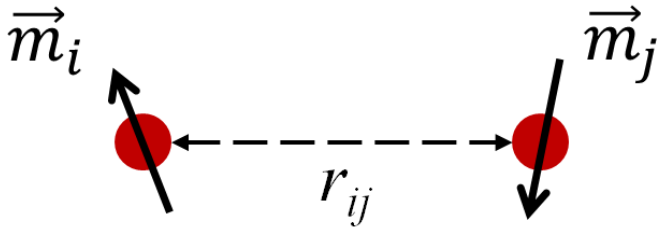

FIG. 1.2. Schematic representation of the dipolar interaction between two magnetic dipoles $\vec{m}_i$ and $\vec{m}_j$ separated by a distance r_{ij}.

1.1.2.3 Magnetic anisotropy

Magnetic anisotropy is the direction dependence of the magnetic energy. The magnetic moments of magnetically anisotropic materials will tend to align along an easy axis, which is an energetically favorable direction. In bulk materials, the magnetic anisotropy is a resultant of magnetocrystalline anisotropy, magnetoelastic anisotropy and the shape anisotropy in ferromagnets.

Magnetocrystalline anisotropy

Magnetocrystalline anisotropy results from the spin-orbit coupling and the crystal field interaction. One of the forms of the magnetocrystalline anisotropy is the single ion anisotropy. The single ion contribution is essentially due to the electrostatic interaction of the orbital state of a magnetic ion and the surrounding crystalline field which is very strong. The crystal field interaction tends to stabilize particular orbitals and is transferred to the spin moments via the spin-orbit coupling which tends to align the magnetic moments along a particular crystallographic direction. For a uniaxial crystal with an easy axis anisotropy along the z direction (or the c direction), the single ion anisotropic energy is defined as

$$E_a = -D_z \sum_i S_z^2 \tag{1.9}$$

with D_z is the single ion anisotropy constant.

Magnetocrystalline anisotropy has a great influence on industrial uses of ferromagnetic materials. Materials with high magnetocrystalline anisotropy usually have high coercivity; i.e., they are hard to demagnetize. These are called ”hard” ferromagnetic materials, and are used to make permanent magnets. Single-ion anisotropy is the major source of magnetocrystalline anisotropy in hard ferromagnetic materials. On the other hand, materials with low magnetocrystalline anisotropy usually have low coercivity, and hence their magnetization can be easily changed. These materials are called ”soft” ferromagnets used to make magnetic cores for transformers and inductors. In general, the anisotropic energy found in TM bulk compounds is dominated by the magnetocrystalline anisotropy [8].

Magnetoelastic anisotropy

Magnetoelastic energy results from magnetostriction, i.e., a deformation in the crystal along a certain direction. If the lattice is changed by a strain [9], the distances between the magnetic atoms are modified and hence the interaction energies are different. This produces magnetoelastic anisotropy. Such lattice deformation can be due to magnetic interactions in a given material and thus magnetic and elastic properties depend on each other. Consider a crystal under a certain strain σ. The magnetostriction constant or the magnetoelastic coupling constant, λ, is defined along the deformation direction. Then, the magnetoelastic energy per unit volume is given by

$$E_\sigma = -\frac{3}{2}\lambda\sigma\sin^2\theta \tag{1.10}$$

with θ being the angle between the magnetization direction and the strain direction. The magnetoelastic energy is said to be zero in non-deformed lattices.

1.1.2.4 Zeeman energy

Zeeman energy is the energy of the magnetic moments under the effect of an applied external magnetic field $\vec{B}$ which is expressed as

$$E_Z = -\vec{B}\cdot\sum_i \vec{m}_i \tag{1.11}$$

where it tends to align the magnetic moments along its direction.

1.1.3 Geometric magnetic frustration

Magnetic frustration exists in a magnetic material when all the magnetic interactions cannot be fully satisfied. It requires antiferromagnetic exchange interactions to exist. There are several ways in which magnetic frustration can arise. When it arises purely from the geometry of the lattice, it is then called geometric magnetic frustration. Such kind of magnetic frustration is mainly found in TM oxides which crystallize in certain lattices which are prone to frustration due to their topologies such as triangular lattices or tetrahedra with shared corners, edges or faces. A simple example that can explain

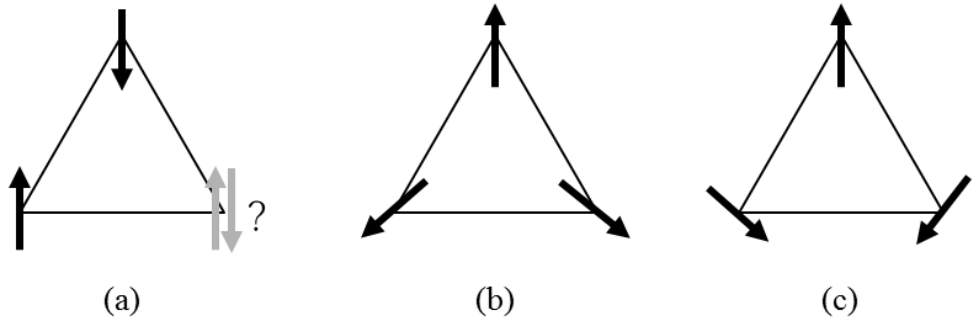

FIG. 1.3. Geometric magnetic frustration arising from triangular arrangement of magnetic moments coupled antiferromagnetically (a), two degenerate ground states 120° (b) and 240° (c).

this phenomenon is a triangular plaquette as shown in Fig. 1.3a. Three magnetic ions are located at the corners of the triangle with antiferromagnetic interactions between them; the energy pair is minimized when each spin is aligned opposite to its neighbors. Once the first two spins align anti-parallel, the third spin cannot simultaneously be anti-parallel with the two other spins. Consequently, it is impossible to find a minimal energy state in which all the interactions are fully satisfied. Then the spins will tend to organize themselves in a minimal energy state where the antiferromagnetic interactions are not fully satisfied. Such minimal energy state is not unique, frustration usually increases the degeneracy of the ground state (GS) giving rise to different physics. In such triangular lattices, the frustrated spin configuration possesses a minimal energy state that corresponds to two degenerate states of 120° (Fig. 1.3b) and 240° (Fig. 1.3c). In order to measure the degree of geometric magnetic frustration, one can define a parameter F written as

$$F = 1 - \frac{E_{GS}}{E_{min}} \tag{1.12}$$

where E_{GS} is the energy of the GS and E_{min} is the magnetic energy if all the exchange interactions can be fully satisfied, and is given by

$$E_{min} = -\frac{1}{2}S^2 \left(z_1|J_1| + z_2|J_2| + z_3|J_3| + 2|D_z|\right) \tag{1.13}$$

with z_1, z_2 and z_3 are the numbers of first, second and third nearest neighbors, respectively. In the non-frustrated systems, $E_{GS} = E_{min}$ and therefore $F = 0$ while $E_{GS} > E_{min}$ in frustrated systems which yields to $F > 0$. $F \longrightarrow 1$ reflects the fact that the magnetic

configuration of a given system is highly frustrated.

1.1.4 Antiferromagnetic triangular lattices

The Heisenberg antiferromagnet on a triangular lattice is one of the prototype examples of frustrated magnetic systems which has been studied for several decades. The magnetic properties of the triangular antiferromagnetic lattice with an easy axis anisotropy can be described through the following Hamiltonian

$$H = -\sum_{\langle i,j \rangle} J_{ij} \vec{S}_i \cdot \vec{S}_j - D_z \sum_i (S_i^z)^2 \tag{1.14}$$

where $D_z > 0$ is the single ion anisotropy constant for an easy axis along the z axis.
In the presence of applied external magnetic fields, the system exhibits a rich magnetic phase diagram consisting of exotic phases [10]. At low temperatures, successive magnetic phase transitions occur as the applied magnetic field is increased.

1.1.4.1 Ground state magnetic configuration without anisotropy

A magnetic configuration can be commensurate or incommensurate with respect to the crystal periodicity. An incommensurate magnetic configuration is a non periodic magnetic structure unlike a commensurate one. In general, a magnetic configuration is defined by a propagation vector $\vec{q} = (h, k, l)$ expressed in the reciprocal lattice which can be determined by neutron diffraction experiments. The magnetic moment can be expressed as function of $\vec{q}$ through the following relation [11]

$$\vec{m}_\ell = \vec{\mathrm{A}} \exp(i\vec{q} \cdot \vec{R}_\ell) \tag{1.15}$$

with $\vec{A}$ being a complex vector and $\vec{R}_\ell$ is the position of $\vec{m}_\ell$ in the lattice.
Since $\vec{m}_\ell$ is real, Eq. (1.15) can be expressed as

$$m_\ell^\alpha = \lambda_\alpha \cos(\vec{q} \cdot \vec{R}_\ell - \varphi_\alpha) \qquad (\alpha = x, y, z) \tag{1.16}$$

It can be shown that, in helimagnetic structures, all the magnetic moments lie in the same plane known as the spiral plane. In our case of $CuCrO_2$, a hard axis anisotropy exists along the x axis ($[110]$ direction) and consequently the yz plane is the spiral plane, and therefore we can write

$$\begin{cases} m_\ell^x = 0 \\ m_\ell^y = \lambda_y \sin(\vec{q}\cdot\vec{R}_\ell) \\ m_\ell^z = \lambda_z \cos(\vec{q}\cdot\vec{R}_\ell - \varphi) \end{cases} \tag{1.17}$$

And since all magnetic moments have the same magnitude, we can write

$$\left|\vec{m}(\vec{R}_\ell)\right|^2 = \left|\vec{m}(-\vec{R}_\ell)\right|^2 = \left|\vec{m}(\vec{0})\right|^2 \tag{1.18}$$

which gives

$$\lambda_y^2 \sin^2(\vec{q}\cdot\vec{R}_\ell) + \lambda_z^2 \cos^2(\vec{q}\cdot\vec{R}_\ell - \varphi) = \lambda_y^2 \sin^2(\vec{q}\cdot\vec{R}_\ell) + \lambda_z^2 \cos^2(\vec{q}\cdot\vec{R}_\ell + \varphi) = \lambda_z^2 \cos^2(\varphi) \tag{1.19}$$

This provides

$$\sin(2\vec{q}\cdot\vec{R}_\ell)\sin(2\varphi) = 0 \tag{1.20}$$

But $\vec{q}\cdot\vec{R}_\ell$ can take any value whatever the vector R_ℓ. Then we remain with $\sin(2\varphi) = 0 \implies \varphi = 0$ and $\lambda_y = \lambda_z = m$ and consequently the solution in the helimagnetic structure can be written as

$$\begin{cases} m_\ell^x = 0 \\ m_\ell^y = m \sin(\vec{q}\cdot\vec{R}_\ell) \\ m_\ell^z = m \cos(\vec{q}\cdot\vec{R}_\ell) \end{cases} \tag{1.21}$$

Now, in the triangular antiferromagnet $CuCrO_2$, the propagation vector is found to be along the $[110]$ direction such that $h = k$ and $l = 0$ [12–16] providing that $\vec{q} = (k, k, 0)$. Thus it is very important to provide an analytical verification of these observations $(h = k)$ before proceeding in further explanations. Consider a magnetic configuration with a propagation vector $\vec{q} = (h, k, 0)$ propagating along the $[110]$ direction as shown in Fig. 1.4. Let us start with the simple case with only first nearest neighbor exchange

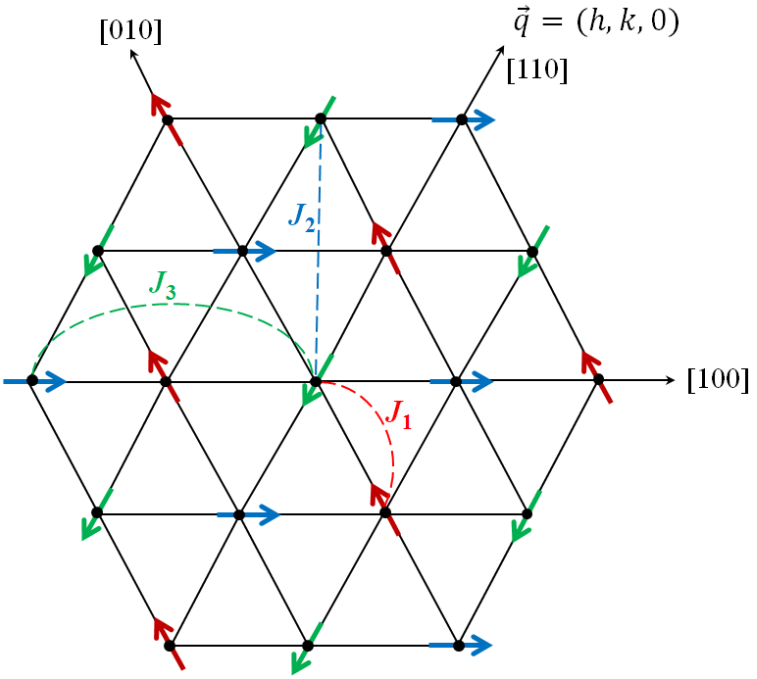

FIG. 1.4. Schematic representation of the triangular antiferromagnet $CuCrO_2$ illustrating a commensurate spin configuration represented in the ab plane with a propagation vector $\vec{q} = (1/3, 1/3, 0)$ taking into account isotropic exchange interactions up to the 3^{rd} nearest neighbors.

interaction J_1. The exchange energy per spin due to the first nearest neighbors is then written as

$$E_{ex}(h,k) = -S^2 \left\{ J_1 \cos(2\pi h) + J_1 \cos(2\pi k) + J_1 \cos\left(2\pi(h+k)\right) \right\} \tag{1.22}$$

Thus the minimization of Eq. (1.22) w.r.t h and k gives

$$\begin{cases} \dfrac{\partial E_{ex}(h,k)}{\partial h} = 0 & \Longrightarrow J_1 \sin\left(2\pi(h+k)\right) + J_1 \sin\left(2\pi h\right) = 0 \quad (1.23) \\ \dfrac{\partial E_{ex}(h,k)}{\partial k} = 0 & \Longrightarrow J_1 \sin\left(2\pi(h+k)\right) + J_1 \sin\left(2\pi k\right) = 0 \quad (1.24) \end{cases}$$

Subtracting Eq. (1.24) from Eq. (1.23) gives

$$\sin(2\pi h) = \sin(2\pi k) \tag{1.25}$$

which means that either

$$h = k \tag{1.26}$$

or

$$2\pi h = \pi - 2\pi k \Longrightarrow h + k = \frac{1}{2} \tag{1.27}$$

Therefore replacing Eq. (1.27) in Eq. (1.23) and Eq. (1.24) gives

$$\begin{cases} \sin(2\pi h) = 0 & \Longrightarrow h = n/2 \text{ with } n \in \mathbb{Z} \quad (1.28) \\ \sin(2\pi k) = 0 & \Longrightarrow k = m/2 \text{ with } m \in \mathbb{Z} \quad (1.29) \end{cases}$$

which is valid if and only if $h = 0$ and $k = 0.5$ or vice versa with h and $k \in [0, 1[$. However, this solution corresponds to a maximum in the $E_{ex}(h, k)$ curve which cannot refer to one of the ground states in triangular lattices. Therefore the only possible solution which minimizes Eq. (1.22) is when $h = k$ and hence $\vec{q} = (k, k, 0)$. Hence, by replacing $h = k$ in Eq. (1.23) we obtain: $\cos(2\pi k) = -1/2 \Longrightarrow k = 1/3$ or $k = 2/3$ which correspond to the $120°$ and the $240°$ configurations shown in Fig. 1.3b and Fig. 1.3c. Therefore, assuming that this formalism holds true for small J_2 and J_3, we can express the GS exchange energy per spin due to the first, second and third nearest neighbors as a function of $\vec{q} = (k, k, 0)$ in the following expression

$$\begin{aligned} E_{ex}(k) \;=\; & -S^2[2J_1\cos(2\pi k) + J_1\cos(4\pi k) + 2J_2\cos(6\pi k) + J_2 \\ & + 2J_3\cos(4\pi k) + J_3\cos(8\pi k)] \end{aligned} \tag{1.30}$$

where J_1, J_2 and J_3 are the isotropic exchange interactions up to the 3^{rd} nearest neighbors as illustrated in Fig. 1.4.

1.1.4.2 Energy of the $120°$ GS configuration with a uniaxial anisotropy

It was shown that the GS configuration of an antiferromagnetic triangular magnet in the Heisenberg model is the degenerate $120°$ (or $240°$) structure with three magnetic sublattices [17] as shown in Fig. 1.5a. For three dimensional vector spins and isotropic exchange interactions, the degeneracy of the $120°$ GS configuration is infinity because these three sublattices can freely rotate within the spiral plane of the system. However, if the Hamiltonian has an easy axis anisotropy, the spiral plane will contain this easy axis and therefore the degeneracy of the $120°$ GS configuration decreases. Then if we assume that one of the three sublattices, $\vec{S}_1$, is making an angle θ with the easy axis (z axis) as

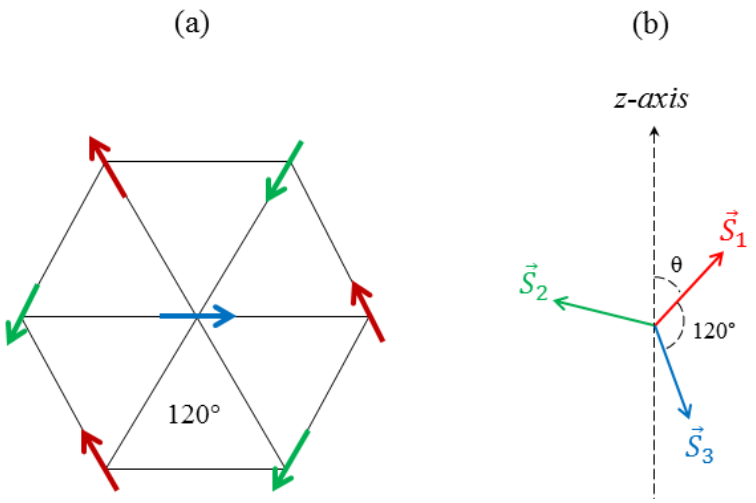

FIG. 1.5. Antiferromagnetic triangular lattice with 120° ground state configuration.

seen in Fig. 1.5b, then $\vec{S}_2$ makes an angle $120^\circ - \theta$ and $\vec{S}_3$ makes an angle $120^\circ + \theta$ with the z axis. Hence, the anisotropic energy for the three spins can be expressed as

$$E_a = -D_z \left((S_1^z)^2 + (S_2^z)^2 + (S_3^z)^2 \right) \tag{1.31}$$

with $S_1^z = S\cos\theta$, $S_2^z = S\cos(120^\circ - \theta)$ and $S_3^z = S\cos(120^\circ + \theta)$. Then

$$E_a = -D_z S^2 \left(\cos^2\theta + \cos^2(120^\circ - \theta) + \cos^2(120^\circ + \theta) \right) = -\frac{3}{2} D_z S^2 \tag{1.32}$$

which is independent of θ. Therefore, in the perfect 120° configuration, the spins can still rotate freely in a spiral plane containing the easy axis without constraints that one sublattice should follow this easy axis. Then in this case, i.e. $k = 1/3$, Eq. (1.30) is now written as

$$E_{120^\circ} = S^2 \left(\frac{3}{2} J_1 - 3J_2 + \frac{3}{2} J_3 - \frac{1}{2} D_z \right) \tag{1.33}$$

1.1.5 Curie-Weiss law

In paramagnetic materials, the magnetization (M) is only induced under the effect of an applied magnetic field $(\vec{B})$. If B is small enough, then M is approximately proportional to B. For a given value of B, M is inversely proportional to the temperature (T) of the system. Such behavior is illustrated in Fig. 1.6 and is described by the Curie law given

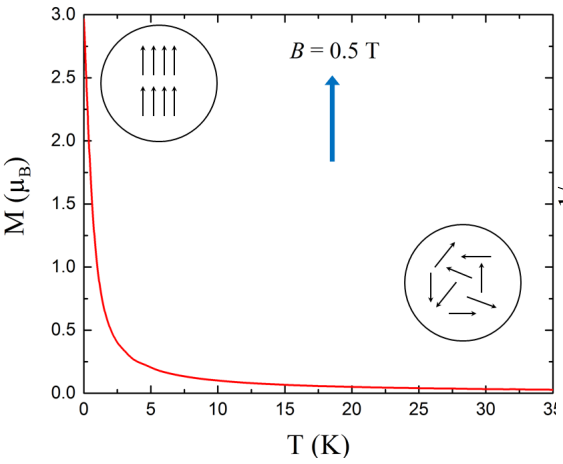

FIG. 1.6. Thermal variation of the magnetization in paramagnetic materials.

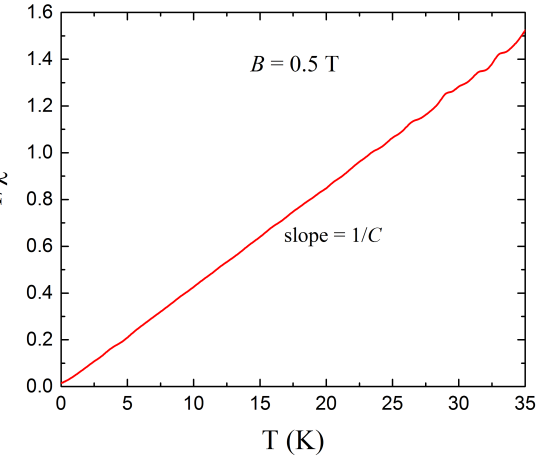

FIG. 1.7. Thermal variation of the inverse magnetic susceptibility in paramagnetic materials.

by

$$M = C\,\frac{H}{T} \qquad (\text{with H} = \text{B}/\mu_0) \tag{1.34}$$

where C is the Curie constant given as

$$C = \frac{\mu_0 N m_{eff}^2}{3k_B} \tag{1.35}$$

with N being the number of magnetic moments per unit volume, μ_0 is the vacuum permeability, k_B is the Boltzmann constant and $m_{eff} = g_J \mu_B \sqrt{J(J+1)}$ is the effective magnetic moment.

By definition, the linear magnetic susceptibility is given by

$$\chi = \left(\frac{\partial M}{\partial H}\right)_{H=0} \tag{1.36}$$

which is equal to M/H when H is sufficiently small and $M(H=0) = 0$. Therefore the paramagnetic linear susceptibility is written as

$$\chi = \frac{C}{T} \qquad (\text{Curie law}) \tag{1.37}$$

The plot of $1/\chi$ versus temperature is linear as shown in Fig. 1.7. From such a plot we can extract the characteristic properties of the system such as the effective magnetic moment per atom. However, in ferromagnetic, antiferromagnetic or ferrimagnetic materials $1/\chi$

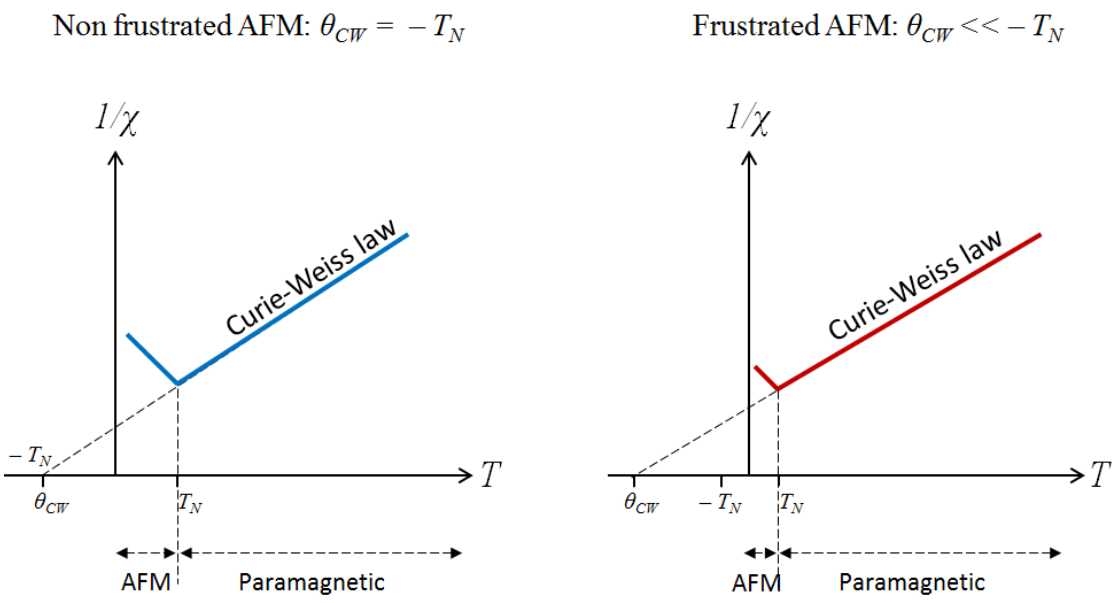

FIG. 1.8. Schematic illustration of the thermal variation of the inverse magnetic susceptibility in antiferromagnetic materials: the left hand side corresponds to a non-frustrated AFM system with $\theta_{CW} = -T_N$ and the right hand side corresponds to a frustrated AFM system with $\theta_{CW} \ll -T_N$.

deviates from such linear behavior due to the spin ordering that takes place below the critical temperature (T_C or T_N). In these materials, the system becomes paramagnetic above T_C or T_N and obeys the Curie-Weiss law given by

$$\chi = \frac{C}{T - \theta_{CW}} \tag{1.38}$$

where θ_{CW} is known as the Curie-Weiss temperature. According to the molecular field theory, $\theta_{CW} = T_C$ in ferromagnetic materials. However, $\theta_{CW} = -T_N$ in non-frustrated antiferromagnets while $\theta_{CW} < -T_N$ in frustrated antiferromagnets as illustrated in Fig. 1.8. Therefore, in a frustrated antiferromagnetic system, $|\theta_{CW}|/T_N > 1$ and increases as much as the frustration increases. According to Refs. [17, 18], one can consider $f = |\theta_{CW}|/T_N$ as a frustration parameter that gives complementary information about the frustrated nature of the system.

Let us now determine the relation between θ_{CW} and the exchange interactions. Consider a frustrated antiferromagnet with 3 sublattices as shown in Fig. 1.4 denoted by A, B and C. According to the molecular field theory [19, 20], the molecular fields acting on each

sublattice can be written as

$$\begin{aligned} H_A^i &= n_{AA}M_A + n_{AB}M_B + n_{AC}M_C + H \\ H_B^i &= n_{BA}M_A + n_{BB}M_B + n_{BC}M_C + H \\ H_C^i &= n_{CA}M_A + n_{CB}M_B + n_{CC}M_C + H \end{aligned} \tag{1.39}$$

where $n_{AA} = n_{BB} = n_{CC} = n_{intra} > 0$ and $n_{AB} = n_{BA} = n_{AC} = n_{CA} = n_{BC} = n_{CB} = n_{inter} < 0$ are the intrasublattice and intersublattice molecular field constants, respectively, and H is an applied magnetic field. In the paramagnetic region above T_N and under small H, $M_\alpha = \chi H_\alpha^i$ with $\chi = C'/T$ such that $C' = \mu_0(N/3)m_{eff}^2/3k_B = C/3$. Hence we get

$$\begin{aligned} M_A &= (C'/T)(n_{intra}M_A + n_{inter}M_B + n_{inter}M_C + H) \\ M_B &= (C'/T)(n_{inter}M_A + n_{intra}M_B + n_{inter}M_C + H) \\ M_C &= (C'/T)(n_{inter}M_A + n_{inter}M_B + n_{intra}M_C + H) \end{aligned} \tag{1.40}$$

The condition for the appearance of a spontaneous sublattice magnetization is that these equations have a nonzero solution when $H = 0$. This means that the determinant of the system (1.40) must be zero. This yields to

$$\frac{C'}{T} = \frac{1}{n_{intra} - n_{inter}} \tag{1.41}$$

and consequently $T_N = C'(n_{intra} - n_{inter})$. The paramagnetic linear susceptibility above T_N is evaluated by Eq. (1.37) where $M = M_A + M_B + M_C$. By solving Eq. (1.40), i.e. by making $(M_A - M_B)$ and $(M_B - M_C)$, we get $M_A = M_B = M_C$. Therefore Eq. (1.37) becomes

$$\chi = \frac{3M_A}{H} \tag{1.42}$$

However, by substituting $M_A = M_B = M_C$ in the equation of M_A in (1.40) we obtain

$$M_A = \frac{C'}{T - C'(n_{intra} + 2n_{inter})} \tag{1.43}$$

Hence Eq. (1.42) becomes

$$\chi = \frac{C}{T - C'(n_{intra} + 2n_{inter})} \tag{1.44}$$

Therefore by the analogy of Eq. (1.44) with Eq. (1.38) we obtain the theoretical value of the Curie-Weiss temperature written as

$$\theta_{CW} = C'(n_{intra} + 2n_{inter}) = \frac{C}{3}(n_{intra} + 2n_{inter}) \tag{1.45}$$

It is important to note that the molecular field constants, n_{intra} and n_{inter}, can be related to the Heisenberg super-exchange interaction J through the following formula [20]

$$n_{intra}, n_{inter} = \frac{zJ}{\mu_0(N/3)g^2\mu_B^2} \tag{1.46}$$

where z is the number of nearest neighbor interactions. In our case of $CuCrO_2$, Fig. 1.4 shows that n_{intra} results from the 6 second neighbors and n_{inter} results from 3 first neighbor interacting spins and 3 third neighbor interacting spins. Hence

$$\begin{aligned} n_{intra} &= \frac{6J_2}{\mu_0 N g^2 \mu_B^2} = \frac{J_2}{C}\frac{2S(S+1)}{k_B} \\ n_{inter} &= \frac{3J_1 + 3J_3}{\mu_0 N g^2 \mu_B^2} = \frac{J_1 + J_3}{C}\frac{S(S+1)}{k_B} \end{aligned} \tag{1.47}$$

Therefore, Eq. (1.45) becomes

$$\theta_{CW} = \frac{2S(S+1)}{k_B}(J_1 + J_2 + J_3) \tag{1.48}$$

1.1.6 A brief overview of spin glasses

Detailed explanations on spin glasses can be found in Refs. [21–23].

A spin glass is a disordered frustrated magnet, where its magnetic moments are localized and not ordered in a regular pattern so that no long range order can be established. Nevertheless these compounds are characterized by a spin glass freezing temperature denoted by T_{SG} which refers to a kind of a second order phase transition from a paramagnetic phase to a freezing

phase where all the spins freeze into random directions. This freezing state is characterized by a very slow equilibration after perturbation and a high dependency on its magnetic history. Magnetic configurations in spin glasses below T_{SG} are out-off-equilibrium configurations known as "metastable" states because they are "stuck" in stable configurations other than the lowest-energy configuration which makes them infinitely degenerate. Spin glass magnets can be classified into metallic and insulating spin glasses according to their conduction properties. Till now, there is neither a unique experiment nor a solvable analytical realistic model which are able definitely to identify a sample as a spin glass. Thus before classifying any material as a spin glass, it is very important to know several characteristic properties that should exist. Basically, two important and necessary ingredients should coexist: frustration and disorder. Additionally, many other features should be seen like:

(i) A clear sharp peak in the linear a.c. susceptibility $(\chi_{a.c.})$ curve under very small magnetic fields indicating the spin glass freezing temperature T_{SG}.

(ii) No magnetic Bragg peaks can be seen in neutron diffraction spectrum. That means the freezing state below T_{SG} is accompanied with no long-range ordering.

(iii) No clear cusp at T_{SG} in the magnetic specific heat curve, however a broad peak exists at $T \simeq (1.2 - 1.3)T_{SG}$.

(iv) Severe magnetic history dependence below T_{SG} in the magnetization measurements (discussed below).

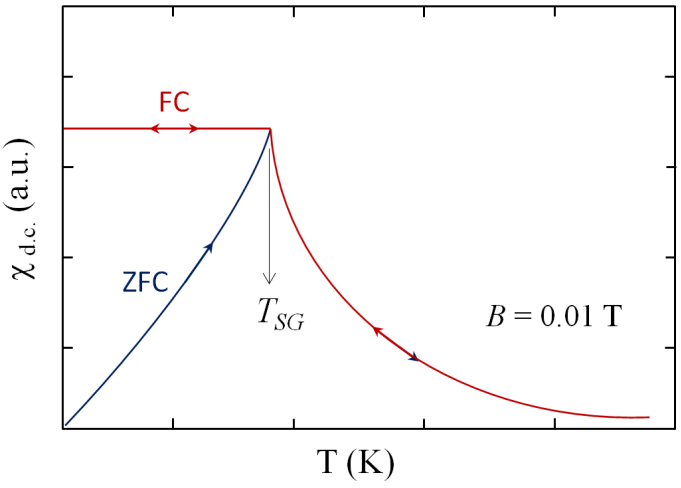

FIG. 1.9. Schematic representation of the thermal variation of the d.c. *ZFC-FC* magnetic susceptibility measured in a spin glass showing the freezing temperature T_{SG}.

The most two commonly used thermomagnetic histories are the *zero-field-cooled (ZFC)* and the *field-cooled (FC)* measurements. The procedure of the *ZFC-FC* measurements goes as follows: the sample is cooled down from an initial state at $T > T_{SG}$ to a measuring temperature $T' < T_{SG}$, then the sample is heated starting from T' under a small applied magnetic field to a given temperature $T'' > T_{SG}$ in which the *ZFC* magnetic measurements $(M, \chi \dots)$ are collected during the heating process. Now, starting from the magnetic configuration obtained at T'', the system is then cooled down to T' under the same magnetic field where the *FC* magnetic measurements are collected during the cooling process. The spin glass d.c. susceptibility deduced from these measurements in a low magnetic field is illustrated Fig. 1.9. It can be seen that *ZFC*-$\chi_{d.c.}$ differs from *FC*-$\chi_{d.c.}$ below T_{SG}, and that *FC*-$\chi_{d.c.}$ is reversible while heating and cooling the sample whereas *ZFC*-$\chi_{d.c.}$ is not. Such irreversibility provides potentially useful information on the low temperature properties of spin glasses. T_{SG} can be identified by the cusp observed in the *ZFC*-$\chi_{d.c.}$ plot, and plenty metastable states below T_{SG} are expected to exist.

1.1.7 Dielectric polarization

Dielectrics are materials that have no free charges; i.e., all electrons are localized and associated to the nearest atoms. When a dielectric is subjected to an external electric field, its molecules or atoms gain electric dipole moments due to the separation of the center of gravity of the positive and negative electrical charges within the system. Each electric dipole moment is proportional to the applied electric field such as

$$\vec{p} = \alpha \vec{E} \tag{1.49}$$

where α is called the polarizability factor. As a consequence of the polarity gained by the dielectric

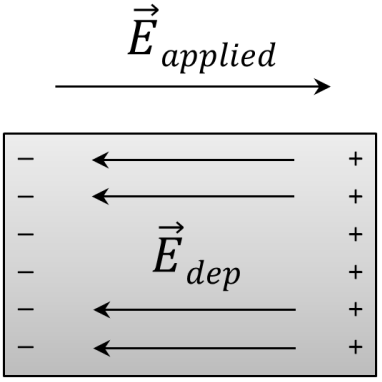

FIG. 1.10. Schematic representation of a dielectric subjected to an applied electric field.

due to the applied electric field ($\vec{E}_{applied}$), an induced dipole field called the depolarizing field ($\vec{E}_{dep}$) that opposes the applied field is created at each dipole moment (see Fig. 1.10). The type of the induced dielectric polarization on the microscopic scale is determined by the dielectric itself. Dielectrics can be classified in two types: polar dielectrics and non-polar dielectrics. Polar dielectrics are materials that possess permanent dipole moments which are randomly oriented, but under the effect of an applied $\vec{E}$-field these electric dipole moments become more oriented thus inducing a net spontaneous dielectric polarization. Non-polar dielectrics are materials that possess electric dipole moments only when subjected to external electric fields.

1.1.8 Multiferroics

More details on multiferroics can be found in Ref. [24–29]

Multiferroics are materials that exhibit magnetoelectric (ME) properties in the same phase. In other words, when there exists a magnetic response to an electric field or an electric response to a magnetic field (Fig. 1.11), the material is said to be a multiferroic. In general, multiferroics can be divided into two classes as introduced by D. Khomskii [30]. Class-I of the multiferroic family is older and numerous. It consists of multiferroics possessing distinct magnetic and ferroelectric transition temperatures where they can be well above the room temperature such as in $BiFeO_3$ ($T_{FE} \approx 1100$ K and $T_N \approx 643$ K) [27, 30]. However, the coupling between magnetism and ferroelectricity is weak in these materials. Class-II of multiferroics also termed magnetic multiferroics, has been recently discovered and is more interesting than class-I. It consists of materials in which ferroelectricity emerges only in the magnetically ordered state – i.e. the ordering temperature of the ferroelectric phase coincides with that of the magnetic

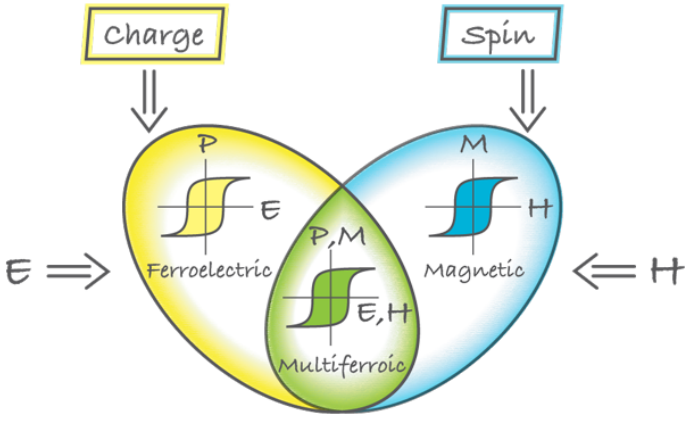

FIG. 1.11. Schematic illustration of the magnetic and electric responses in ferromagnetic, ferroelectric and multiferroic materials [30].

phase – and is caused by a particular type of magnetism [31, 32]. Many multiferroics are transition metal oxides of the spiral type and mostly belong to class-II. Spiral magnetic ordering in dielectrics is mainly caused by magnetic frustration leading to having frustrated multiferroics of class-II [30]. Boracites were the first well known multiferroics [33, 34], and soon several other multiferroics were either found in nature or synthesized artificially [35]. Cr_2O_3 was also a typical example of multiferroics which shows fascinating ME properties [36–38]; an electric field induces macroscopic magnetization (ferromagnetism) [39] and a magnetic field generates macroscopic electric polarization (ferroelectricity) [40]. However, its ME properties were not sufficient to be used for applications in magnetic memory devices for example. Since the discovery of Cr_2O_3, many other compounds have been discovered to exhibit multiferroic properties such as $TbMnO_3$ [31].

1.2 About the transition metal oxide $CuCrO_2$

1.2.1 The delafossite structure

Delafossite minerals of general formula ABO_2 is a group characterized by a sheet of linearly coordinated A cations stacked between edge-shared octahedral layers BO_6 as shown in Fig.1.12. Delafossite group has been recognized for its electrical properties from insulation to metallic conduction. Materials with this crystal structure generally have high p-type conductivity because of the low formation energy of Cu vacancies which are hole producing defects [41]. Through the discovery of the $CuFeO_2$ mineral in 1873, Friedel opened the door to the delafossites ABO_2 [42–45]. Such a family crystallizes in the layered $R\bar{3}m$ space group (Fig. 1.12). For instance, for A in a d^9 configuration, e.g., A = Pd or Pt, highly metallic compounds with anomalous temperature dependence of the resistivity have been reported [46–49]. Moreover, the discovery of simultaneous transparency and p-type conductivity in $CuAlO_2$ by Kawazoe *et al.* [50], laid ground for the development of transparent optoelectronic devices. Furthermore, depending on the chemical composition, a plethora of behaviors can be evidenced. The diversity of properties they exhibit raises up an ever increasing interest in this class of compounds. The transport in these compounds has been found to be strongly anisotropic, with a degree of anisotropy that may reach 10^3 [46, 47, 51]. For A in a d^{10} configuration, the semi-conducting materials $CuBO_2$, with B = Cr, Fe, Rh, may be turned into promising thermoelectric ones through hole doping [52, 53] – in particular, an especially high power factor has been found in $CuRh_{1-x}Mg_xO_2$

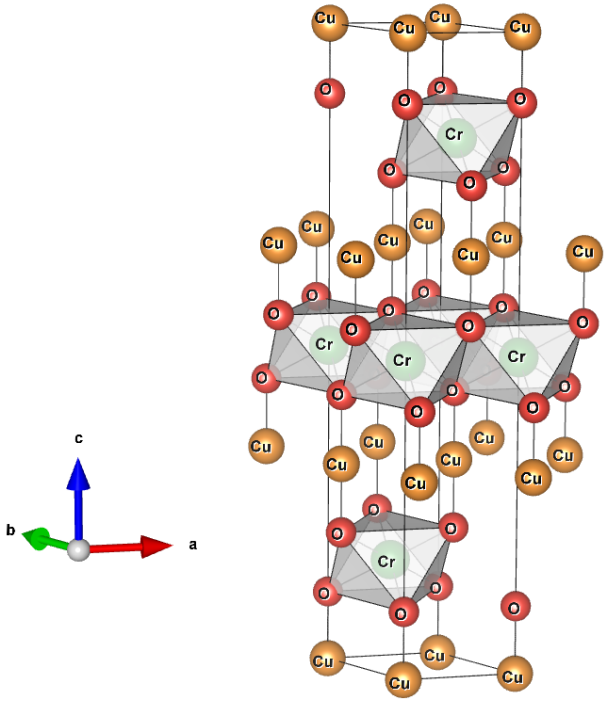

FIG. 1.12. Delafossite structure of ABO_2 with A = Cu^{+} and B = Cr^{3+}.

[54], which transport coefficients served as a basis for the Apparent Fermi Liquid scenario [55]. Regarding the magnetic compounds $CuFeO_2$ and $CuCrO_2$, many studies point towards a strong coupling of the magnetic and structural degrees of freedom [12, 56–63] which pave the way to multiferroelectricity.

1.2.2 Exchange interactions in $CuCrO_2$

1.2.2.1 Validity of proposed sets of exchange interactions (literature)

Since $CuCrO_2$ is an antiferromagnet, thus obviously the first nearest neighbor exchange interaction (J_1) is negative. Looking for the second and third nearest neighbor in-plane exchange interactions, it is not obvious to predict their nature (FM or AFM). Frontzek *et al.* [64] proposed a set of exchange interactions for $CuCrO_2$ extracted from neutron diffraction (ND) experiments given in Table 1.1. He found that all the in-plane exchange interactions are antiferromagnetic such that $J_2/J_1 \approx 0.171$ and $J_3/J_1 \approx 0.029$. In order to know the minimal energy state that corresponds to this set of exchange interactions, we plot the variation of Eq. (1.30) as function of k as shown in the left side of Fig. 1.13. It is clear that the plot of $E_{ex}(k)$ exhibits a minimum at

TABLE 1.1. Estimated values of the in-plane exchange interactions in $CuCrO_2$ using neutron diffraction experiments and density functional theory calculations. The values are given in meV.

	J_1	J_2	J_3
ND	-2.8	-0.48	-0.08
DFT	-2.972	0.09	-0.163

$k = 1/2$ which corresponds to the 180° configuration of energy

$$E_{ex}^{180^\circ} = S^2 \left(J_1 + J_2 - 3J_3\right) \tag{1.50}$$

providing that $E_{ex}^{180^\circ} = -6.84$ meV. However, the energy of the 120° configuration corresponding to $k = 1/3$ is

$$E_{ex}^{120^\circ} = S^2 \left(\frac{3}{2}J_1 - 3J_2 + \frac{3}{2}J_3\right) \tag{1.51}$$

which gives $E_{ex}^{120^\circ} = -6.48$ meV $> E_{ex}^{180^\circ}$. Therefore we can say that the ND estimates of the exchange interactions cannot represent the real exchange interactions presented in $CuCrO_2$.

On the other hand, another estimates for the same exchange interactions using the density functional theory calculations were given in Ref. [63] (Table 1.1). It was found that J_2 is FM in nature while J_3 is AFM such that $J_2/J_1 \approx -0.030$ and $J_3/J_1 \approx 0.055$. The plot $E_{ex}(k)$ shows two minima at $k = 1/3$ and $k = 2/3$ (Fig. 1.13) which correspond to the 120° and to the 240° configurations of $CuCrO_2$. Then $E_{ex}^{120^\circ} = -11.19$ meV $< E_{ex}^{180^\circ} = -5.38$ meV. Therefore, we can say that the DFT set of exchange interactions can refer to the true exchange interactions

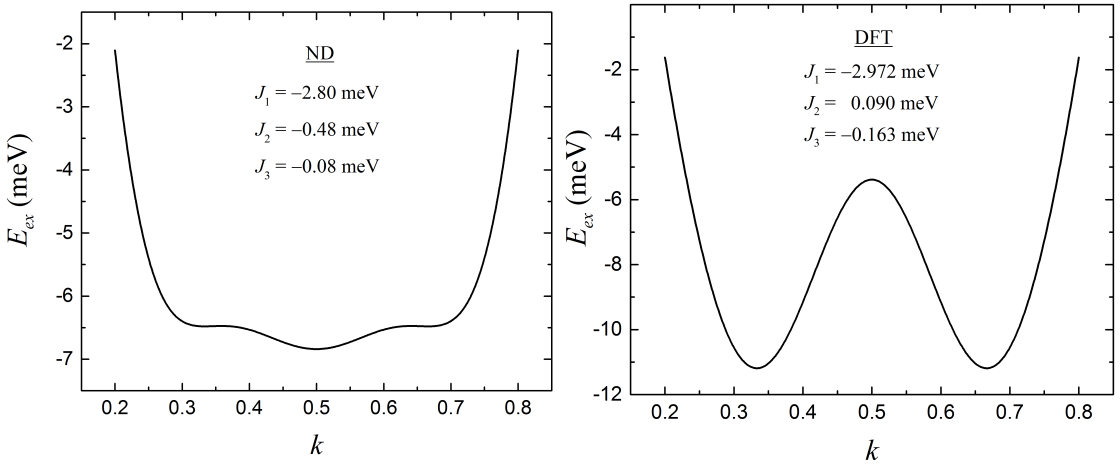

FIG. 1.13. Variation of the exchange energy as function of the propagation vector k for two sets of exchange interactions extracted from neutron diffraction experiments (left), and from DFT calculations (right) in $CuCrO_2$.

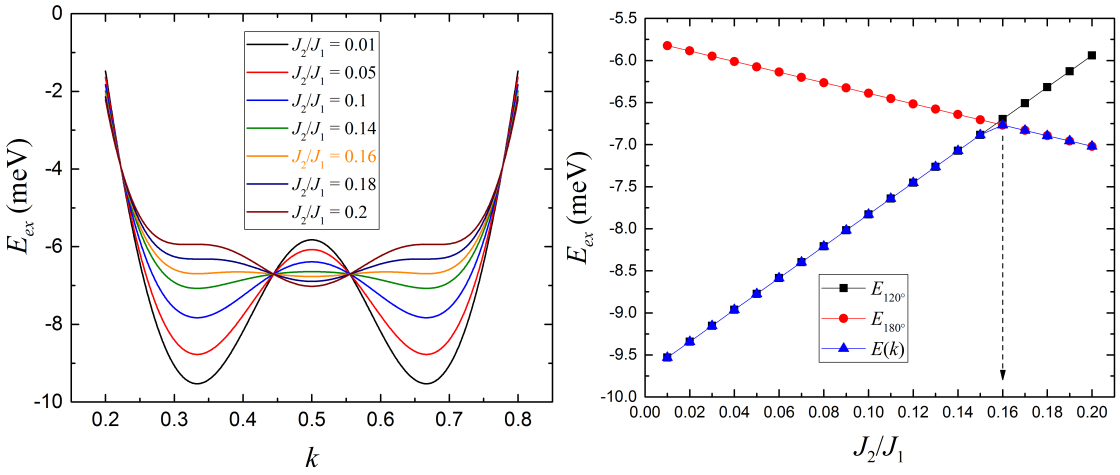

FIG. 1.14. Variation of the exchange energy as function of the propagation vector k for various rations of J_2/J_1 (left), and the variation of the minimal energy of $E_{ex}(k)$ versus J_2/J_1 for J_2 AFM compared to the theoretical energy of the $120°$ and the $180°$ (right) in $CuCrO_2$.

presented in $CuCrO_2$.

The question arises now is that, what is the true magnetic natures and order of magnitudes of J_2 and J_3 in this multiferroic? To answer that we minimize Eq. (1.30) for various values of J_2 and J_3 in both cases AFM and FM as shown below.

1.2.2.2 Nature and order of magnitude of J_2

Here we take the ND set of exchange interactions. We fix J_1 and J_3 and we make varying J_2/J_1 for J_2 being AFM and FM.

J_2 AFM

When J_2 is AFM, it can be seen that the $E_{ex}(k)$ plot exhibits two minima at $k = 1/3$ and $k = 2/3$ if $J_2/J_1 < 0.16$ as shown in the left side of Fig. 1.14. However when $J_2/J_1 \geq 0.16$, the $E_{ex}(k)$ plot possesses a minimum at $k = 1/2$ which means that the magnetic configuration does no more refer to the $120°$ configuration. For each value of J_2/J_1, we record the minimum energy of $E_{ex}(k)$ and we compare it to that calculated for $E_{ex}^{120°}$ and $E_{ex}^{180°}$. The variation of $E_{ex}(k)$, $E_{ex}^{120°}$ and $E_{ex}^{180°}$ versus J_2/J_1 is shown in the right side of Fig. 1.14.

It is clear that the GS configuration is the $120°$ whenever $J_2/J_1 < 0.16$. However when $J_2/J_1 \geq 0.16$, $E_{ex}(k)$ follows $E_{ex}^{180°}$ and thus the $120°$ GS configuration is broken and turns to become a colinear state.

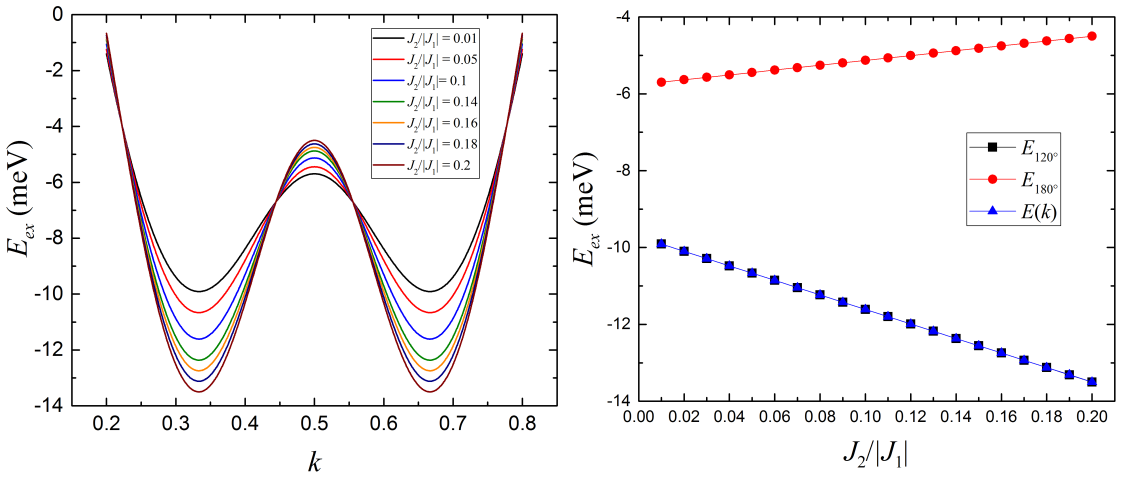

FIG. 1.15. Variation of the exchange energy as function of the propagation vector k for various rations of $J_2/|J_1|$ (left), and the variation of the minimal energy of $E_{ex}(k)$ versus $J_2/|J_1|$ for J_2 FM compared to the theoretical energy of the 120° and the 180° (right) in $CuCrO_2$.

J_2 FM

For the set of exchange interactions extracted from ND experiments, we now take J_2 FM and repeat the same previous calculations. It can be seen that whatever the ratio J_2/J_1, $E_{ex}(k)$ always has two minima at $k = 1/3$ and $k = 2/3$ (left side of Fig. 1.15) which means that the minimal energy state always refers to the 120° or 240° configurations. Moreover we can see that as much as J_2/J_1 increases, as much as $E_{ex}(k)$ decreases and follows $E_{ex}^{120°}$ (right side of Fig. 1.15) which means that the 120° GS configuration becomes more and more stable.

1.2.2.3 Nature and order of magnitude of J_3

Here, for the set of exchange interactions extracted from the DFT calculations, we fix J_1 and J_2 and we make varying J_3/J_1 for both cases J_3 AFM and FM.

J_3 AFM

When J_3 has an AFM nature, it can be seen that whatever the ratio J_3/J_1, $E_{ex}(k)$ always possesses two minima at $k = 1/3$ and $k = 2/3$ as shown in Fig. 1.16 (left side). This means that the minimal energy state always refers to the 120° or 240° configurations. Also Fig. 1.16 (right side) shows that as much as J_3/J_1 increases, as much as $E_{ex}(k)$ decreases and follows $E_{ex}^{120°}$ reflecting the fact that the AFM nature of J_3 stabilizes the 120° GS configuration.

J_3 FM

For a FM nature of J_3, we can see that $E_{ex}(k)$ has two minima at $k = 1/3$ and $k = 2/3$ if

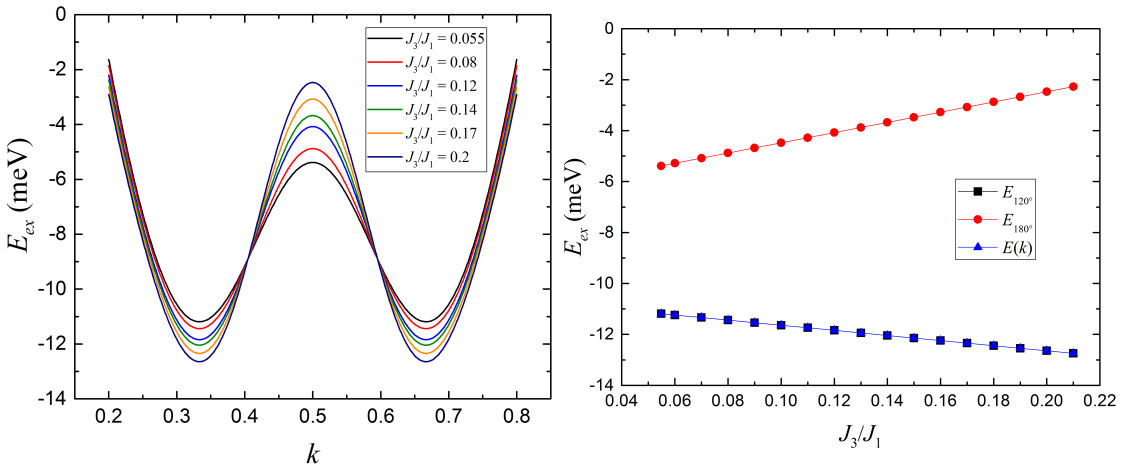

FIG. 1.16. Variation of the exchange energy as function of the propagation vector k for various rations of J_3/J_1 (left), and the variation of the minimal energy of $E_{ex}(k)$ versus J_3/J_1 for J_3 AFM compared to the theoretical energy of the $120°$ and the $180°$ (right) in $CuCrO_2$.

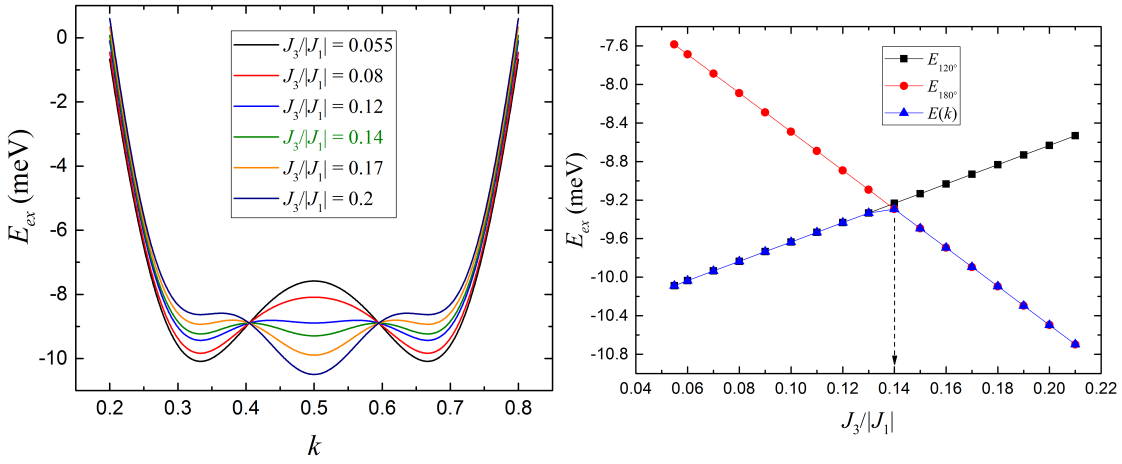

FIG. 1.17. Variation of the exchange energy as function of the propagation vector k for various rations of $J_3/|J_1|$ (left), and the variation of the minimal energy of $E_{ex}(k)$ versus $J_3/|J_1|$ for J_3 FM compared to the theoretical energy of the $120°$ and the $180°$ (right) in $CuCrO_2$.

$J_3/|J_1| < 0.14$ as shown in Fig. 1.17 (left side). When $J_3/|J_1| \geq 0.14$, $E_{ex}(k)$ possesses a single minimum located at $k = 1/2$. The variation of the minimum of $E_{ex}(k)$ versus $J_3/|J_1|$ is given in Fig. 1.17 (right side). It can be seen that $E_{ex}(k)$ coincides with $E_{ex}^{120°}$ whenever $J_3/|J_1| < 0.14$, but it deviates from it at $J_3/|J_1| = 0.14$ and then follows $E_{ex}^{180°}$. Then the FM nature of J_3 destabilizes the $120°$ GS configuration.

The zone of interactions where the $120°$ *configuration exists is schematically illustrated in Fig. 1.18. We conclude that the FM nature of* J_2 *and the AFM nature of* J_3 *stabilize the* $120°$ *GS configuration. However if* J_2 *is AFM, its value should be greater than* $-0.16|J_1|$ *otherwise the*

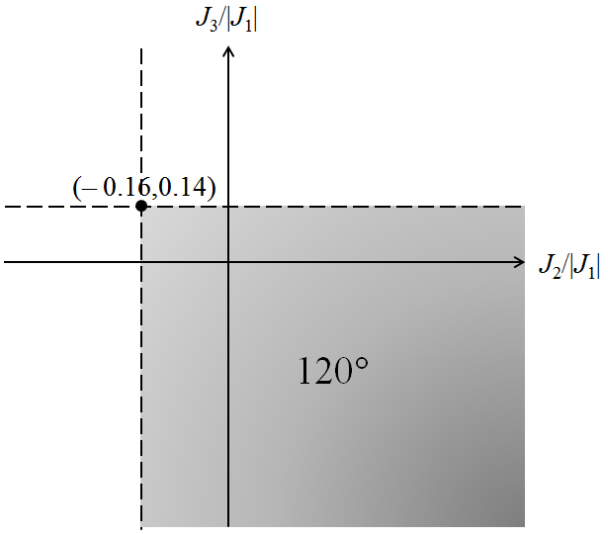

FIG. 1.18. Schematic representation of the zone of interactions where the 120° configuration persists in $CuCrO_2$.

120° *GS configuration is broken. Similarly if* J_3 *is FM, its value should be smaller than* $0.14|J_1|$ *otherwise the* 120° *GS configuration is broken. Due to this conflict in the estimated values of the exchange interactions and their magnetic natures, we look to estimate our own set of these interactions in the real crystal to provide a better understanding of the magnetic and ferroelectric properties of* $CuCrO_2$ *(chapter 3).*

1.2.3 Magnetoelectric properties of $CuCrO_2$

$CuCrO_2$ is a very good example of the spin-driven ferroelectricity. In this compound, ferroelectric polarization starts to appear just below the magnetic ordering temperature T_N [13, 65–67]. It was found that the magnetic ordering in single crystals of $CuCrO_2$ occurs in two stages with two transition temperatures $T_{N1} \approx 23.6$ K and $T_{N2} \approx 24.2$ K [14, 64, 65, 68]. These observations were described as follows: at T_{N2}, the system enters a 2D ordered antiferromagnetic collinear state, while a fully three dimensional magnetic ordering is achieved below T_{N1}. However, such scenario was contrary to other experimental studies [52, 66, 67] performed also on single crystals of $CuCrO_2$ where they showed that $CuCrO_2$ undergoes a single phase transition to an ordered antiferromagnetic proper-screw configuration at $T_N = 24 - 26$ K. Knowing that physical properties of single crystals are highly dependent on the nature of the defects (twin boundaries, dislocations, impurities) as well as on their concentrations [69–72], and based on the results of experimental studies performed on polycrystalline samples of $CuCrO_2$ [15, 52, 73] showing a unique T_N, it is more confident to believe that $CuCrO_2$ possesses a single magnetic phase

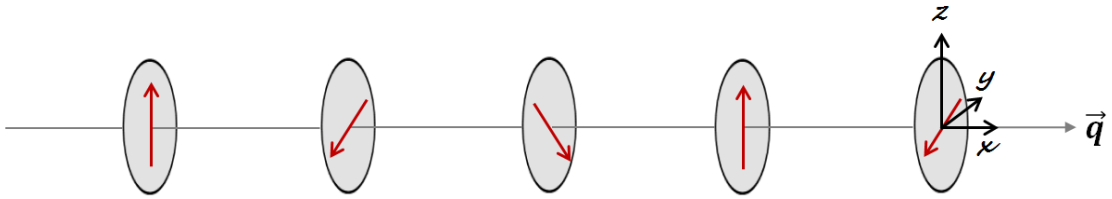

FIG. 1.19. Schematic representation of a proper-screw spin structure with its corresponding propagation vector $\vec{q}$.

transition.

Early neutron diffraction experiment [73] showed that the magnetic configuration of $CuCrO_2$ below the ordering temperature T_N is a proper-screw (Fig. 1.19) commensurate configuration with a propagation vector $\vec{q} = (1/3, 1/3, 0)$ pointing along the $[110]$ direction. However, recent neutron diffraction experiments [12–16] showed that the magnetic configuration of $CuCrO_2$ below T_N is a proper-screw with an incommensurate propagation vector $\vec{q} = (0.329, 0.329, 0)$ propagating along the $[110]$ direction. The origin of such incommensurability was discussed in Ref. [74] where they showed that the deviation from the commensurate configuration is due to a tiny in-plane lattice distortion that takes place below T_N along the $[110]$ direction. The equilateral triangular plaquettes with isotropic exchange interaction, J_1, above T_N (Fig. 1.20a) turned to

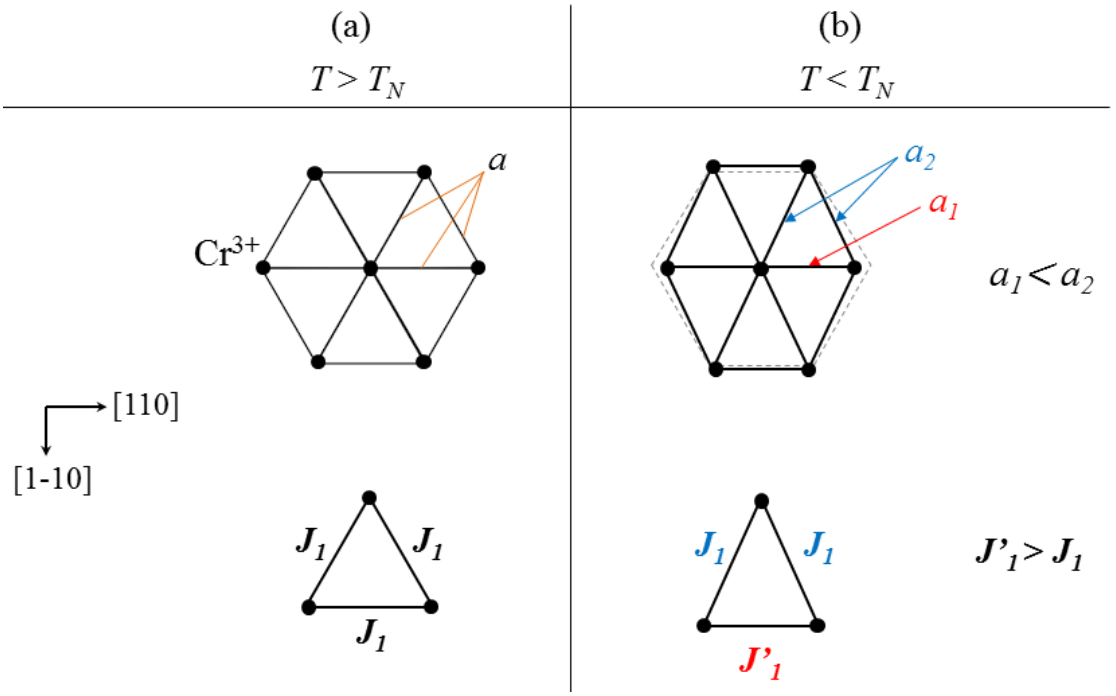

FIG. 1.20. Atomic plane of Cr^{3+} ions at $T > T_N$ with equilateral triangular plaquettes and isotropic exchange interaction J_1 (a), distorted atomic plane of Cr^{3+} ions below T_N with anisotropic first nearest-neighbor exchange interactions with $J_1/J'_1 < 1$ (b).

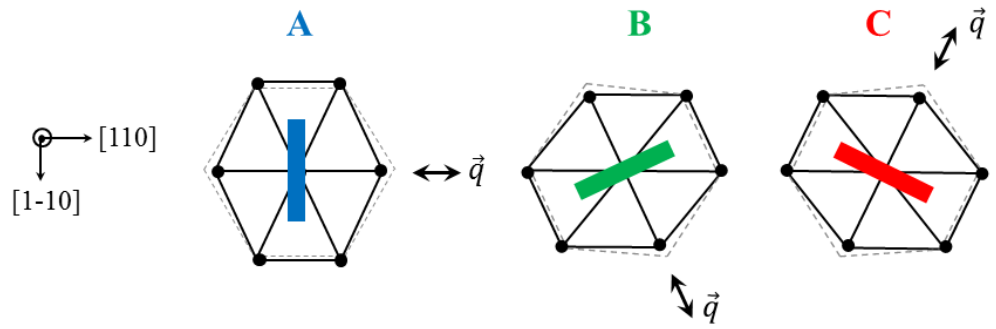

FIG. 1.21. Schematic representation of the three types of domains with different spiral planes in $CuCrO_2$ showing their corresponding propagation vector $\vec{q}$. Thick lines denote the spiral plane for the three degenerate domains A, B and C at zero fields.

become isosceles triangular plaquettes upon distortion below T_N leading to the appearance of distinct exchange interactions, J_1 and J_1', through the neighboring spins as illustrated in Fig. 1.20b. The fact of the appearance of the lattice distortion below T_N confirms its strong coupling with the spiral magnetic ordering in $CuCrO_2$ [74]. The question arises now is why the in-plane lattice distortion occurs. Two hypotheses may answer this question. First hypothesis suggests that spin-lattice coupling may force the lattice to distort slightly leading to high spin degeneracy [74]. Second hypothesis assumes that the present inter-plane interaction causes a slightly incommensurate structure which can be a driving force for the lattice distortion [75, 76]. Although these answers are still hypotheses and more detailed investigations are needed for further understanding.

Even though, the presence of the tiny in-plane lattice distortion doesn't totally break all the symmetry elements of the crystal [67]. The crystal still possesses a twofold rotation axis along the $\vec{q}$ direction and a threefold rotation axis along the c axis. The threefold symmetry allows the existence of three equivalent magnetic domains denoted by A, B and C as illustrated in Fig. 1.21. The remaining unbroken symmetry operation allows the appearance of ferroelectric polarization only along the perpendicular direction of each spiral plane.

1.3 Ferroelectricity induced by proper-screw and cycloid structures

Nowadays, the term *ME multiferroic* is used not only for ferromagnetic-ferroelectric materials, but also for ferroelectric with some other magnetic order such as antiferromagnets. In particular, ferroelectrics induced by spin ordering is very important in developing a novel ME phenomenon.

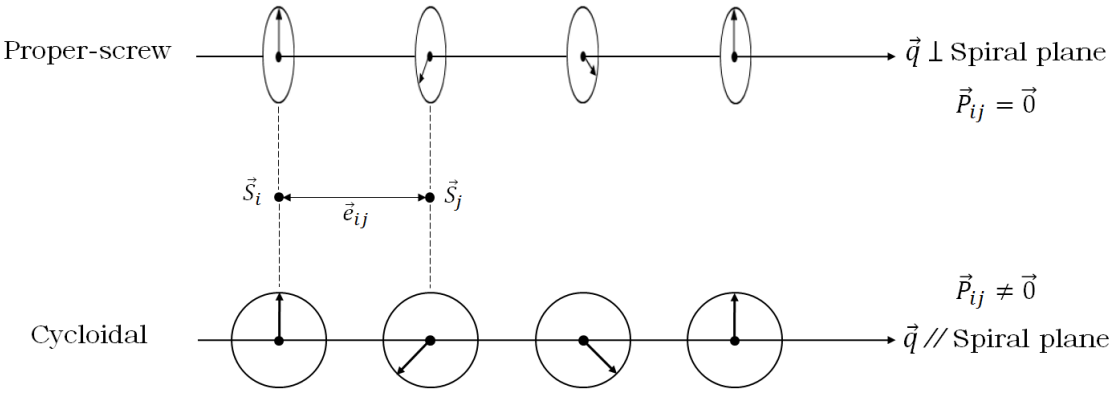

FIG. 1.22. Proper-screw spin configuration with $\vec{q}$ perpendicular to the spiral plane and cycloidal spin configuration with $\vec{q}$ inside the spiral plane.

From the microscopic point of view, several scenarios of spin-driven ferroelectricity were proposed [77, 78]. Indeed, intensive experimental studies have confirmed that these scenarios really induce electric polarization.

Most of the spiral induced multiferroics have the cycloidal spin structures whose magnetic propagation vectors $\vec{q}$ lie in the spiral plane (Fig. 1.22) and whose magnetic symmetries allow the systems to be polar and ferroelectric [79]. The microscopic origin of such a ferroelectricity can be successfully explained by the spin current model or the inverse DM interaction [80, 81]. More precisely, within this model, the electric polarization $\vec{P}_{ij}$ produced between two canted spins $\vec{S}_i$ and $\vec{S}_j$, located at sites i and j, respectively, is given by

$$\vec{P}_{ij} \propto \vec{e}_{ij} \times (\vec{S}_i \times \vec{S}_j) \equiv \vec{p}_1 \tag{1.52}$$

where $\vec{e}_{ij}$ is a unit vector joining the sites i and j. However, recent multiferroics such as $CuFeO_2$ and $CuCrO_2$ show a spin-driven ferroelectricity that cannot be explained by such a model. This is because in these multiferroics, the spiral-spin structure is a proper-screw one where the propagation vector $\vec{q}$ is perpendicular to the spiral plane [24–26] as shown in Fig. 1.22. In this configuration, $\vec{S}_i \times \vec{S}_j$ is parallel to $\vec{e}_{ij}$ ($\vec{e}_{ij}$ is along the $\vec{q}$ direction due to symmetry considerations [67]), and hence Eq.(1.52) will lead to a net zero polarization. Thus the microscopic origin of this ferroelectric polarization can be actually described by the variation in the metal-ligand $(d-p)$ hybridization with spin-orbit coupling [82, 83] as proposed by Arima [84]. Accordingly, based on symmetry considerations, Kaplan and Mahanti [85] introduced an additional contribution $\vec{p}_2 \propto (\vec{S}_i \times \vec{S}_j)$ to the macroscopic polarization which contributes in both cycloid and proper-screw configurations unless a mirror plane containing $\vec{e}_{ij}$ or twofold rotation axis perpendicular to $\vec{e}_{ij}$ exists. Therefore, within this model, now referred to as extended inverse DM model, the

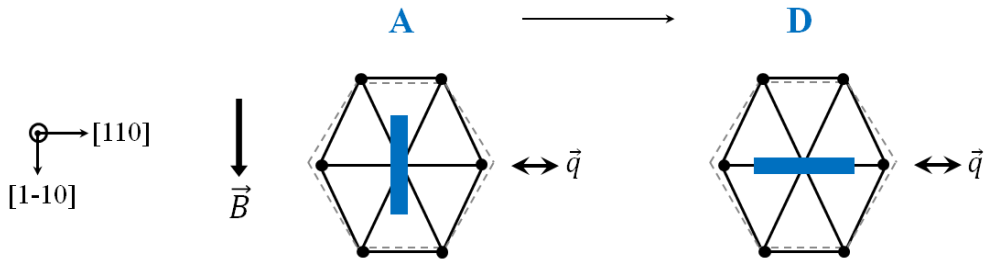

FIG. 1.23. Flop of domain A to domain D under $B_{flop} \approx 5.3$ T applied along the $[1\bar{1}0]$ direction in $CuCrO_2$.

total polarization is given by

$$\vec{P} = \vec{p}_1 + \vec{p}_2 \tag{1.53}$$

Therefore, now the direction of $\vec{P}$ is determined by the sum of the two orthogonal components, $\vec{p}_1$ and $\vec{p}_2$. Hence, the extended inverse DM model is now applicable to the proper-screw structure in $CuCrO_2$, which shows ferroelectric polarization consisting with only $\vec{p}_2$.

In frustrated magnetic systems, the GS energy is highly degenerate corresponding to several magnetic configurations. This leads to the possibility of occurrence of magnetic phase transition under a weak applied magnetic field. Large ME effect can be seen in these multiferroics when applying an external magnetic field, resulting in a sudden change in the ferroelectric polarization direction due to a flop of the spiral plane [86]. When applying an external magnetic field perpendicular to the screw axis, the spiral spin structure would vary from proper-screw type to a cycloidal one with the spiral axis parallel to the magnetic field. Such kind of magnetic field induced ferroelectric transition was reported in some hexaferrites [87–90]. Frustrated triangular antiferromagnet $CuCrO_2$ undergoes first order magnetic phase transition from proper-screw to cycloidal structure when applying a magnetic field $B_{flop} \approx 5.3$ T along $[1\bar{1}0]$ [13, 91, 92]. Such transition leads to the flop of the spiral plane from A to D domain (Fig. 1.23) seen through the significant decrease of the ferroelectric polarization measured along the $[110]$ direction [65]. Such flop is very crucial in $CuCrO_2$ since it corresponds to a change in the nature of the magnetic structure from proper-screw to cycloidal structure preserving the same $\vec{q}$ modulation vector. Even though, not only magnetic control of ferroelectricity can be seen in $CuCrO_2$, but also electric control of magnetism exists at the same time. In the absence of electric $(\vec{E})$ and magnetic $(\vec{B})$ fields, the $120°$ configuration is triply degenerate, i.e. three magnetic domains A, B and C exist equiprobable in a crystal of $CuCrO_2$ (Fig. 1.21). Taking also into account the doubly degenerate spin chirality, we remain with six magnetic domains that coexist under zero field as described in Refs. [65, 91]. Since these six domains are degenerate, they occupy the same volume in a crystal

of $CuCrO_2$, leading to a net zero ferroelectric polarization. Hence by applying a poling electric field, one can quite easily select a ferroelectric domain that corresponds to a magnetic domain leading to the detection of a finite ferroelectric polarization along the applied field. Such control of ferroelectric domains within the same ferroelectric state is very important for the reversal of polarization. This good ME tunability in $CuCrO_2$, using both $\vec{B}$ and $\vec{E}$ fields, makes it a very important member in the multiferroic family of class-II.

1.4 Magnetically diluted $CuCrO_2$

Motivated by the study of the collective behavior in conventional magnets, researchers turned their attention to diluted magnets that exhibit novel promising characteristic properties. When a pure magnet exhibits frustrated interactions, its associated diluted magnet may present novel characteristic properties such as spin-glass behavior [93, 94]. Beside this new behavior, the diluted magnet or the diluted semiconductor may possess better magnetic and electric properties [52, 95] than the pure one. In particular, doping $CuCrO_2$ by Ga^{3+}* $(S = 0)$ in the Cr^{3+} sites results in a material that may combine the good performances from both semiconductors $CuCrO_2$ and $CuGaO_2$ [96]. It was shown that $CuCr_{1-x}Ga_xO_2$ exhibits better optical transmittance properties than both $CuCrO_2$ and $CuGaO_2$ [97]. Also $CuCr_{1-x}Ga_xO_2$ is used as a photocathode in the p-type dye sensitized solar cells (DSSCs) where it shows the best performance after optimizing the composition and the thickness of the photocathode film [97].

Due to the very close radii of Cr^{3+} ($r_{Cr^{3+}} = 61.5$ pm) and Ga^{3+} ($r_{Ga^{3+}} = 62$ pm), no significant changes in the structural parameters of the unit cell of $CuCrO_2$ were detected upon doping [98]. Also it was found that $CuCr_{1-x}Ga_xO_2$, with small concentrations of Ga^{3+}, preserves its antiferromagnetic nature while at higher concentrations the system turned to be disordered evidencing the possibility of the existence of spin-glass-like behavior [99]. However, such spin-glass-like behavior is still a prediction and no rigorous investigations were done to characterize well such phenomenon. Neutron powder diffraction experiments performed on $CuCr_{0.9}Ga_{0.1}O_2$ showed that the magnetic peaks observed at 1.8 K correspond to a propagation vector $\vec{q} = (0.329, 0.329, 0)$ where they are significantly broadened compared to that of $CuCrO_2$ which evidenced the presence of a disorder in the magnetic structure [98]. Thus, for the moment the two main ingredients of the spin-glass state (disorder + frustration) are presented but still alone not

*Gallium was discovered in Paris by Paul-Émile Lecoq de Boisbaudran in 1875. Since its discovery, gallium has been used to make alloys with low melting points as well as it has been used as a good dopant in semiconductor substrates.

sufficient to speak precisely about the existence of such complex frozen state. Based on that, we aim in this work to investigate the effect of such magnetic dilution (Ga^{3+} doping) on the magnetic properties of the delafossite $CuCrO_2$ by means of a combination of $ab\ initio$ (Appendix A) calculations and Monte Carlo simulations presented in Chapter 4. We try to characterize well the magnetic states for various concentrations of Ga^{3+} ($x = 0, 0.02, 0.05, 0.1, 0.15, 0.2$ and 0.3) to provide better understanding for such diluted antiferromagnet.

CHAPTER 2

Model and Monte Carlo method

This chapter presents the physical models and the numerical simulation technique used to investigate the magnetoelectric properties of $CuCrO_2$.

2.1 Model description

As previously mentioned, $CuCrO_2$ crystallizes in the layered $R\bar{3}m$ space group in the delafossite structure. Such delafossite structure with trigonal system and hexagonal axes is formed of edge shared CrO_6 layers alternatively stacked between Cu^+ layers along the vertical direction (c axis) as shown in Fig. 1.12 [with $a = 2.9746(1)$ Å and $c = 17.1015(3)$ Å in the hexagonal structure]. Each layer of ions forms a two dimensional triangular lattice. Within the different ions of $CuCrO_2$, we are just concerned in the magnetic ones (Cr^{3+}, $S = 3/2$) to model its magnetic and ferroelectric properties. A model based on triangular lattices stacked vertically is used to build the crystal. In this crystal, a single unit cell contains three chromium ions located as: $Cr^{3+}(a/3, 2a/3, c/6)$, $Cr^{3+}(0, 0, c/2)$ and $Cr^{3+}(2a/3, a/3, 5c/6)$. The coordination numbers for the 1^{st}, 2^{nd}, 3^{rd} and 4^{th} neighbors of each Cr^{3+} ion are identical with $z = 6$.

A box of $L_a \times L_b \times L_c$ unit cells is built. Note that $L_a = L_b = L$, thus in the following we will use L for L_a and L_b, and L_z for L_c. The simulation box is then composed of $N = 3 \times L^2 \times L_z$ spins located at the corners of the triangular plaquettes within each ab plane (Fig. 2.1) stacked vertically

size systems, we implemented periodic boundary conditions in all direction to reduce finite size effects which will be discussed later in Sec. 2.3. Each Cr^{3+} ion is represented by a three dimensional vector $\vec{S} = (S_x, S_y, S_z)$ that rotates freely in all directions with x, y and z follow

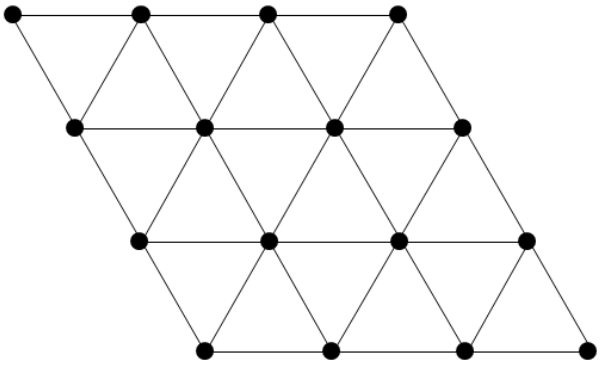

FIG. 2.1. $L \times L$ triangular lattice representing each plane of Cr^{3+} ions.

the $[110]$, $[\bar{1}10]$ and $[001]$ directions, respectively. Then, our magnetic Hamiltonian is given by

$$H_m = -\sum_{\langle i,j \rangle} J_{ij} \vec{S}_i \cdot \vec{S}_j - D_x \sum_i S_{ix}^2 - D_z \sum_i S_{iz}^2 - \vec{B} \cdot \sum_i \vec{m}_i \tag{2.1}$$

where J_{ij} represents the exchange interactions up to the fourth neighbors (Fig. 2.2), $D_x < 0$ and $D_z > 0$ are the single ion anisotropy constants of the hard and easy axes along the $[110]$ and $[001]$ directions, respectively, and $\vec{B}$ is the applied magnetic field. This Hamiltonian was first used in the DFT calculations to extract the values of the exchange interactions and single ion anisotropy constants in the non-distorted and the distorted crystal structure, and it is then used in our FORTRAN code based on the Monte Carlo (MC) method.

In the presence of an electric field $\vec{E}$, the coupling between the spins and $\vec{E}$ is defined as

$$H_e = -A_0 \vec{E} \cdot \sum_{\langle i,j \rangle} \vec{S}_i \times \vec{S}_j \tag{2.2}$$

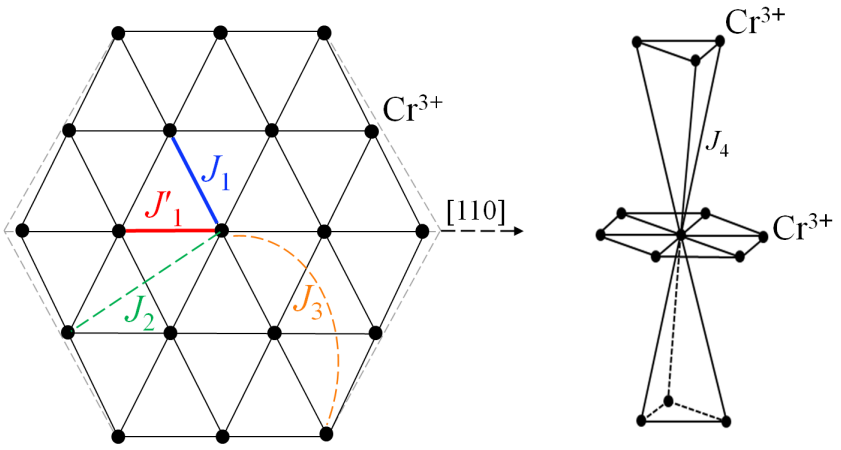

FIG. 2.2. Intralayer and interlayer super-exchange interactions in $CuCrO_2$ with $J_1' = J_1$ in the non-distorted crystal structure, and $J_1' > J_1$ in the distorted one.

where the sum runs over the magnetic bonds along the $[110]$ direction, and A_0 is a coupling constant related to the spin-orbit and spin exchange interactions [67].

Therefore the total Hamiltonian will be $H_m + H_e$ given as

$$\begin{aligned} H &= -\sum_{\langle i,j \rangle} J_{ij} \vec{S}_i \cdot \vec{S}_j - D_x \sum_i S_{ix}^2 - D_z \sum_i S_{iz}^2 \\ &\quad + g\mu_B \vec{B} \cdot \sum_i \vec{S}_i - A_0 \vec{E} \cdot \sum_{\langle i,j \rangle} \vec{S}_i \times \vec{S}_j \end{aligned} \tag{2.3}$$

2.2 Monte Carlo method

2.2.1 Generalities

In the recent years, numerical simulation tools have been developed considerably by increasing the capacity of super computers and improving the algorithms. Numerical simulations can be considered as a bridge between theoretical and experimental studies. They allow to study various physical phenomena where usually the analytical solution is impossible, like the problem of understanding phase transitions in systems with many competing Heisenberg interactions. Also numerical simulations can replace some difficult or very expensive experimental measurements and provide the desired outcomes. An important advantage of numerical simulations is that, they deal with fully pure isolated systems unlike real systems where different physical effects simultaneously exist such as chemical impurities, synthesize environment... Also by numerical simulations, one can study the effect of varying one physical parameter on the properties of a given system which is not possible experimentally.

MC method is a broad class of computational algorithms based on random number sequences. It is a stochastic method that can be used in many scientific disciplines like physics, chemistry, biology... The basis of the MC method is the theory of Markov chains which is a process that allows one to make predictions for the future of a system based on its present state only.

In physics, MC simulation do well treat the equilibrium properties of many-particle interacting systems. To study these interacting systems, one should define a reference space known as the phase space which represents, in case of a spin system, the set of spin configurations. Each possible spin configuration is represented as

$$X = \left(\vec{S}_1, \vec{S}_2, ..., \vec{S}_i, ..., \vec{S}_{N-1}, \vec{S}_N \right) \tag{2.4}$$

where N is the number of spins in the system.

The transition probability per unit time that corresponds to the transition from a configuration X to a configuration X' is denoted by $W(X, X')$. The important property of a Markov chain is the existence of an equilibrium distribution of states. A sufficient condition for having a stationary probability distribution is

$$W(X, X')P(X) = W(X', X)P(X') \tag{2.5}$$

which is called the detailed balance condition.

Now, the approach is to separate the transition in two sub-steps; the proposal and the acceptance-rejection steps. The proposal distribution $g(X, X')$ is the conditional probability of proposing a state X' given X, and the acceptance distribution $A(X, X')$ is the conditional probability to accept the proposed state X'. Therefore, the transition probability $W(X, X')$ can be written as

$$W(X, X') = g(X, X')A(X, X') \tag{2.6}$$

with $g(X, X') = g(X', X)$.

2.2.2 MC method in the canonical ensemble

In the canonical ensemble, the probability distribution at a given temperature T is defined as

$$P_T(X) = \frac{exp(-E(X)/k_BT)}{Z(T)} \tag{2.7}$$

where $E(X)$ is the energy of a given configuration X, k_B is the Boltzmann constant and $Z(T) = \sum_X exp(-E(X)/k_BT)$ is the partition function at a given temperature T. Therefore, Eq. (2.5) will be re-written as

$$\frac{W(X, X')}{W(X', X)} = \frac{P(X')}{P(X)} = exp(-\Delta E/k_BT) \tag{2.8}$$

which depends only on the energy variation $\Delta E = E(X') - E(X)$ during the transition $X \longrightarrow X'$.

Thermal averages, or Gibbs averages, are defined by

$$\langle A \rangle_T = \frac{\sum_X A(X)exp(-E(X)/k_BT)}{\sum_X exp(-E(X)/k_BT)} \tag{2.9}$$

with A being any thermodynamic quantity.

2.2.2.1 Metropolis algorithm

The Metropolis algorithm [100] is a single spin rotation algorithm, i.e., the transition from a configuration X to a configuration X' is associated with a change in the orientation of one spin $\left(\vec{S}_i \longrightarrow \vec{S}'_i\right)$ and thus $X' = \left(\vec{S}_1, \vec{S}_2, ..., \vec{S}'_i, ..., \vec{S}_{N-1}, \vec{S}_N\right)$. It has an acceptance probability $A(X, X')$ or simply $A(\vec{S}_i, \vec{S}'_i)$ defined as

$$A(\vec{S}_i, \vec{S}'_i) = \min\left\{1, e^{-\Delta E/k_B T}\right\} \tag{2.10}$$

Note that the probability to accept a new configuration, which increases the energy of the system, decreases with the decrease of temperature (it is approximately 1 at high T in the disordered state, and almost null in the low T region when the system is almost ordered). Therefore, for a given initial random magnetic configuration X_0, the Metropolis algorithm at each temperature T goes as follow:

1. Choose randomly a spin $\vec{S}_i$ and suggest for it a new random orientation $\vec{S}'_i$.
2. Calculate the energy variation ΔE associated to this rotation according to Eq. (2.3).
3. If $\Delta E < 0 \Longrightarrow$ accept the new orientation.
   Else, choose a random number $0 < r < 1$ with uniform distribution, and check if $r \leq exp(-\Delta E/k_B T)$ accept the new orientation, otherwise reject.
4. Choose another spin randomly (back to step 1).

N repetitions of the steps 1 to 4 is known as a MC step (MCS), with N being the number of spins in the system. A large number of MCS ($n_{MCS} = 10^5$ for e.g.) is performed at each temperature, so that each spin is examined n_{MCS} times in average.

2.2.2.2 Time Step Quantified Monte Carlo method

The standard Metropolis algorithm is known to be efficient in finding one of the lowest energy configurations and calculating the equilibrium quantities at each temperature. It minimizes the free energy of the system at each temperature without "seeing" the different energy barriers that should be overcome when going from a configuration X to another one X'. Nevertheless, the

standard Metropolis algorithm exhibits the problem of having no physical time associated with each MC step, resulting in unquantified dynamic behavior. It was found that Langevin dynamics is a very good approach for studying the dynamic behaviors, but unfortunately it is limited to time scales of the order of few ns. And because the MC approach is less time consuming, U. Nowak *et al.* [101] succeeded to quantify each MCS and associate it to a real physical time. The trial step of this algorithm is a random movement of each spin $\vec{S}_i$ within a cone of a given size. For this purpose, a random vector $\vec{u}$ with a uniform probability distribution is chosen within a sphere of radius R (Fig. 2.3). After that, $\vec{u}$ is added to $\vec{S}_i$ and subsequently the resulting vector is normalized to obtain $\vec{S}_i' = S\frac{\vec{S}_i+\vec{u}}{\|\vec{S}_i+\vec{u}\|}$. The radius of the sphere (cone) R affects the physical time associated to 1 MCS [101]. Indeed, R cannot take any value, it should satisfy the condition $R < 1$, but at the same time it should not be too small since then the algorithm becomes inefficient. The procedure of this new algorithm, in our case, is the same as the standard Metropolis in terms of the acceptance-rejection principle.

Within this algorithm, 1 MCS is associated to a real time interval Δt through the following relation

$$R^2 = \frac{20\alpha\gamma k_B T}{(1+\alpha^2)m}\Delta t \tag{2.11}$$

where α is a damping constant chosen to be ≥ 1 for the validity of the formula [101], $\gamma = 1.76 \times 10^{11}\ (Ts)^{-1}$ is the gyromagnetic ratio, k_B is the Boltzmann constant, and m is the theoretical magnetic moment ($3\mu_B$ in our case).

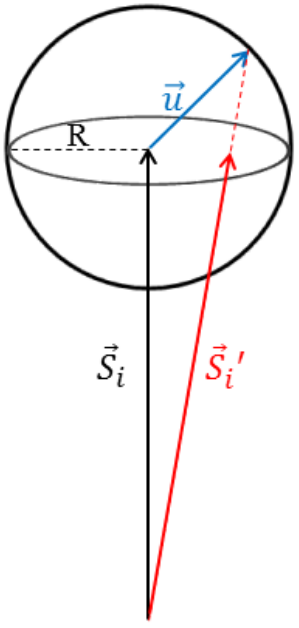

FIG. 2.3. Schematic illustration of the principle of the time step quantified Monte Carlo method with $R < 1$.

Thus, from Eq. (2.11), one has to choose either a value for Δt (usually it is of the order of 10^{-12} s) to find R, or to choose a reasonable value of R (0.1 for example) and find Δt to be the real time interval corresponding to 1 MCS. Thus for example, if one takes $R = 0.1$ and $\alpha = 1$ for $T = 10$ K, Eq. (2.11) gives us $\Delta t = 1.15 \times 10^{-15}$ s associated to 1 MCS.

With this new technique, the algorithm is able to see the energy barriers in the phase space, and thus it allows us to simulate the hysteresis loops at various temperatures (but not too small) within reasonable computer time.

Although, this new technique doesn't succeed in all systems and still faces some limitations. For example, if one consider a ferromagnetic system with very strong exchange couplings and at very low temperatures, single spin rotations are not possible because the system can only rotate uniformly.

2.2.2.3 Simulated annealing – Calculation of different thermodynamic quantities

The algorithm of simulated annealing was proposed by S. Kirkpatrick *et al.* [102, 103]. During the annealing process, the system which is initially at high temperature and in a paramagnetic phase is slowly cooled so that the system achieves its thermodynamic equilibrium at each temperature after a time interval n_0 called the *equilibration time*. As the cooling proceeds, the system becomes more ordered and its energy decreases (Fig. 2.4) to approach its minimum near 0 K. The magnetic configuration at 0 K is known as the ground state configuration which can be degenerate in some systems. In frustrated systems, if the initial temperature of the system is below its ordering temperature (T_N or T_C), or if the cooling process is not sufficiently slow the system may be frozen in a metastable state (i.e. trapped in a local minimum energy state at low temperatures) and doesn't achieve one of its ground state configurations. In order to calculate thermal averages, the system should explore all the phase space. However, in our MC simulations, we make time averaging (over the number of MCS at equilibrium) which is equivalent to the Gibbs averaging (Eq. 2.9), if n_{MCS} is large enough, according to the choice of our transition probability. This is known as the ergodicity principle.

To estimate n_0, it is possible to plot any thermodynamic quantity versus n_{MCS} (i.e., versus time) and to see when the system reaches its equilibrium, see Fig. 2.4. After that, time averaging is done over $(n_{MCS} - n_0)$ MCS. Thus, the thermal average $\langle A \rangle_T$ of any thermodynamic quantity

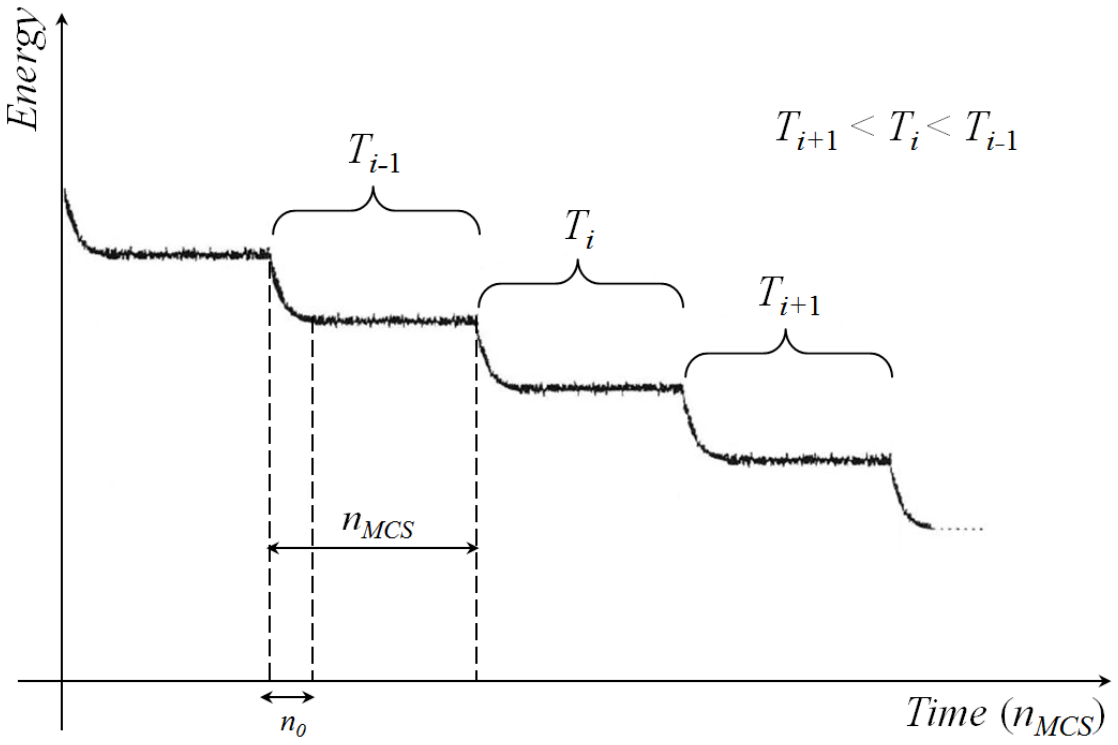

FIG. 2.4. Time variation of the internal energy during the cooling process.

A is calculated as

$$\langle A \rangle_T \simeq \frac{1}{n_{MCS} - n_0} \sum_{\ell=n_0+1}^{n_{MCS}} A(X_\ell) \tag{2.12}$$

with X_ℓ is the spin configuration at the end of the ℓ^{th} MCS. Note that A in our simulations is one of the different thermodynamic quantities such as internal energy, chirality of spins, spin-spin correlation functions, and a magnetic order parameter $\vec{P}$ related to the ferroelectric polarization.

- Internal energy $U(T)$ per spin

$$U(T) = \frac{\langle H \rangle_T}{N} = \frac{1}{N(n_{MCS} - n_0)} \sum_{\ell=n_0+1}^{n_{MCS}} H(X_\ell) \tag{2.13}$$

where N is the number of spins in the system.

- Chirality of spins $\kappa(T)$ per magnetic bond

To characterize the nearly 120° GS configuration we considered the spin chirality defined as

$$\vec{\kappa}_p = \frac{1}{S^2} \frac{2}{3\sqrt{3}} (\vec{S}_1 \times \vec{S}_2 + \vec{S}_2 \times \vec{S}_3 + \vec{S}_3 \times \vec{S}_1) \tag{2.14}$$

where 1, 2 and 3 refer to the spins at the corners of each elementary triangular plaquette p in an ab plane (Fig. 2.5). $\kappa_p = 1$ for the perfect 120° configuration. Then we defined

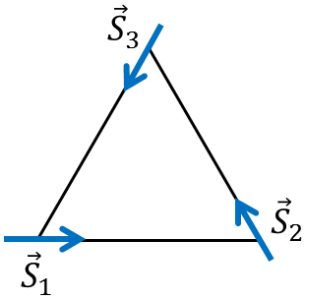

FIG. 2.5. Triangular plaquette p.

the order parameter per plane to be $\lambda = \frac{1}{n_b}\|\sum_p \vec{\kappa}_p\|$ where n_b is the number of magnetic bonds per plane, and finally the order parameter of the whole system was defined as $\kappa = \langle\bar{\lambda}\rangle_T$ where $\bar{\lambda}$ is the average of λ over the ab planes.

And finally,

$$\kappa(T) = \frac{1}{n_{MCS} - n_0} \sum_{\ell=n_0+1}^{n_{MCS}} \bar{\lambda}(X_\ell) \tag{2.15}$$

- Spin-spin correlation functions $G(R,T)$ per magnetic bond

  In order to characterize more precisely the magnetic configurations, we calculated the temperature dependence of the spin-spin correlation functions along the a-direction ($[100]$ direction) defined as

$$G(R,T) = \frac{1}{N_a(n_{MCS} - n_0)} \sum_{\ell=n_0+1}^{n_{MCS}} \left(\frac{1}{S^2} \sum_{\langle i,j \rangle} \vec{S}_i \cdot \vec{S}_j \right)_\ell \tag{2.16}$$

  where N_a is the number of pairs $\vec{S}_i, \vec{S}_j$ separated by a distance R along the a-direction.

- $\vec{P}$ associated to the ferroelectric polarization per magnetic bond

  As proposed by Kaplan and Mahanti [85], Eq.(1.53) describes the electric polarization in $CuCrO_2$. And since $\vec{P}$ is allowed only along the $[110]$ direction due to symmetry considerations [67], we then calculate

$$\mathscr{P}(T) = \frac{1}{N_x(n_{MCS} - n_0)} \sum_{\ell=n_0+1}^{n_{MCS}} \left(\vec{e}_x \cdot \sum_{\langle i,j \rangle} \vec{S}_i \times \vec{S}_j \right)_\ell \tag{2.17}$$

  to be the projection of $\vec{P}$ along the $[110]$ direction. The sum of $\langle i,j \rangle$ runs along the $[110]$ direction and $N_x = (L-1)^2$ is the number of first nearest neighbor magnetic bonds counted along that direction in each ab plane. Then we average $\mathscr{P}$ over the atomic planes

to finally obtain

$$P_{[110]}(T) = \frac{1}{3L_z} \sum_{i=1}^{3L_z} \mathscr{P}_i(T) \tag{2.18}$$

with $3L_z$ represents the number of the ab planes found in the system.

- Specific heat $C(T)$ per spin

  The specific heat per spin is calculated as

$$C(T) = \frac{\partial U}{\partial T} = \frac{\langle H^2 \rangle_T - \langle H \rangle_T^2}{N k_B T^2} \tag{2.19}$$

- Linear magnetic susceptibility $\chi(T)$ per spin

  Because $\mathrm{CuCrO_2}$ is an antiferromagnetic system, magnetization can be derived only under an applied external magnetic field $\vec{B}$. Thus the associated linear magnetic susceptibility measured along the direction of $\vec{B}$ is defined as

$$\chi(T) = \frac{M_B(T)}{H} \tag{2.20}$$

  with

$$M_B(T) = \frac{-g}{N(n_{MCS} - n_0)} \, \vec{e}_B \cdot \sum_{\ell=n_0+1}^{n_{MCS}} \left(\sum_i \vec{S}_i \right)_\ell \tag{2.21}$$

  being the magnetization in μ_B calculated along the direction of $\vec{B}$ and $\vec{e}_B = \frac{\vec{B}}{\|\vec{B}\|}$ is a unit vector along the magnetic field direction.

2.3 Finite size and boundary effects

In order to reduce finite size effects, we implement the periodic boundary conditions (PBCs) in all directions. However, it is well known that PBCs can affect the simulated magnetic configuration near 0 K when the GS configuration is incommensurate. Thus, to characterize well the effect of the PBCs on the energy and magnetic configuration of the GS in $\mathrm{CuCrO_2}$, we calculate the exchange energy per spin of a finite system as function of the size L and the propagation vector $\vec{q} = (k, k, 0)$ with only the first nearest neighbor interactions in the distorted 2D crystal structure

according to

$$\begin{aligned} E_{ex}(k,L) &= \frac{-S^2}{L^2}\left(\left[L^2-2L+1\right]J_1'\cos(4\pi k)+2L(L-1)J_1\cos(2\pi k)\right. \\ &\quad +2(L-1)J_1'\cos\left[2\pi k(L-2)\right]+J_1'\cos\left[4\pi k(L-1)\right] \\ &\quad \left.+2LJ_1\cos\left[2\pi k(L-1)\right]\right) \end{aligned} \tag{2.22}$$

In the infinite system ($L \longrightarrow \infty$), Eq. (2.22) becomes

$$E_{ex}(k) = -S^2\left(J_1'\cos(4\pi k)+2J_1\cos(2\pi k)\right) \tag{2.23}$$

The minimization of Eq. (2.23) w.r.t k gives

$$\cos(2\pi k_{inf}) = \frac{-J_1}{2J_1'} \tag{2.24}$$

with k_{inf} denotes the value of the propagation vector in one of the GS configurations of the infinite lattice. In the non-distorted structure, Eq. (2.24) gives $k_{inf} = 1/3$ or $k_{inf} = 2/3$. To simplify the discussion we will work in one of the GS configurations of $CuCrO_2$. In the distorted crystal structure with $J_1 = -2.383$ meV and $J_1' = -2.709$ meV (see Chapter 3), Eq. (2.24) gives $k_{inf} \approx 0.3225$. Then the energy of the infinite system corresponding to $k_{inf} \approx 0.3225$ is $E_{inf}/k_B = -98.08838$ K. Fig. 2.6 shows the variation of $E_{ex}(k,L)$ as functions of L for $k_{inf} \approx 0.3225$. It can be seen that the energy of the finite system with PBCs does well depend

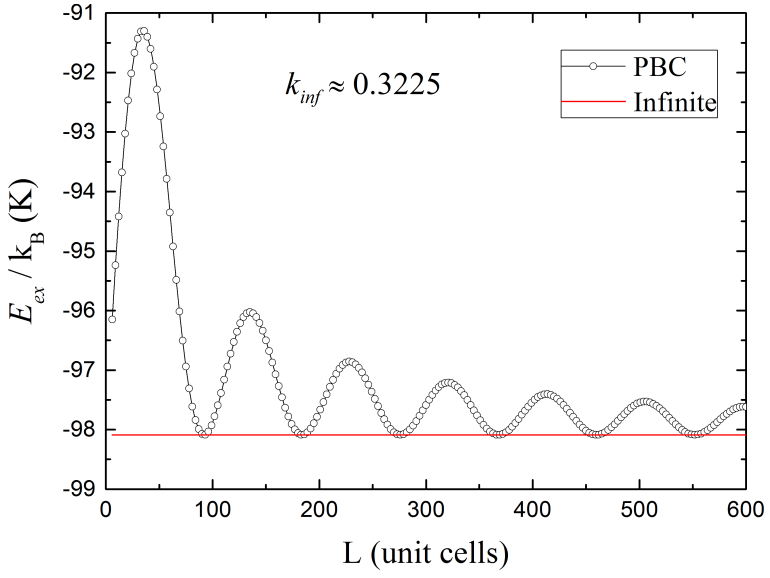

FIG. 2.6. Theoretical curves of the variation of the exchange energy as function of size L (multiples of 3) in a 2D system compared to that in the infinite system.

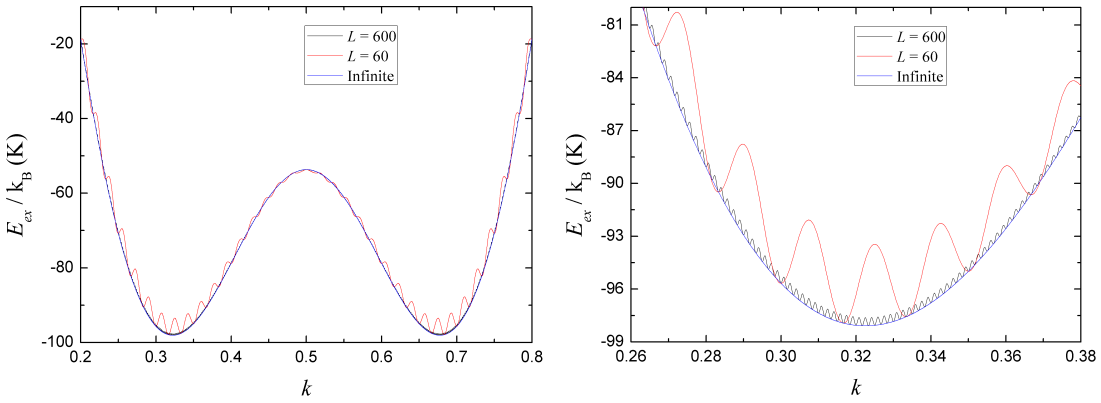

FIG. 2.7. Theoretical curves of the variation of exchange energy versus k (left), and its corresponding zoom in the minimal energy regime (right) in a 2D system.

on L and approaches that of the infinite system when L is very large as well as for particular values of L which correspond to the minima of $E_{ex}(k, L)$ in Fig. 2.6. Such sinusoidal damping shape is due to the excess of energy at the boundaries of the system due to the PBCs because of the incommensurability of the magnetic configuration.

Now for a given finite system of size L, we can see the effect of the PBCs on the magnetic configuration of the GS by plotting $E_{ex}(k, L)$ versus k as shown in Fig. 2.7. For example, if $L = 600$ $k_{GS} \approx 0.3217$ is close to k_{inf} while for $L = 60$, $k_{GS} \approx 0.3167$ which reflects a significant deviation from k_{inf}. However for the finite system of size $L = 90$ that corresponds to the first minimum of $E_{ex}(k, L)$ (Fig. 2.6), $k_{GS} \approx 0.3222$ is very close to k_{inf}. Inspite of the k-dependence of $E_{ex}(k, L = 90)$ shown in Fig. 2.8, it can be clearly seen that the minimum of $E_{ex}(k, L = 90)$ $(E_{GS}/k_B = -98.088$ K) is very close to that of the infinite system

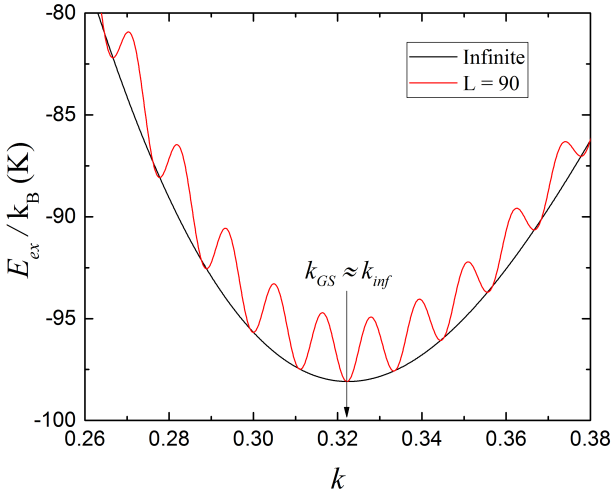

FIG. 2.8. Theoretical curves of the variation of the exchange energy versus k for $L = 90$ in comparison with that of the infinite system.

$(E_{inf}/k_B = -98.08838\ \mathrm{K})$.

Therefore, based on what mentioned, we can say that these PBCs perturb the magnetic configuration in the case of incommensurate helimagnetic structures like in $CuCrO_2$. Thus the choice of L is very sensitive and has an effect on the GS configuration of the simulated system.

To verify the effect of PBCs in our MC simulations, we test various system sizes and see their corresponding GS configuration for the same $J_1 = -2.383$ meV and $J_1' = -2.709$ meV. To characterize well the simulated magnetic configuration at a very low temperature we calculate the propagation vector $\vec{q} = (h, k, 0)$ such that h and k are calculated along the a and b directions, respectively. Given two spins $\vec{S}_i$ and $\vec{S}_j$ along the a or b directions, the angle between $\vec{S}_i$ and $\vec{S}_j$ is given by $\theta_{ij} = 2\pi h$ or $\theta_{ij} = 2\pi k$. Also, θ_{ij} is calculated from the scalar product of $\vec{S}_i$ and $\vec{S}_j$ according to

$$\cos(\theta_{ij}) = \frac{\vec{S}_i \cdot \vec{S}_j}{S^2} \tag{2.25}$$

Consequently, one can write

$$h \text{ or } k = \frac{1}{2\pi} \arccos\left(\frac{\vec{S}_i \cdot \vec{S}_j}{S^2}\right) \tag{2.26}$$

The simulations start from random spin configurations at a sufficiently high initial temperature $T_i = 35.01$ K. We then cool down to a final temperature $T_f = 0.01$ K with a constant temperature step $\Delta T = 1$ K. At each temperature we perform $n_{MCS} = 1.05 \times 10^5$ with discarding $n_0 = 5 \times 10^3$ for thermal equilibration. Since the value of k is expected to be close to $1/3$ or $2/3$, we then choose L to be a multiple of 3 to compare the deviation of our results from the commensurate configuration of $k = 1/3$ or $2/3$. The simulated values of $\vec{q} = (h, k, 0)$ for the different sizes are given in Table 2.1. We find that PBCs favor the closest commensurate spin configuration for $L = 15$ with a propagation vector $\vec{q} \approx (0.3333, 0.3333, 0)$. However, when $L = 30, 45$ or 60 the simulation chooses a GS configuration with a propagation vector $\vec{q} = (h, k, 0)$ with $h \neq k$ as shown in Table 2.1. For $L = 90$, $\vec{q} \approx (0.3222, 0.3222, 0)$ which is very close to $\vec{q}_{inf} \approx (0.3225, 0.3225, 0)$ in agreement with the calculations done for $L = 90$ and shown in Fig. 2.8. However, it is very important to note that for $L = 120$ $(> L = 90)$

TABLE 2.1. Simulated values of the propagation vector $\vec{q} = (h, k, 0)$ for various system sizes in a 2D lattice of $CuCrO_2$.

L	15	30	45	60	90	120
h	0.3333	0.3003	0.3332	0.3186	0.3222	0.3251
k	0.3333	0.3330	0.3112	0.3167	0.3222	0.3251

the simulation chooses again a GS configuration of propagation vector $\vec{q} \approx (0.3251, 0.3251, 0)$ which is different from that of the infinite system due to the effects of PBCs as shown in Fig. 2.6. However, we have shown in Sec. 1.1.4.1 that the commensurate GS configuration in $CuCrO_2$ with $h \neq k$ doesn't exist. Similar demonstration is found in the incommensurate configuration and hence we can say that the simulation results with $h \neq k$ are not physical but rather perturbations induced by PBCs. Thus to characterize well the real GS state configuration, we have to take much more care of the choice of L regarding all the previous effects.

It is important to note that the use of free boundary conditions (FBCs) perturb more the results due to the significant effects of the free boundaries in finite sizes. These perturbations could be minimized if a very large simulation box is considered and the results are averaged only inside its bulk which is difficult within the available computer resources.

2.4 Statistical and systematic errors

The time of a MC simulation is directly proportional to n_{MCS}, to the number of spins (N) in the system and also to the number of simulated temperature steps (n_{Temp}). Thus we can write

$$t_{sim} \propto n_{MCS} \times N \times n_{Temp} \tag{2.27}$$

Within the limited computational budgets, one should choose between performing simulations with large n_{MCS} of small system sizes or small n_{MCS} of larger sizes. These limitations are the sources of errors known as statistical and systematic errors [104].

Statistical errors [105, 106]

The autocorrelation function of a physical quantity A is defined by

$$\varphi_A(t) = \frac{\langle A(0)A(t)\rangle - \langle A\rangle^2}{\langle A^2\rangle - \langle A\rangle^2} \tag{2.28}$$

where it verifies that $\varphi_A(0) = 1$ and $\varphi_A(t) \longrightarrow 0$ when $t \longrightarrow \infty$.

The autocorrelation time of A is defined as

$$\tau_A = \int_0^\infty \varphi_A(t)dt \tag{2.29}$$

Suppose that we make n successive independent measurements $\{A_1, \ldots, A_i, \ldots, A_n\}$ of this quantity A. We define the expectation value of the square of the statistical error on the measure

of $\langle A \rangle$ as

$$\left\langle (\delta A)^2 \right\rangle = \left\langle \left[\frac{1}{n} \sum_i^n \left(A_i - \langle A \rangle \right) \right]^2 \right\rangle \tag{2.30}$$

It can be shown that, in a MC simulation, the above expectation value is related to the autocorrelation function $\varphi_A(t)$ by

$$\left\langle (\delta A)^2 \right\rangle = \frac{\langle A^2 \rangle - \langle A \rangle^2}{n} \left(1 + \frac{2}{\delta t} \int_0^{t_n} (1 - t/t_n)\, \varphi_A(t) dt \right) \tag{2.31}$$

where δt is the time interval (in MCS) between two successive measurements of A, $t_n = n\delta t$ with $\delta t \ll t_n$. In addition, if we assume that the autocorrelation function is almost null when $\tau_A \ll t_n$, the main contribution in the integral of Eq. (2.31) is obtained for $t \ll t_n$. Hence we can neglect t/t_n in front of 1 and replace the upper bound of the integral by ∞ in Eq. (2.31) and using Eq. (2.29) we obtain

$$\left\langle (\delta A)^2 \right\rangle \approx \left(\langle A^2 \rangle - \langle A \rangle^2 \right) \frac{2\tau_A + \delta t}{n\delta t} \tag{2.32}$$

Moreover, if we have $\delta t \ll \tau_A$, we can simplify Eq. (2.32) to

$$\left\langle (\delta A)^2 \right\rangle \approx \left(\langle A^2 \rangle - \langle A \rangle^2 \right) \frac{2\tau_A}{n\delta t} \tag{2.33}$$

The relative statistical error is then given by

$$\rho_A = \frac{\sqrt{\langle (\delta A)^2 \rangle}}{\langle A \rangle} \approx \sqrt{\left(\frac{2\tau_A}{n\delta t} \right) \frac{\langle A^2 \rangle - \langle A \rangle^2}{\langle A \rangle^2}} \tag{2.34}$$

It can be seen that the relative statistical error is independent of the time interval δt between two successive measurements, but depends essentially on the ratio between the autocorrelation time (τ_A) and the number of MC steps $(n\delta t)$ at thermal equilibrium. Therefore, to reduce statistical errors we need to increase n_{MCS} performed at each temperature. However, when the system is large enough, it is often impossible to increase enough n_{MCS} due to the constraints on the available computer resources. These limitations are sources of the statistical errors in MC simulations. Another source for the statistical errors is the disorder induced, for example, by chemical impurities introduced in the system. This requires to average over a large enough number of random configurations to decrease its contributions.

Systematic errors

Systematic errors in a MC simulation, like the statistical errors, arise from the finite number of

measurements n performed on the physical quantity A during the simulation. Systematic errors are particularly significant on the estimation of the specific heat and magnetic susceptibility since they are proportional to the variance of the probability distribution. For that, the specific heat and the magnetic susceptibility are systematically underestimated during a MC simulation because the estimate of a variance from a finite sample is systematically smaller than that in an infinite sample. A possible solution to reduce these systematic errors is to increase the number of measurements done by increasing n_{MCS} as much as possible.

In this work, we tried as much as possible to limit these errors. Thus we tried to simulate systems as large as possible and perform large enough number of MC steps with averaging the final results over several different simulations (parallel calculations).

CHAPTER 3

Magnetoelectric properties of $CuCrO_2$

Over the past few years, structural and magnetoelectric properties of $CuCrO_2$ were experimentally studied by neutron diffraction experiments and other techniques. However, till now, there is no clear and enough understanding of its magnetoelectric properties and its complex spin structure. Based on that, we aim to revisit this compound from the numerical simulation side. In order to model the magnetoelectric properties of this complex oxide, we calculate its exchange interactions and single ion anisotropy constants using DFT calculations in the non-distorted and distorted lattice structure presented in Sec. 3.1. Using these extracted parameters, we model the magnetoelectric properties of $CuCrO_2$ using the classical Monte Carlo method. The results of this chapter have been published in *Physical Review B* [107].

3.1 DFT calculations

These calculations were done by Y. O. Kvashnin at the "Department of Physics and Astronomy, Division of Materials Theory, Uppsala University, Sweden".

We have performed a series of DFT calculations in order to investigate the electronic and magnetoelectric properties of $CuCrO_2$. Knowing that the conventional DFT calculations underestimate the value of the energy band gap, we have applied the DFT + U method to improve the estimation of the energy band gap compared to the experimental data. However, we note that the calculated value of the energy band gap depends on the choice of Hubbard U parameters for Cu and Cr $3d$ states. In addition, we also investigate in details the effect of different double-counting correction schemes. Finally, for all different computational setups, we extract the effective

inter-atomic exchange interactions (J_{ij}) — illustrated in Fig. 2.2 — using the magnetic force theorem [108, 109].

3.1.1 Computational details

DFT calculations were performed using the full-potential linear muffin-tin orbital (FP-LMTO) method as implemented in RSPt [110] software. An experimental crystal structure was taken from Ref. [111]. No ionic relaxation was done within our DFT calculations. The electronic structure of $CuCrO_2$ has been calculated before using the DFT + U method. In literature, we found several different choices of the Hubbard U parameters for this system:

1. Choice U_1. In Refs. [112, 113] the values of $U_{eff} = U - J_H$ for Cu and Cr were set to 5.2 eV and 4.0 eV, respectively. This choice of the parameters is motivated by the fact that it gives a good description valence-band photo-emission spectra of Cu_2O and Cr_2O_3 [41, 114].

2. Choice U_2. In Ref. [63] the authors applied Hubbard U correction on Cr $3d$ only. The adopted values of the Hubbard U and the Hund's exchange J_H were 2.3 and 0.96 eV, respectively, by which they were extracted from first principle calculations for a similar system $LiCrO_2$ [115].

For most of the calculations we have adopted Fully Localized Limit (FLL) [116, 117] form of the double counting (DC) correction, which is suitable for insulators. In addition to that, for the U_2 choice we have also tried another widely used type of the DC — Around Mean Field (AMF). This form of DC is usually used for relatively small U values, which is justified in the U_2 case, but not in U_1.

3.1.2 Band gap and electronic structure

Electronic structure of $CuCrO_2$ was calculated using LDA and LDA+U methods. We have considered two magnetic configurations: ferromagnetic (FM) state where all Cr spins point in the same direction and another collinear antiferromagnetic (AFM) state. The latter phase has a lower total energy compared to the FM one, but according to the calculated values of the exchange interactions, this configuration is not the ground state of the system. This will be discussed in detail in the next section.

TABLE 3.1. Calculated magnetic moments and values of the indirect band gaps E_g obtained for different computation setups and magnetic orders.

Setup	magnetic configuration	m_{Cr} (μ_B)	m_{total} (μ_B)	E_g (eV)
LDA	FM	2.63	3.00	0.76
LDA+U [U_1, FLL]	FM	2.68	3.00	2.25
LDA+U [U_2, FLL]	FM	2.62	3.00	1.5
LDA+U [U_2, AMF]	FM	2.52	3.00	1.16
LDA	AFM	$\pm$2.54	0.00	1.1
LDA+U [U_1, FLL]	AFM	$\pm$2.65	0.00	2.38
LDA+U [U_2, FLL]	AFM	$\pm$2.56	0.00	1.78
LDA+U [U_2, AMF]	AFM	$\pm$2.46	0.00	1.5

The main computed quantities are summarized in Table 3.1. Note that the magnetic moments values on every site are calculated by projecting the magnetization density onto the muffin-tin (MT) sphere. Therefore, there is also some magnetization in the interstitial, which contributes to the total magnetic moment value. In FM state there is also a small induced magnetization on Cu and O.

As one can see, for all computational methods the magnetic moment of Cr was calculated to be close to its nominal value of $3\mu_B$, expected for a purely ionic picture. In reality, due to hybridization with oxygen p-states, the projected magnetic moment of Cr is slightly reduced. What is quite remarkable is that the change of the assumed magnetic order for the same computational method results in a small difference in the values of m_{Cr} by no more than 3.5%. Similar comparison of the band gap values reveals that the stabilization of an AFM order always leads to an increase of the E_g as compared with that in FM state.

3.1.3 Exchange interactions and anisotropy: computational details

Exchange couplings were calculated using the magnetic force theorem (i.e. the so-called Lichtenstein's formula) [108, 109]. The DFT electronic structure is mapped on the classical Heisenberg model of the following form

$$H_{ex} = -\sum_{i \neq j} J_{ij} \vec{S}_i \cdot \vec{S}_j \tag{3.1}$$

where $\vec{S}_i$ denotes the vector spin along the direction of the magnetization of the site i ($S = 3/2$). With this sign convention, positive J_{ij} corresponds to the ferromagnetic coupling. Note that also with this notation of the summation of the Hamiltonian, each bond is counted twice. Our calculations take into account the exchange interactions up to the third neighboring spins (J_1,

TABLE 3.2. Chosen MT radii in a.u.

Cu	Cr	O
1.80	2.00	1.65

J_2 and J_3) within the ab plane, and the interlayer interaction J_4 between Cr^{3+} atomic planes as show in Fig. 2.2, as well as the single ion anisotropy constants. The various parameters calculated with this method may depend on the spin configuration used to extract them. This is something normal because the electronic structure (e.g. density of states) may depend on the magnetic order. The differences are known to be large for metals and are signatures of non-Heisenberg behavior of the system. In oxides, these differences are usually much smaller. We investigate this point for $CuCrO_2$ in details below.

The exchange coupling is computed between $3d$ states of Cr. The latter are constructed performing the "MT-heads" projection scheme [118]. The wave functions are projected onto the MT spheres, whose radii are listed in Table 3.2.

For the magnetocrystalline anisotropy, the following form of energy was assumed

$$H_{MAE} = -D_x \sum_i (S_i^x)^2 - D_z \sum_i (S_i^z)^2 \tag{3.2}$$

with $D_x < 0$ and $D_z > 0$ being the single ion anisotropy constants for a hard and an easy axes anisotropy along the $[110]$ and the $[001]$ directions, respectively. Our DFT calculations provide the estimations of the exchange interactions and single ion anisotropy constants for the perfect crystalline structure without distortion, and for the distorted lattice as shown in the following sections.

3.1.3.1 Non-distorted crystal structure

For the non-distorted crystal structure, the calculated parameters are listed in Table 3.3. It can be seen that there is no single computational setup (among the ones considered here) which provide excellent agreement for both E_g and the J_{ij}'s. The best estimate of the band gap value was obtained using LDA+U [U_1, FLL] setup. However, this choice of U results in strongly suppressed exchange parameters. In turn, LDA+U [U_2, FLL] setup underestimates the band gap value. On the other hand, it provides more reasonable values J_{ij}'s. The values of J_{ij}'s depend not only on the choice of U parameters, but also on the employed double-counting correction. LDA+U in conjunction with AMF DC results enhanced the values of the J_{ij}'s with respect to

TABLE 3.3. Exchange interactions (in meV) extracted from different calculations with their corresponding transition temperatures (T_N) simulated by MC simulations. Negative sign corresponds to an AFM coupling.

Setup	State	J_1	J_2	J_3	J_4	T_N (K)
LDA	FM	-4.197	0.033	-0.508	-0.048	47.87
LDA+U [U_1, FLL]	FM	-0.411	0.024	-0.157	-0.030	7.82
LDA+U [U_2, FLL]	FM	-2.407	0.012	-0.266	-0.060	27.39
LDA+U [U_2, AMF]	FM	-4.922	-0.024	-0.339	-0.133	49.96
LDA	AFM	-3.556	0.109	-0.508	-0.073	41.11
LDA+U [U_1, FLL]	AFM	-0.556	0.036	-0.169	-0.036	9.93
LDA+U [U_2, FLL]	AFM	-2.395	0.046	-0.266	-0.073	28.03
LDA+U [U_2, AMF]	AFM	-4.632	0.024	-0.339	-0.133	50.07

those extracted from the LDA method. Even though the values of the J_{ij}'s differ for various setups, they are qualitatively comparable concerning the sign of the exchange coupling for each neighboring spin. All of the obtained sets of the J_{ij}'s indicate a geometrical frustration of Cr spins on the hexagonal lattice. We can see clearly that both sets of exchange interactions extracted from the LDA+U [U_2, FLL] starting from either FM or AFM states are nearly similar, and both give the perfect $120°$ GS configurations with the good transition temperature compared to experimental data. Thus the choice of the calculation setup is very important with no significant effect of the initial magnetic configuration (FM or AFM). Based on that, we will base our next calculations on the LDA+U [U_2, FLL] method starting from FM configuration for simplicity. Based on the Hamiltonian given in Eq. (3.2), the values of the single ion anisotropy constants are: $D_x = 0$ meV and $D_z = 0.033$ meV correspond for the hard and easy axes anisotropy, respectively.

3.1.3.2 Distorted crystal structure

Kimura *et al.* [74] have reported experimentally a tiny in-plane lattice distortion in $CuCrO_2$ that takes place below its ordering temperature (T_N) along the [110] direction. In this part of our study, we have considered this experimental lattice distortion $d = (a_2 - a_1)/a_1 = 0.0001$ illustrated in Fig. 1.20 to calculate again the J_{ij}'s and the single ion anisotropy constants. Beside $d = 0.0001$, we have tested several values of d to understand the effect of such lattice distortion on the extracted parameters and therefore on the properties of $CuCrO_2$. The dependence of the magnetization on the considered values of d was found to be negligible. A magnetic moment of about 2.62 μ_B per Cr atom has been obtained. The a_2 parameter was set to the experimental

TABLE 3.4. Exchange interactions and single ion anisotropy constants (in meV) extracted from different structures corresponding to different values of lattice distortion. Negative sign corresponds to an AFM coupling.

d	J_1/J_1'	J_1'	J_1	J_2	J_3	J_4	D_x	D_z
0.0001	0.995	−2.419	−2.407	0.012	−0.266	−0.060	−0.000	0.033
0.001	0.952	−2.516	−2.395	0.012	−0.266	−0.060	−0.000	0.033
0.002	0.917	−2.612	−2.395	0.012	−0.266	−0.060	−0.000	0.033
0.003	0.879	−2.709	−2.383	0.012	−0.266	−0.060	−0.001	0.033

lattice constant and was kept fixed in the calculations. a_1 was varied, such that a_1 is always smaller than a_2. J_1' corresponds to the shorter distance to the neighboring spin. From Table 3.4, we can see that the distortion primarily affects the 1^{st} nearest neighbor couplings, while its effect on the remaining neighboring interactions is negligible. For the experimental lattice distortion $d = 0.0001$, we note that our values of J_1, J_1' and D_z are very close to the ones reported experimentally in Ref. [92] which confirm that our DFT calculations provide good estimates. It is very important to note that the magnitude of the in-plane single ion anisotropy constant (D_x) increases when d increases reflecting the fact that this type of anisotropy results from the lattice distortion (magnetostriction) associated with the spiral magnetic ordering below T_N.

To fit our goal and model the magnetoelectric properties of $CuCrO_2$, we need a complete set of exchange interactions and single ion anisotropy constants that is able to give an incommensurate GS configuration and to reproduce experimental results. However, we found that the sets of $d = 0.0001$, $d = 0.001$ and $d = 0.002$ can't reproduce the incommensurate magnetic configuration for a reasonable size within the available computer resources due to the effect of PBCs. They require large systems $(L > 90)$ to see the small deviation from the perfect $120°$ configuration. On the other hand, we know that the hard axis anisotropy in our system is very important to fix a spiral plane and to speak about spontaneous ferroelectricity. But it can be seen that the sets of exchange interactions and single ion anisotropy constants corresponding to the $d = 0.0001$, $d = 0.001$ and $d = 0.002$ can't fit our goal because $D_x \approx 0$. Therefore, we will take the set of $d = 0.003$ to launch our simulations.

3.2 Monte Carlo simulation results

Based on the discussions we made in Sec. 2.3, we choose the size $L = 90$, whatever the value of L_z, in all our MC simulations to model the true GS configuration in $CuCrO_2$.

3.2.1 Study without an external magnetic field

We start our simulations from random spin configurations at a high enough temperature ($T_i = 35.01$ K) above the transition temperature of the system. We then cool down to a final temperature ($T_f = 0.01$ K) to characterize the GS configuration of the system. The cooling process follows an algebraic sequence such that $T_{i+1} = T_i - \Delta T$. At each temperature step, we perform $n_{MCS} = 1.05 \times 10^5$ MCS by which $n_0 = 5 \times 10^3$ MCS is discarded for thermal equilibration. Note that we average our results over 28 simulations with different random configurations ($n_{conf} = 28$) to reduce statistical errors. The parameters of simulations are listed in Table 3.5. Note that these simulations of size $90 \times 90 \times 3$ with such parameters require $t_{sim} \approx 253$ hours.

TABLE 3.5. MC simulation parameters used in the study of phase transition and GS configuration in $CuCrO_2$.

Simulation parameters								
Size	N	T_i (K)	ΔT (K)	T_f (K)	n_{Temp}	n_{conf}	n_{MCS}	n_0
$90 \times 90 \times 3$	72 900	35.01	0.5	0.01	71	28	1.05×10^5	5×10^3

3.2.1.1 Ground state configuration and phase transition

Fig. 3.1 shows the temperature dependence of the internal energy per spin. It shows an inflection point around 28.5 K, which suggests a phase transition at this temperature. The simulated GS energy per spin is $U(T_f)/k_B \simeq -109.856$ K. The energy contributions of each term of

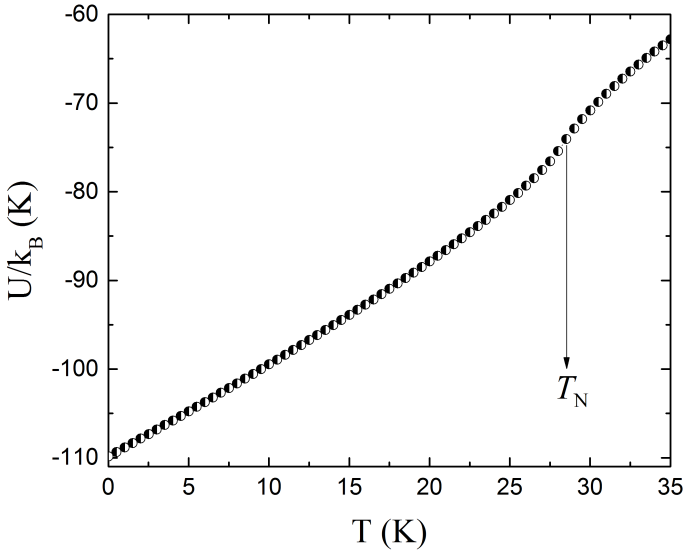

FIG. 3.1. Thermal variation of the internal energy simulated with the set of $d = 0.003$ in $CuCrO_2$.

TABLE 3.6. Energy contribution per spin of each term of the Hamiltonian of Eq. (2.3) at $T_f = 0.01$ K simulated with the set of $d = 0.003$ for a size $90 \times 90 \times 3$ in $CuCrO_2$.

E_{J_1}/k_B (K)	E_{J_2}/k_B (K)	E_{J_3}/k_B (K)	E_{J_4}/k_B (K)	E_{D_x}/k_B (K)	E_{D_z}/k_B (K)
-98.079	-0.931	-10.235	-0.183	0.000	-0.427

$U(T_f)$ are given in Table 3.6. It can be seen that the dominant contribution comes from the first nearest neighbors and the smaller contribution is that of J_4 which gives evidence about the quasi-two dimensional nature of the system. The simulated value of the propagation vector at $T_f = 0.01$ K is found to be $\vec{q}_{sim} \simeq (0.322, 0.322, 0)$ which is close to that reported in experimental studies $\vec{q} = (0.329, 0.329, 0)$ [12–16]. The fact that $\vec{q}_{sim} \neq (1/3, 1/3, 0)$ reflects the incommensurability of the magnetic configuration. Now in the presence of lattice distortion and by ignoring the energy contribution due to J_4, Eq. (1.30) becomes

$$\begin{aligned} E_{ex}(k) &= -S^2[2J_1\cos(2\pi k) + J_1'\cos(4\pi k) + 2J_2\cos(6\pi k) + J_2 \\ &\quad + 2J_3\cos(4\pi k) + J_3\cos(8\pi k)] \end{aligned} \tag{3.3}$$

and therefore to compare our simulated GS energy with the theoretical one, we calculate $E_{ex}(k_{sim})/k_B$ with $k_{sim} = 0.322$ and compare it to $U_{ex}(T_f)/k_B = (U(T_f) - E_{J_4} - E_{D_z})/k_B = -109.246$ K. By putting k_{sim} in Eq. (3.3) we got $E_{ex}(k_{sim})/k_B = -109.247$ K which is exactly $U_{ex}(T_f)/k_B$.

Now to see the deviation of the simulated GS energy from the commensurate 120° GS configuration, we calculate

$$E_{120^\circ} = S^2\left(J_1 + \frac{1}{2}J_1' - 3J_2 + \frac{3}{2}J_3 - \frac{1}{2}D_z\right) \tag{3.4}$$

Note that in the perfect 120° configuration, the energy contribution due to J_4 is null. Thus, for the set of exchange interactions and single ion anisotropy constants corresponding to $d = 0.003$, Eq. (3.4) gives us $E_{120^\circ}/k_B = -109.368$ K $> U(T_f)/k_B$. This confirms that the GS state configuration in the presence of lattice distortion is no more the 120° configuration, but rather an incommensurate spin structure known as the ICY state close to the 120° configuration. Fig. 3.2 shows the spin configuration of the ICY state where we can clearly see the lack of periodicity in the spin structure. Precise knowledge about the magnetic ordering in the ICY state can be gained by calculating the spin-spin correlation function $G(R, T)$ defined in Eq. (2.16). Fig. 3.3 shows the variation of $G(R, T)$ as function of the distance R along the [100] direction $(1 \leq R \leq L/2)$ simulated at $T_f = 0.01$ K. It can be clearly seen that the spin is in a continuous rotation as R increases. This confirms the incommensurability of the spin configuration due to the distorted

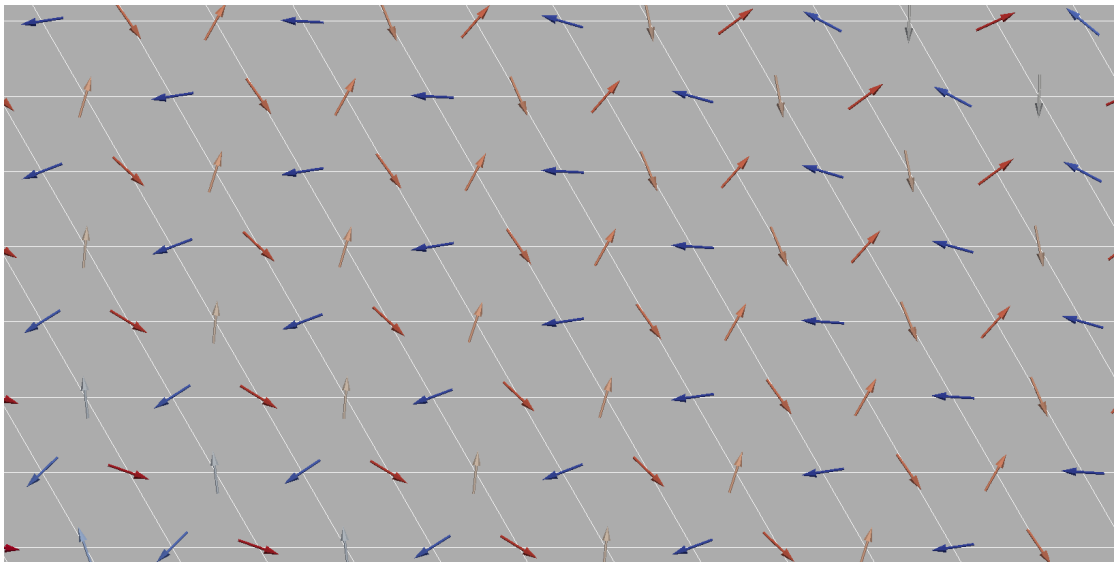

FIG. 3.2. GS spin configuration at $T_f = 0.01$ K. We plot each spin as $(S_z, S_y, 0)$ in the ab plane of $CuCrO_2$ for simplicity.

crystal structure. Our simulated $G(R,T)$ is very close to that calculated theoretically in the infinite lattice according to the following formula

$$G_{theo}(R,T) = \cos(2R\pi k_{inf}) \tag{3.5}$$

with $k_{inf} = 0.3225$ calculated by Eq. (2.24) with neglecting the effect of J_2 and J_3. Concerning the degree of geometric magnetic frustration of the simulated GS, the simulated value of Eq. (1.12) at $T_f = 0.01$ K gives $F_{sim} = 0.541$ which reflects a highly frustrated magnetic configuration.

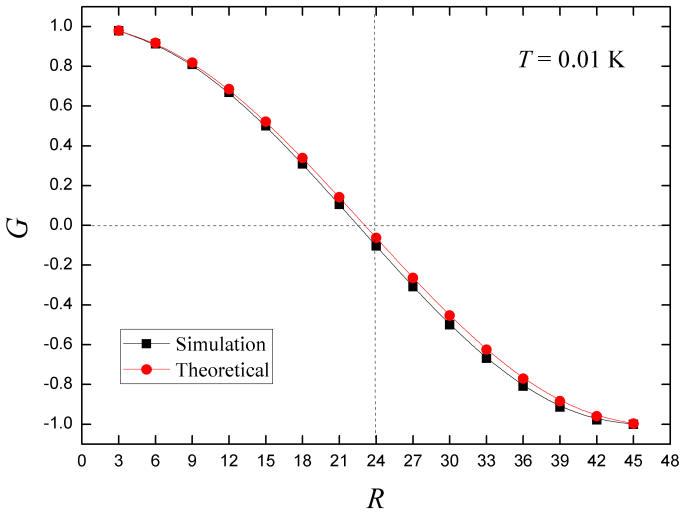

FIG. 3.3. Variation of the spin-spin correlation function versus the distance (in a units) simulated with the set of $d = 0.003$ along the [100] direction at $T_f = 0.01$ K in $CuCrO_2$.

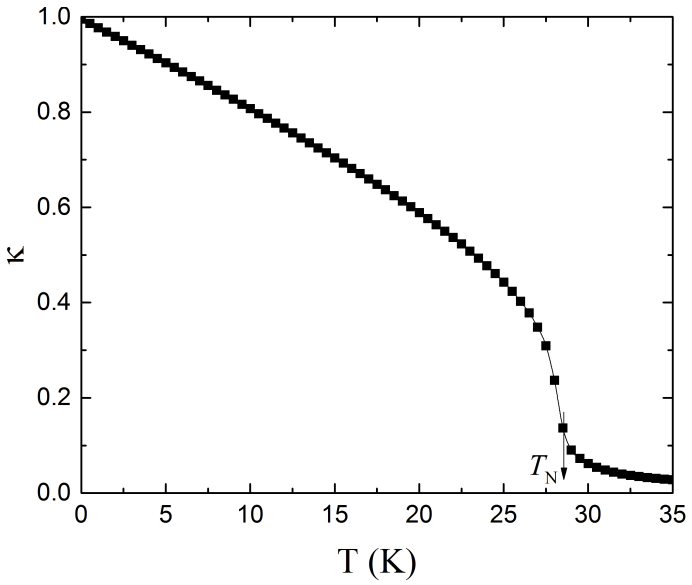

FIG. 3.4. Temperature dependence of the order parameter simulated with the set of $d = 0.003$ in $CuCrO_2$.

To characterize more precisely the magnetic ordering and the nearly $120°$ GS configuration, we consider the spin chirality defined in Eq. (2.15) to be the order parameter in our system. Fig. 3.4 shows the thermal variation of the order parameter where we can see that spin ordering starts to take place below $T_N \approx 28.5$ K. At $T = T_f$, $\kappa \approx 0.995$ indicates a small deviation from the commensurate $(120°)$ configuration of $\kappa = 1$. We compare $\kappa(T_f)$ with the theoretical value κ_{theo} — assuming all the spins are in the same spiral plane in the regular magnetic configuration — corresponding to $k_{sim} = 0.322$ according to the following formula

$$\kappa_{theo} = \frac{2}{3\sqrt{3}} \{2\sin(2\pi k_{sim}) - \sin(4\pi k_{sim})\} \tag{3.6}$$

We find that $\kappa_{theo} \approx 0.995$ which corresponds exactly to $\kappa(T_f)$. This means that our simulations converge toward the true magnetic configuration having the yz plane as the spiral plane of the system.

On the other hand, within our MC simulations, we simulate the temperature dependence of the specific heat per spin based on Eq.(2.19) to estimate precisely the transition temperature in $CuCrO_2$. Fig. 3.5 shows the simulated temperature profile of the specific heat per spin where it shows a peak at $T_N = 28.5 \pm 0.5$ K that corresponds to a phase transition from a paramagnetic state to an antiferromagnetic state which is in a very good agreement with that reported experimentally $(T_N = 24 - 26$ K) [52, 66, 67]. To characterize well this phase transition it is very important to study the size effect on the peak of the specific heat. Fig. 3.6 shows the

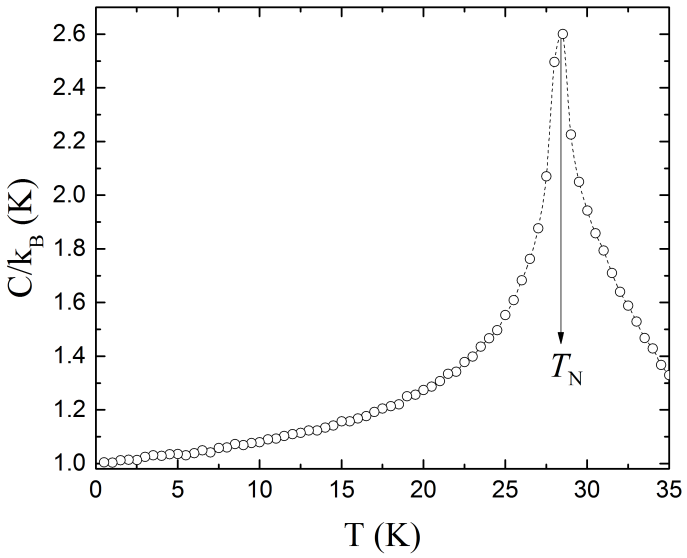

FIG. 3.5. Thermal variation of the specific heat per spin simulated with the set of $d = 0.003$ in $CuCrO_2$.

thermal variation of the specific heat per spin for various system sizes. We study the effect of varying L for a fixed $L_z = 3$ (left panel of Fig. 3.6) where we can clearly see the increase in the peak of C as L increases which indicates the presence of long range ordering within the ab plane. However, the C-peak is not affected (within statistical errors) by the variation of L_z for a given $L = 90$ as shown in the right panel of Fig. 3.6. This confirms the quasi-two dimensional behavior $CuCrO_2$ and confirms that the magnetic ordering in this delafossite is found to be within the ab plane. Thus it is also important to study the size effect on the energy of the system at the GS as well as at finite temperatures. Fig. 3.7 shows the temperature dependence of the internal energy per spin simulated for different choices of L and L_z. It is clearly seen that the internal energy is insensitive for size variation. Table 3.7 presents the simulated values of $U(T_f)/k_B$,

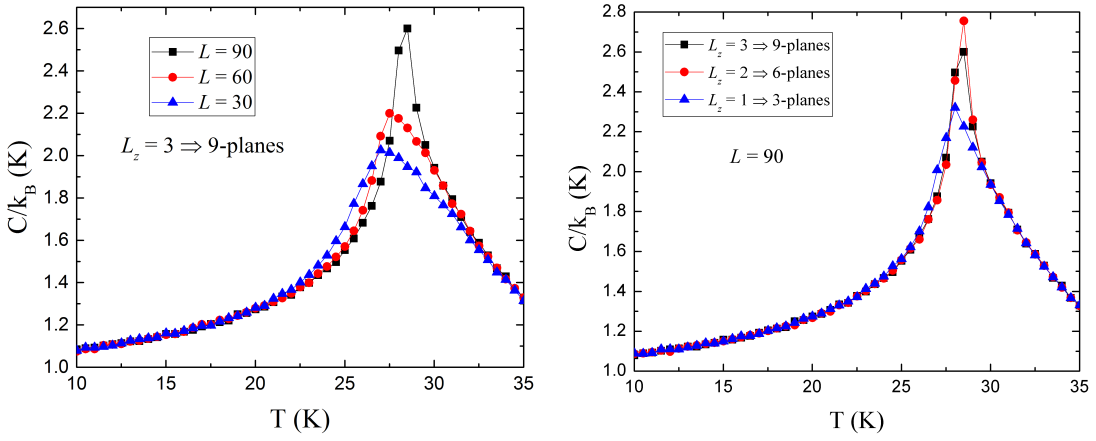

FIG. 3.6. Size dependence of the thermal variation of the specific heat per spin simulated with the set of $d = 0.003$ for various system sizes in $CuCrO_2$.

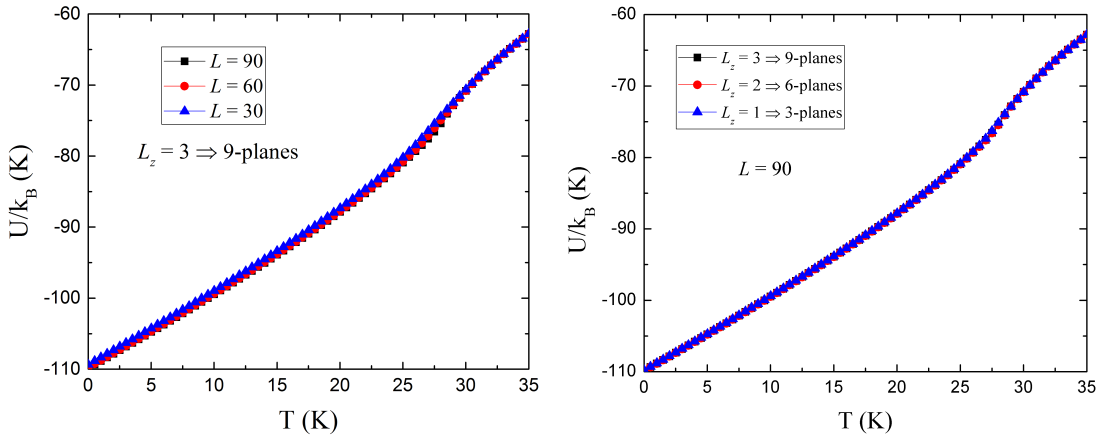

FIG. 3.7. Size dependence of the thermal variation of the internal energy per spin simulated with the set of $d = 0.003$ for various system sizes in $CuCrO_2$.

$\kappa(T_f)$, $\vec{q} = (h, k, 0)$ for each size at $T_f = 0.01$ K as well as their corresponding T_N. From the simulation results presented in Table 3.7, one can see that $U(T_f)/k_B$ as well as $\vec{q}$ slightly vary with varying L while they are roughly not affected by the variation of L_z. The simulated value of the order parameter κ at $T_f = 0.01$ K shows no significant L or L_z dependence. About the transition temperature T_N, a small shift of the peak of the specific heat curves (Fig. 3.6) can be seen but remains within the limit of 1 K. Therefore, we can say that there exists no significant size dependence of our results at finite temperatures while the GS configuration is sensitive to the choice of L.

Finally, we conclude that the choice of the simulation box can't be arbitrary when one aims to study the true GS configuration of $CuCrO_2$ due to the significant effect of PBCs on the magnetic configuration of the GS ($\vec{q}$). Thus the choice of L that corresponds to one of the minima in Fig. 2.6 is very important for the convergence of the simulated GS toward the theoretical one whatever the choice of L_z. Also, from the accordance of the simulation results with the theoretical calculations (GS energy and chirality) as well as the experimental observations, we can deduce the validity of our DFT estimates for the exchange interactions and single ion anisotropy constants.

TABLE 3.7. Size effects on the GS configuration and the phase transition in $CuCrO_2$.

Size	N	$U(T_f)$/k$_B$ (K)	$\kappa(T_f)$	$\vec{q} = (h, k, 0)$	$T_N \pm 0.5$ (K)
$30 \times 30 \times 3$	8 100	-109.329	0.999	$(0.333, 0.333, 0)$	27.0
$60 \times 60 \times 3$	32 400	-109.753	0.995	$(0.333, 0.317, 0)$	27.5
$90 \times 90 \times 3$	72 900	-109.856	0.995	$(0.322, 0.322, 0)$	28.5
$90 \times 90 \times 2$	48 600	-109.868	0.995	$(0.322, 0.322, 0)$	28.5
$90 \times 90 \times 1$	24 300	-109.790	0.995	$(0.322, 0.322, 0)$	28.0

3.2.1.2 Ferroelectric properties

To study the ferroelectric properties in $CuCrO_2$, we apply the extended inverse DM model given by Eq.(1.53). As discussed in Sec. 1.3, only the second term of Eq.(1.53) ($\vec{p}_2$) contributes to the ferroelectric polarization in the proper-screw configuration. Thus, we simulate the thermal variation of the projection of $\vec{p}_2$ along the $[110]$ direction ($P_{[110]}$) to describe the ferroelectric nature of $CuCrO_2$. To measure a spontaneous ferroelectric polarization, we apply a poling electric field $E_x = \pm 450$ kV/m along the $[110]$ direction during the first 3×10^3 MCS (n_{elec}) to fix a unique helicity of all atomic planes, and then we turn it off to let the system relax to its equilibrium position during the remaining 2×10^3 MCS of the *equilibration time* (n_0). Fig. 3.8 shows the thermal variation of $P_{[110]}$ which starts to emerge at T_N. Also it can be seen that by switching the direction of the poling electric field, $P_{[110]}$ is reversed. This confirms the electric control of spin helicity discussed in Ref. [12]. Further insight into the ferroelectric nature of our system may be gained through the study of the P-E hysteresis loops. The simulations of the hysteresis loops are done using the time step quantified MC method with the Metropolis algorithm as explained in Sec. 2.2.2.2. Before proceeding in explaining the ferroelectricity in our system, it is very important to investigate the effect of the physical time Δt corresponding to 1 MCS. To do so, we simulate the P-E hysteresis loops at $T = 5$ K for various values of R. As usual, the system is cooled from $T_i = 35$ K to $T = T_{loop} = 5$ K under a poling electric field $E_{poling} = 300$ kV/m applied during the first 3×10^3 MCS of n_0 to choose a unique helicity

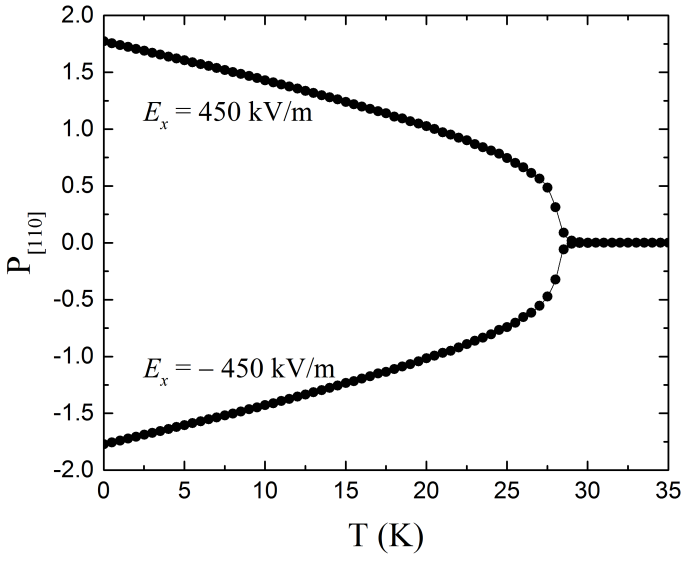

FIG. 3.8. Temperature dependence of the ferroelectric polarization simulated along the $[110]$ direction with the set of $d = 0.003$ in $CuCrO_2$.

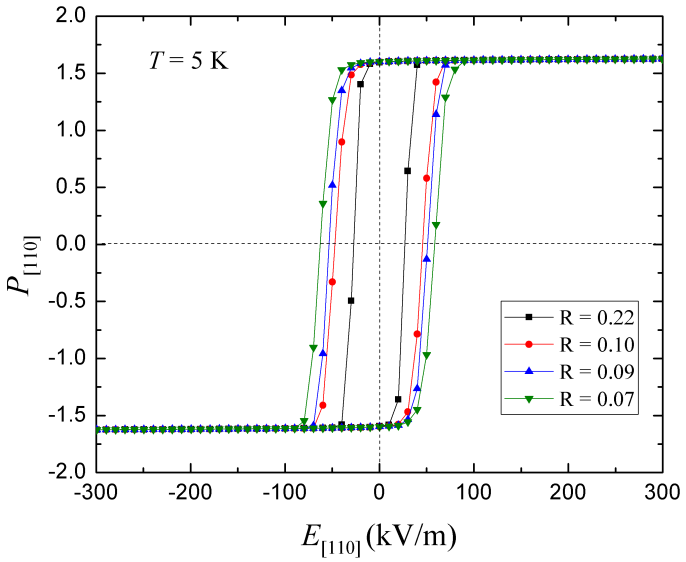

FIG. 3.9. P-E hysteresis loops simulated at $T = 5$ K with the set of $d = 0.003$ for different values of R in $CuCrO_2$.

for all the planes. At $T = T_{loop}$, we apply E_{poling} at every MCS and we start decreasing E progressively by a constant field step $\Delta E = 10$ kV/m to reach $E = -E_{poling}$ and then we increase this field by the same field step ΔE to reach again E_{poling}. At each field step, we perform 5.5×10^4 MCS with discarding $n_0 = 5 \times 10^3$ for equilibrium considerations. Fig. 3.9 shows the hysteresis loops simulated at $T = 5$ K for various values of R. It shows that the reversal field of $P_{[110]}$ decreases as R increases. Table 3.8 shows the values of the simulated reversal electric field (E_r) for $P_{[110]}$ for various R with their corresponding measuring time associated to 1 MCS calculated according to Eq. (2.11). As expected, the reversal field increases as the measuring time decreases, i.e., R decreases. This is because the probability to rotate the spins at each field step decreases with the decrease of the measuring time. However, decreasing R too much will make the algorithm inefficient. We find that the loop that corresponds to $R = 0.09$ shows an electric coercive field $E_r \approx 5.3 \times 10^{-2}$ MV/m very close to that measured experimentally ($E_r = 5.1 \times 10^{-2}$ MV/m [91]). Therefore we fix $R = 0.09$ in our simulations for further

TABLE 3.8. The effect of varying R on the reversal electric field of $P_{[110]}$ simulated at $T = 5$ K.

R	Δt (s)	E_r (MV/m) at $T = 5$ K
0.22	1.12×10^{-14}	2.7×10^{-2}
0.10	2.29×10^{-15}	4.6×10^{-2}
0.09	1.72×10^{-15}	5.3×10^{-2}
0.07	1.15×10^{-15}	6.1×10^{-2}

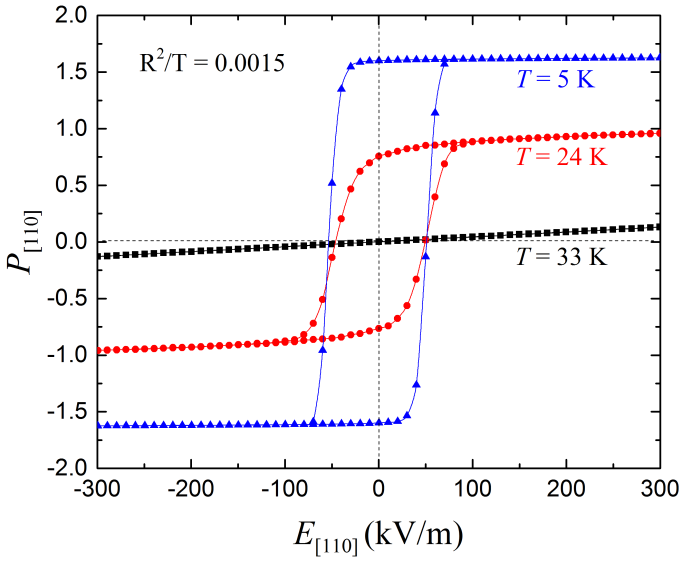

FIG. 3.10. P-E hysteresis loops simulated with the set of $d = 0.003$ at different temperatures in $CuCrO_2$.

investigations. It is worth noting that the reversal of $P_{[110]}$ results from the reversal of the helicity of each ab atomic plane.

After that we simulate the P-E hysteresis loops at different temperatures (Fig. 3.10) for a better understanding of the induced ferroelectricity in $CuCrO_2$. $P_{[110]}$ shows a linear E dependence without hysteresis above T_N because the system is in the paraelectric phase, while clear hystereses are seen for temperatures below T_N. Also one can see that the reversal electric field as well as the saturation electric field are roughly independent of the temperature below T_N.

3.2.2 Study under applied magnetic fields

3.2.2.1 Antiferromagnetic nature of $CuCrO_2$

Here we investigate the M-B hysteresis loops for B applied along the $[110]$ and $[1\bar{1}0]$ directions. As usual, we start our simulations from initial random spin configurations at $T_i = 35$ K. We then cool down to $T_{loop} = 5$ K with a constant temperature step $\Delta T = 1$ K. At $T = T_{loop}$, we apply a magnetic field $B = 5$ T and we start decreasing B with a constant field step $\Delta B = 0.5$ T to reach $B = -5$ T. At $B = -5$ T, we then increase B by the same field step to reach again $B = 5$ T. At each field step we apply $n_{MCS} = 5.5 \times 10^4$ with discarding $n_0 = 5 \times 10^3$ for equilibrium considerations. Note that each hysteresis is an average of 10 different random configurations. It can be seen that the magnetization measured along the applied magnetic field shows a linear dependence without hysteresis whatever the direction of B. This confirms the

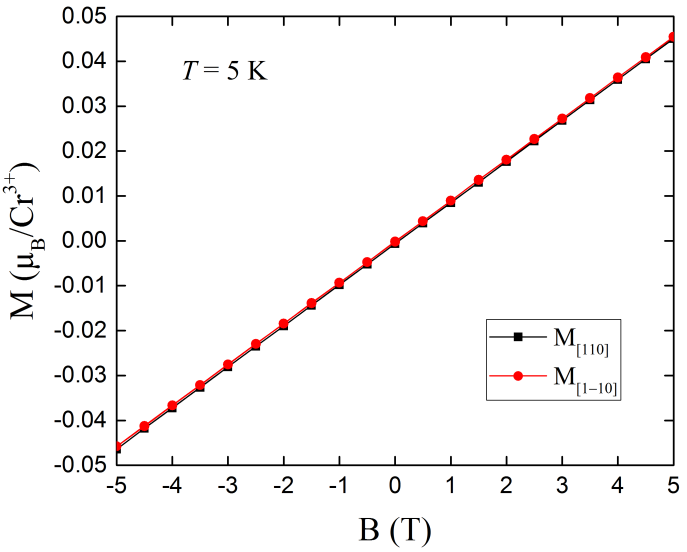

FIG. 3.11. Magnetic field dependence of the magnetization simulated with the set of $d = 0.003$ at $T = 5$ K in $CuCrO_2$.

antiferromagnetic nature of $CuCrO_2$ and is consistent with the magnetic measurements done in Refs. [67, 91].

3.2.2.2 Curie-Weiss behavior

We start this set of simulations from random spin configurations at $T_i = 300$ K and we then cool down to $T_f = 2$ K with a constant temperature step $\Delta T = 2$ K. Thus each curve of these simulations is composed of $n_{Temp} = 150$ temperatures. Then it is impossible to use the same size as before $(90 \times 90 \times 3)$ because we cannot exceed $t_{sim} = 300$ hours*. Therefore we need to decrease either n_{MCS} or N. And because decreasing n_{MCS} would increase the statistical errors, we then choose to decrease N through decreasing L_z preserving the same L. Magnetic properties under 0.3 T applied along the [110] direction were simulated between 300 K and 2 K to estimate the Curie-Weiss temperature θ_{CW} of $CuCrO_2$. The simulation parameters are given in Table 3.9. Fig. 3.12 shows the variation of the magnetization and inverse susceptibility measured along the applied magnetic field. It can be seen that $1/\chi$ obeys well

*The maximum simulation time available at CRIANN is 300 hours.

TABLE 3.9. MC simulation parameters used in the study of the magnetic properties of $CuCrO_2$ under 0.3 T magnetic field.

Simulation parameters								
Size	N	T_i (K)	ΔT (K)	T_f (K)	n_{Temp}	n_{conf}	n_{MCS}	n_0
$90 \times 90 \times 1$	24 300	300	2	2	150	28	1.05×10^5	5×10^3

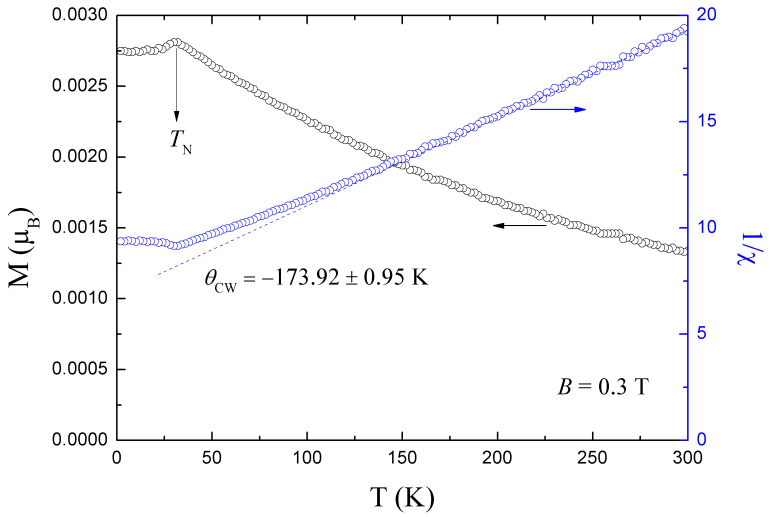

FIG. 3.12. Temperature dependence of the magnetization per spin and the inverse susceptibility simulated with the set of $d = 0.003$ under $B = 0.3$ T in $CuCrO_2$.

the Curie-Weiss law for antiferromagnets (Eq. 1.38) at high temperatures. The extrapolation of the high temperature part of the $1/\chi$ plot gives $|\theta_{CW}| \approx 173.92$ K which is very close to that measured experimentally ($\theta_{CW} = 160 - 170$ K) [52, 119]. However, by applying Eq. (1.48) with replacing J_1 by $(J_1' + 2J_1)/3$ and $S(S+1)$ by S^2 (because we treat the spins classically) we get $|\theta_{CW}| = 140.77$ K which is not far from both the simulated and the experimental values of θ_{CW}.

The $1/\chi$ curve starts to deviate from the linear behavior at about 100 K. In order to precise the origin of this deviation we calculated the temperature dependence of the spin-spin correlation function according to Eq. (2.16) along the [100] direction. As shown in Fig. 3.13, short-range

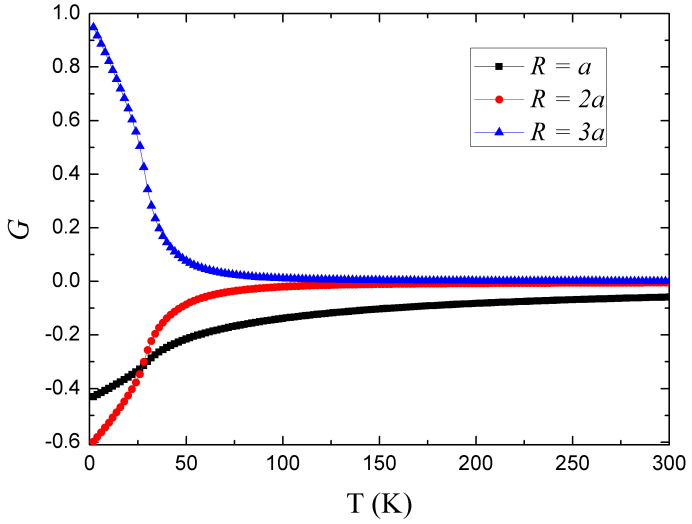

FIG. 3.13. Temperature dependence of the spin-spin correlation functions simulated with the set of $d = 0.003$ along the [100] direction in $CuCrO_2$.

antiferromagnetic correlations start to develop below ~ 100 K, which leads to the deviation from the Curie-Weiss law seen in Fig. 3.12. Furthermore, these correlation functions exhibit inflection points close to T_N estimated from the specific heat curve (Fig. 3.5). Besides, an anomaly in the magnetization curve (Fig. 3.12) appears at 30 ± 2 K consistent with our estimate of T_N from the specific heat curve (Fig. 3.5). The ratio $f = |\theta_{CW}| / T_N \approx 6.1$ ($\gg 1$) confirms the frustrated nature of $CuCrO_2$ as discussed in Sec. 1.1.5.

3.2.3 Domain stability under the effect of applied magnetic fields

In this part of our study, we are going to investigate the effect of applied magnetic fields ($\vec{B}$) on the stability of magnetic domains in $CuCrO_2$. As explained in Sec. 1.2.3, the nearly 120° spin configuration is triply degenerate, and those three magnetic domains coexist in the system with three corresponding spiral-planes making an angle about 120° between each others. In the absence of any external field, these three magnetic domains, denoted by the A, B and C, are equiprobable to exist with the same volume and the same energy. It was supposed that an applied magnetic field in the ab plane can stabilize one kind of the domains more than the others depending on the direction of the applied magnetic field [13, 65, 91]. Accordingly, it was predicted that when $\vec{B}$ is applied along the $[110]$ direction, the domain with the spiral plane parallel to the (110) plane is stabilized, i.e., the A-domain. Such prediction of domains rearrangement can explain the increase of the ferroelectric polarization measured along the $[110]$ direction reported in Ref. [65]. On the other hand, it was supposed that when $\vec{B}$ is applied along the $[1\bar{1}0]$ direction, the A-domain will become less stable and that at a certain value of $\vec{B}_{[1\bar{1}0]}$ ($B_{flop} \approx 5.3$ T), domain A will flip to become perpendicular to the direction $\vec{B}_{[1\bar{1}0]}$, i.e., D-domain as illustrated in Fig. 1.23.

Therefore, to discuss all the above mentioned predictions quantitatively, we need to consider the domain configuration of our spin structure (Fig. 1.21). However, it is still difficult to model such spin structure in the presence of lattice distortion. This is because we need to have the three types of domains and thus three distorted directions corresponding to three hard axes in the same simulation which is very complicated to implement in our model. However, instead of taking the three domains at the same time and study the effect of applying $\vec{B}$ along the $[110]$ direction for e.g., we will deal only with the A-domain and study its stability under the effect of changing the direction of $\vec{B}$ as shown in Fig. 3.14. Based on this model, we apply $\vec{B}$ along the $[110]$ and the $[1\bar{1}0]$ directions to study the stability of A-domain under $\vec{B}_{[110]}$ and $\vec{B}_{[1\bar{1}0]}$, respectively. After that we apply $\vec{B}$ along the $[010]$ direction to study the stability of A-domain under this field which

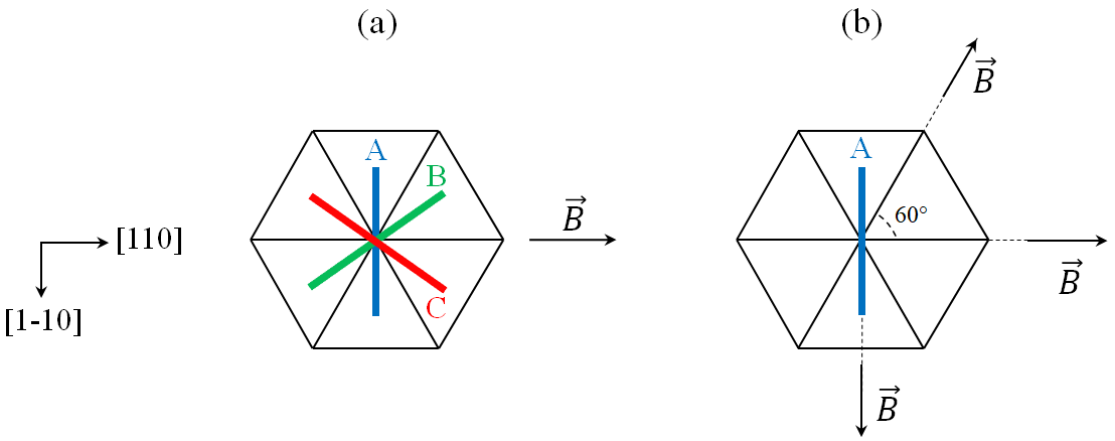

FIG. 3.14. Schematic representation of the three magnetic domains A, B and C under an applied magnetic field: along the $[110]$ direction (a), and the magnetic field directions with respect to the A domain in our simulations (b).

is equivalent to the stability of B or C-domains under $\vec{B}_{[110]}$ (Fig. 3.14b). The simulations pursue the following procedure: we take the system from a random spin configuration at $T_i = 35$ K and we slowly cool down to $T_f = 0.01$ K according to $T_{i+1} = \alpha T_i$ with $\alpha = 0.95$ under a field of 20 T. With this cooling process, the system stays longer time at low temperatures than at high ones providing a better accuracy on the GS energy but with longer simulation time. Because in this study we are not interested in studying the phase transition in the system, we are able to decrease n_{MCS} than that used in the previous investigations. The parameters of the simulations are given in Table 3.10.

The thermal variation of the internal energy of the A-domain under the effect of an applied magnetic field along the $[110]$, $[010]$ and $[1\bar{1}0]$ directions is shown in Fig. 3.15. Despite of the small difference in the energies, but it still can be seen that the internal energy of the A-domain under the effect of $B_{[110]}$ is slightly lower than that under the effect of $B_{[010]}$. Thus, in terms of three domains interpretations, we could say that the A-domain is more stable than B and C-domains under the effect of $B_{[110]}$ as predicted in Refs. [13, 65, 91]. On the other hand, it can be also seen that the internal energy of the A-domain under the effect of $B_{[1\bar{1}0]}$ is slightly higher than that under the effect of $B_{[110]}$ which could give an evidence of the possibility of the destabilization of A-domain under the effect of the application of $\vec{B}$ along the $[1\bar{1}0]$ as assumed

TABLE 3.10. Simulation parameters used in the study of domain stability under the effect of magnetic fields in $CuCrO_2$.

Simulation parameters								
Size	N	T_i (K)	α	T_f (K)	n_{Temp}	n_{conf}	n_{MCS}	n_0
$90 \times 90 \times 1$	24 300	35	0.95	0.01	159	28	5.5×10^4	5×10^3

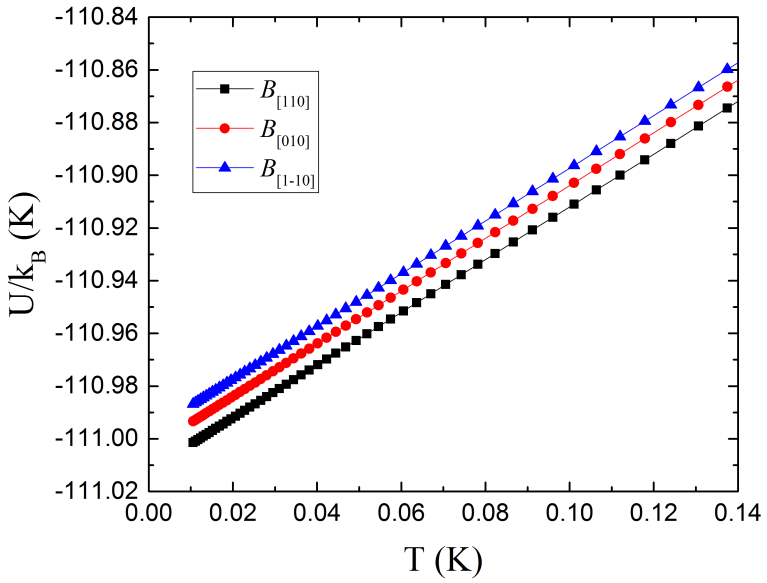

FIG. 3.15. Thermal variation of the internal energy per spin of the A-domain under an applied magnetic field along the [110], [010] and [1$\bar{1}$0] directions.

in Refs. [13, 65, 91]. Table 3.11 shows the values of the internal energy and the chirality of the A-domain at $T_f = 0.01$ K simulated under the effect of the various directions of the applied magnetic field. It can be seen that $\kappa(T_f)$ doesn't respond to the direction of the applied field. It preserves the same value whatever is the direction of $\vec{B}$. This shows that the magnetic field may stabilize one type of domains than the others without altering the magnetic configuration. Such magnetic field effect on the magnetic domains and consequently on the measured ferroelectric polarization measured along the [110] direction makes $CuCrO_2$ a rare example in terms of the magnetoelectric tunability by both magnetic and electric fields.

TABLE 3.11. Domain stability under the effect of $B = 20$ T in $CuCrO_2$.

	$B = 0$	$B_{[110]}$	$B_{[010]}$	$B_{[1\bar{1}0]}$
U_{GS}/k_B (K)	-109.769	-111.001	-110.993	-110.987
$\kappa(T_f)$	0.995	0.991	0.991	0.991

CHAPTER 4

Effect of Ga doping in $CuCrO_2$

In this chapter we investigate, by means of MC simulations the effect of magnetic dilution on the magnetic and ferroelectric properties of $CuCrO_2$. Some of these effects have been studied experimentally for several series of $CuCr_{1-x}M_xO_2$, where M^{3+} is a non-magnetic cation of $S = 0$ ($M^{3+} = Al^{3+}$, Ga^{3+}, Sc^{3+} and Rh^{3+}) [98]. It was shown that the homogeneity of substitution depends on the dopant M^{3+}. Since both Cr^{3+} and Ga^{3+} possess very close radii ($r_{Cr^{3+}} = 61.5$ pm and $r_{Ga^{3+}} = 62$ pm), we choose to study the case of $CuCr_{1-x}Ga_xO_2$ because it allows us to investigate the effect of pure magnetic dilution (for small Ga fractions) without steric effect like the other dopants. With our results we try to explain some experimental predictions and provide better understandings of the magnetoelectric properties of the diluted $CuCrO_2$.

Because DFT calculations (Appendix A) show no pronounced effect of Ga^{3+} doping on the exchange interactions in the system as well as no structural modifications, we safely replace a certain fraction x of Cr^{3+} by $S = 0$ sites randomly through the whole system. With the set of exchange interactions and single ion anisotropy constants corresponding to $d = 0.003$, we simulate the magnetic and ferroelectric properties of $CuCr_{1-x}Ga_xO_2$ for $x = 0, 0.02, 0.05, 0.1, 0.15, 0.2,$ and 0.3. Since we showed in chapter 3 that the effect of J_4 is very small and that the system has a quasi-two dimensional behavior, we will perform these sets of simulations on 2D lattices for time considerations. Note that our MC simulations are performed with and without applied magnetic fields to get a more clear picture on the diluted $CuCrO_2$ as discussed below.

4.1 Study without applied magnetic fields

4.1.1 Ground state configuration and phase transition

Typically, we start our simulations from random spin configurations at a high enough temperature ($T_i = 35.01$ K) above the transition temperature of the system. We then slowly cool down to a final temperature $T_f = 0.01$ K according to $T_{i+1} = T_i - \Delta T$. We consider a 2D system of size 90×90. At each temperature step, we perform $n_{MCS} = 1.05 \times 10^5$ MCS with discarding the first 5×10^3 MCS for thermal equilibration. Note that our results are averaged over 112 simulations with different random configurations. The parameters of simulations are listed in Table 4.1.

Fig. 4.1 shows the thermal variation of the internal energy per spin simulated for various fractions x. It can be seen that the internal energy per spin of the system increases as x increases due to the loss in the magnetic interactions caused by the introduced defects. In particular, it can be seen that starting from $x = 0.2$ the inflection point in the internal energy curve disappears. Fig. 4.2 shows the variation of the internal energy per spin versus x at $T_f = 0.01$ K where it shows a linear x-dependence of $U(T_f)$. To compare the simulated GS configuration with the ICY state, we calculate E_{ICY} in the infinite system of $CuCr_{1-x}Ga_xO_2$ such as

$$\begin{aligned} E_{ICY}(k_{inf}) &= -S^2(1-x)[2J_1\cos(2\pi k_{inf}) + J_1'\cos(4\pi k_{inf}) + 2J_2\cos(6\pi k_{inf}) + J_2 \\ &\quad + 2J_3\cos(4\pi k_{inf}) + J_3\cos(8\pi k_{inf}) + \frac{1}{2}D_z] \end{aligned} \tag{4.1}$$

where $k_{inf} = 0.3225$ as given in Sec. 2.3. It can be seen that $U(T_f)$ is below E_{ICY} for $x \neq 0$. This means that the ICY state presented in the pure $CuCrO_2$ is no more the stable configuration in $CuCr_{1-x}Ga_xO_2$. On the other hand, we calculate the parameter F – the degree of magnetic frustration given in Eq. (1.12) – which shows that the frustration of the GS configuration slightly decreases with increasing x but remains high in the system as shown in Fig. 4.3.

Then the question arises now is that, what is the nature of these diluted antiferromagnets? To

TABLE 4.1. MC simulation parameters used in the study of phase transition and GS configuration in $CuCr_{1-x}Ga_xO_2$.

Simulation parameters								
Size	$N\ (x=0)$	T_i (K)	ΔT (K)	T_f (K)	n_{Temp}	n_{conf}	n_{MCS}	n_0
90×90	8 100	35.01	0.5	0.01	71	112	1.05×10^5	5×10^3

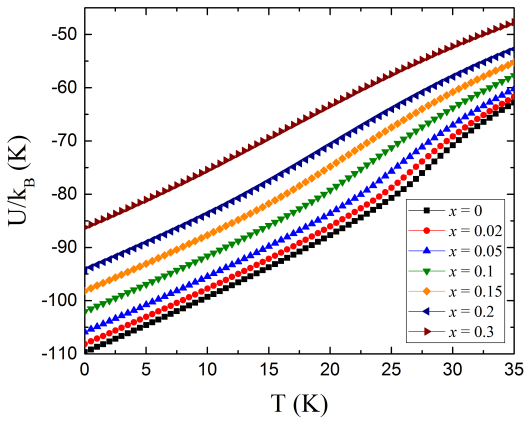

FIG. 4.1. Thermal variation of the internal energy per spin simulated in $CuCr_{1-x}Ga_xO_2$.

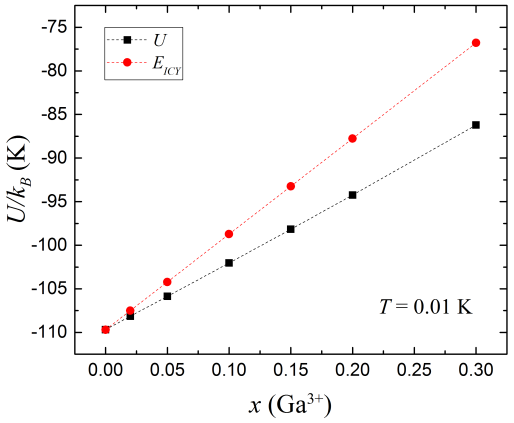

FIG. 4.2. Variation of the GS energy per spin compared to E_{ICY} as function of x in $CuCr_{1-x}Ga_xO_2$.

describe more precisely, we simulate the thermal variation of the specific heat per spin for the different fractions x (Fig. 4.4). It can be seen that the specific heat peak is rounded and shifts toward low temperatures with the increase of x up to 0.15. Starting from $x = 0.2$, no clear peak can be identified, but rather a broaden peak which suggests a loss in the long range magnetic ordering in the system. Hence it is very important to calculate the correlation functions for the various fractions. Fig. 4.5 shows the variation of the spin-spin correlation functions calculated along the $[100]$ direction at $T = 0.01$ K according to Eq. (2.16) for each fraction x. It can be clearly seen that the system preserves its long range ordering up to $x = 0.15$ and suddenly loses it at $x \geq 0.2$. This accords well with the broadening of the specific heat peak for $x \geq 0.2$ shown in Fig. 4.4. The loss in the long range ordering and hence the disordered spin structures can be

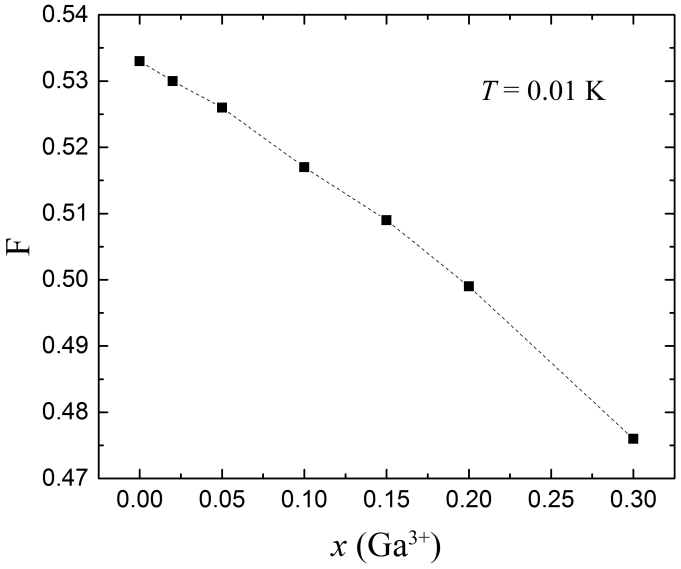

FIG. 4.3. Variation of the degree of magnetic frustration of the GS in $CuCr_{1-x}Ga_xO_2$.

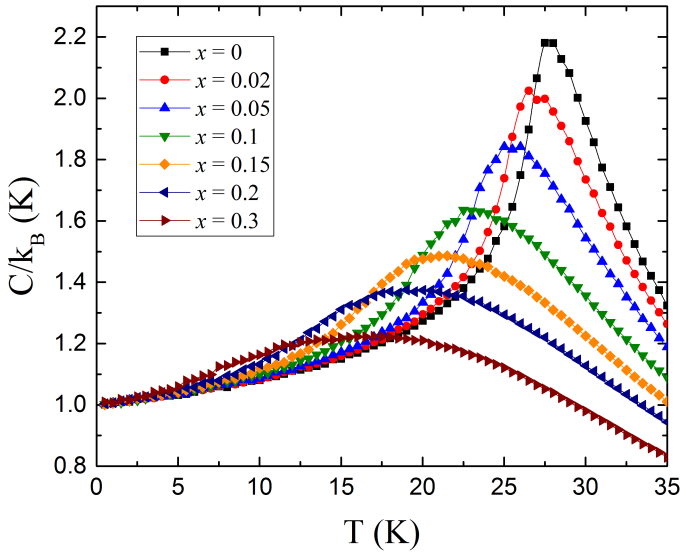

FIG. 4.4. Thermal variation of the specific heat per spin simulated in $CuCr_{1-x}Ga_xO_2$.

seen in Fig. 4.6 and Fig. 4.7. Beside the simulated correlation functions, it is very important to investigate the size effect on the specific heat peak in order to see whether these diluted systems still undergo phase transitions or not. For the same simulation parameters given in Table 4.1, we repeat the same sets of simulation for two different sizes of $L = 30$ and $L = 150$ beside the $L = 90$. Fig. 4.8 shows the temperature dependence of the specific heat per spin simulated for each fraction of x. It can be seen that the specific heat peak responds to the size variation till $x = 0.15$. Therefore, a long range ordering still exists in these diluted antiferromagnets.

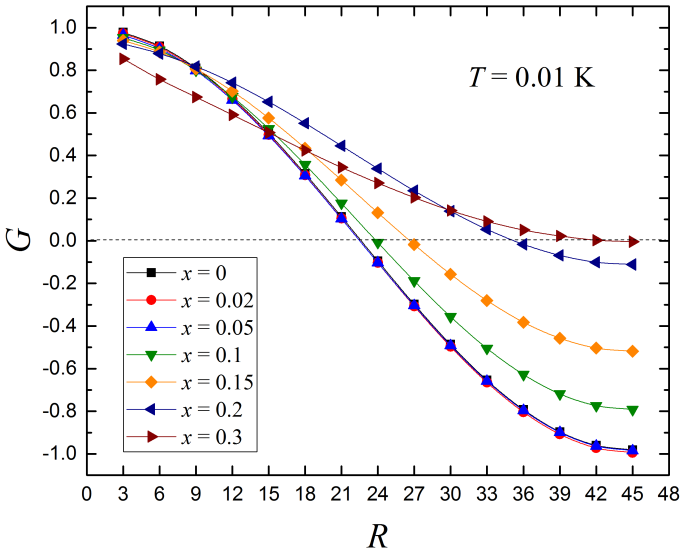

FIG. 4.5. Variation of the spin-spin correlation functions versus the distance simulated with the set of $d = 0.003$ along the $[100]$ direction at $T_f = 0.01$ K in $CuCr_{1-x}Ga_xO_2$.

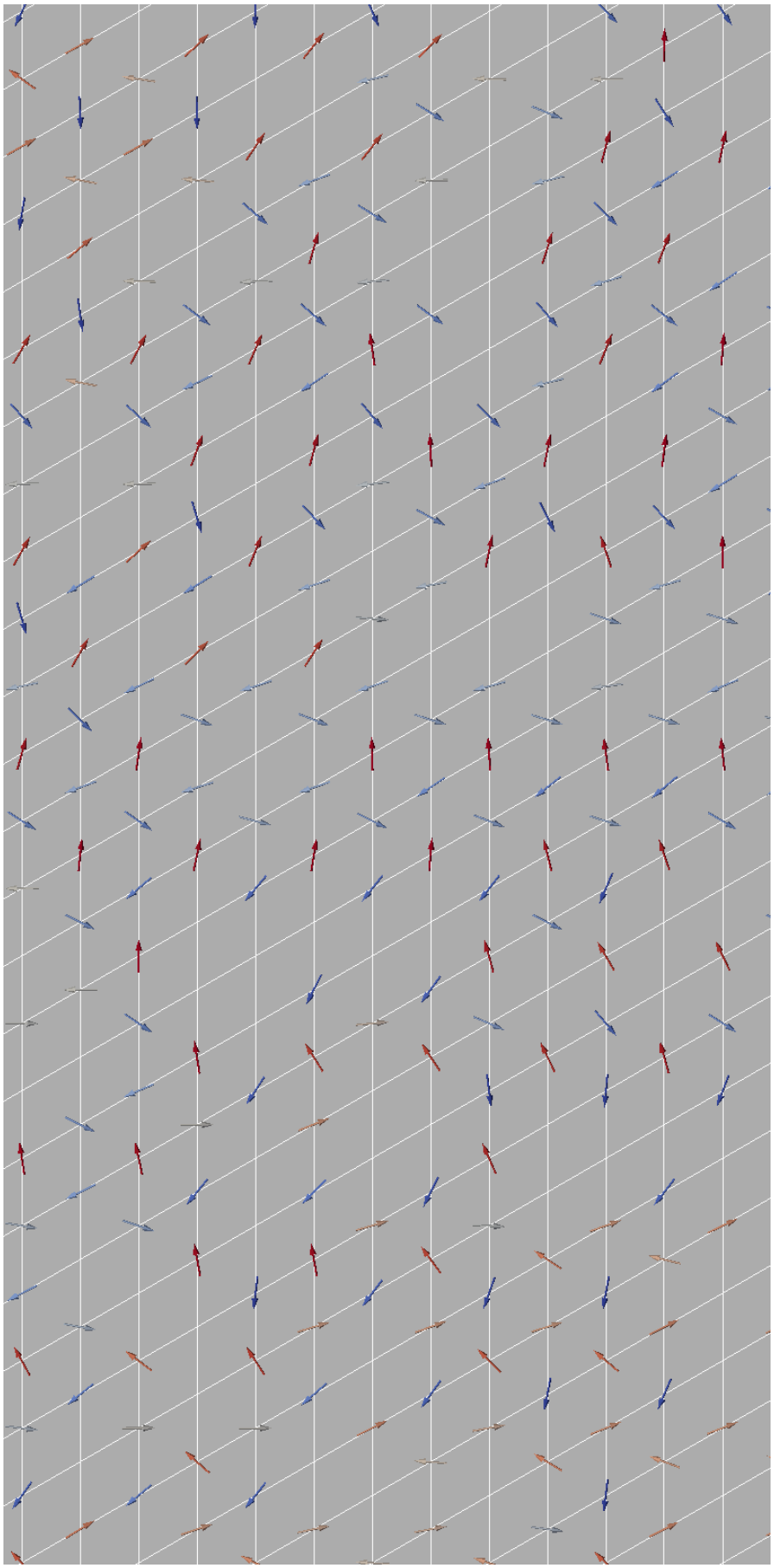

FIG. 4.6. One of the simulated GS spin configurations of $\mathrm{CuCr_{0.8}Ga_{0.2}O_2}$.

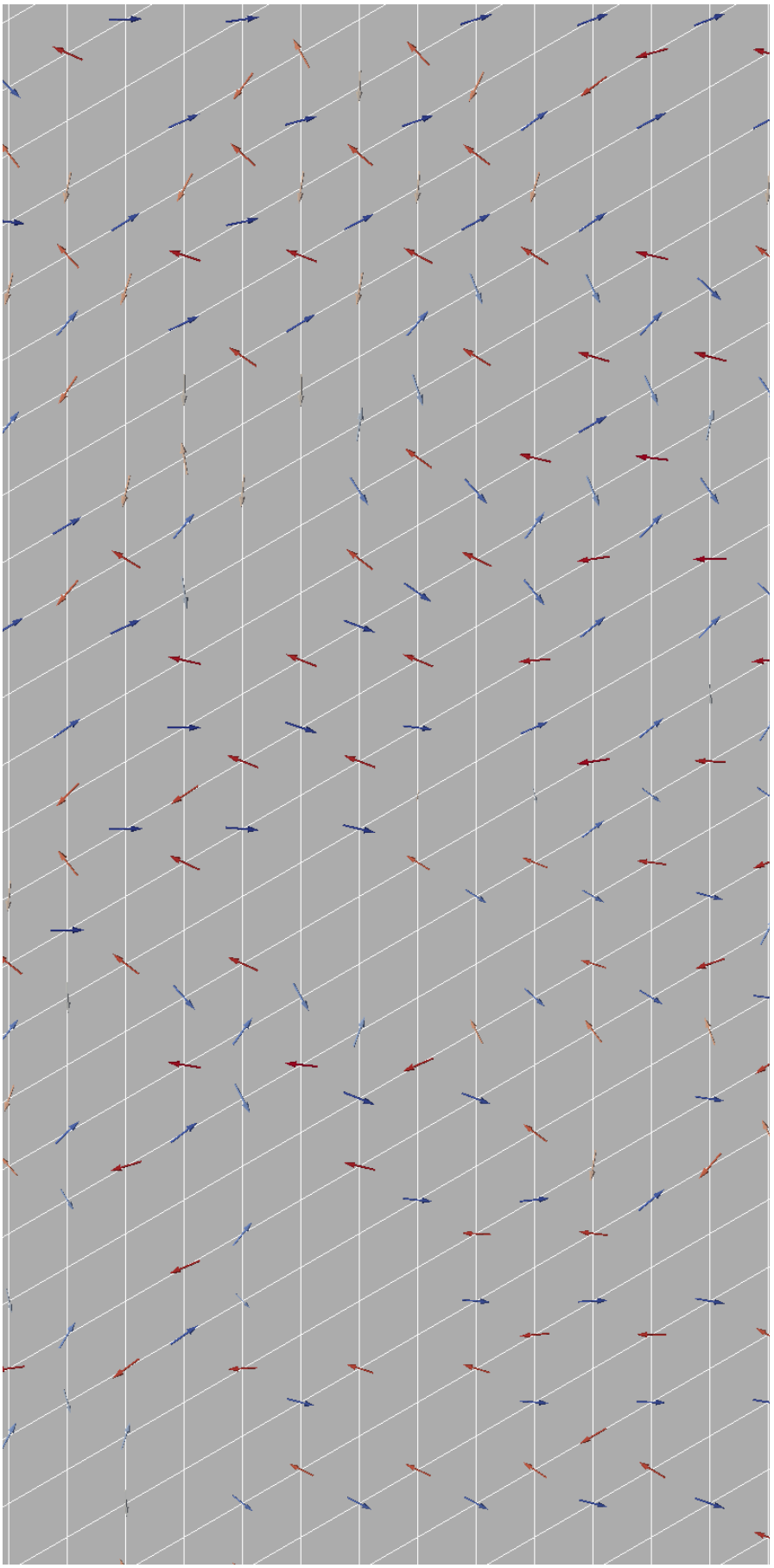

FIG. 4.7. One of the simulated GS spin configurations of $CuCr_{0.7}Ga_{0.3}O_2$.

However at $x \geq 0.2$, the specific heat peak doesn't increase with increasing the size which is consistent with the loss of the long range ordering seen in Fig. 4.5. Therefore at this stage we can say that the magnetic configurations for $x \geq 0.2$ are disordered (no more long range order). Thus in the presence of both frustration and disorder in the system (for $x \geq 0.2$) — the necessary ingredients for having a spin glass behavior — one can think about spin-glass-like behavior in the system and hence try to find some features that are able to describe such a freezing state. First of all, we can see that the low temperature part of the specific heat curve for $x = 0.3$ (Fig. 4.8f) varies quite linearly with T unlike that of $x = 0.2$ (Fig. 4.8e), which is a signature of a spin-glass-like behavior in diluted magnets [22]. Because the low temperature region of the specific heat curve in $CuCr_{0.7}Ga_{0.3}O_2$ may reflect a spin-glass-like behavior, and because its peak is broadened and doesn't respond to size variation, then the specific heat cannot characterize the phase transition and consequently the freezing temperature of the system.

On the other hand, it is curious to know where does the disorder of the spins take place. Do the system still possesses a spiral plane? To answer this question, we simulated the thermal variation of the spin chirality given in Eq. (2.15) and the components κ_x, κ_y and κ_z of Eq. (2.14) along the $[110]$, $[\bar{1}10]$ and $[001]$ directions, respectively. It can be seen that at $T_f = 0.01$ K for $x \leq 0.2$, $\kappa_y = \kappa_z \approx 0$ and $\kappa = \kappa_x$ (Fig. 4.9a–4.9e) which suggests that the spins are still confined within the yz spiral plane due to the effect of the hard-axis anisotropy. However, when $x = 0.3$ there exists a nonzero component of κ_y and that $\kappa_x < \kappa$ (Fig. 4.9f) which reflects the fact that the spins are no more confined in the same spiral plane.

To verify our previous interpretations, we calculate the thermal variation of the average of the absolute value of S_x, S_y and S_z according to

$$\langle\overline{|S_u|}\rangle_T = \frac{1}{N(n_{MCS} - n_0)} \sum_{\ell=n_0+1}^{n_{MCS}} \left(\sum_{i=1}^{N} |S_u^i| \right)_\ell \tag{4.2}$$

with $u = x, y, z$. It can be seen that the $\langle\overline{|S_x|}\rangle_T$ component falls to zero for $x \leq 0.2$ (Fig. 4.10) which is consistent with disappearance of κ_y and κ_z in the same compounds. This confirms that the spins are located in the yz spiral plane. Thus we can say that the magnetic configuration for $x = 0.2$ is disordered (nearly zero correlation) within the yz plane. However at $x = 0.3$, $\langle\overline{|S_x|}\rangle_T$ is now not null which means that the spins go out of the yz plane. This observation is consistent with the appearance κ_y component in $CuCr_{0.7}Ga_{0.3}O_2$.

Now we need to characterize the spiral spin ordering temperature for $x \leq 0.2$. It can be signaled at the temperature when $\kappa_x \neq 0$ ($x \leq 0.2$) as seen in Fig. 4.9a–4.9e. Since in these cases $\kappa = \kappa_x$,

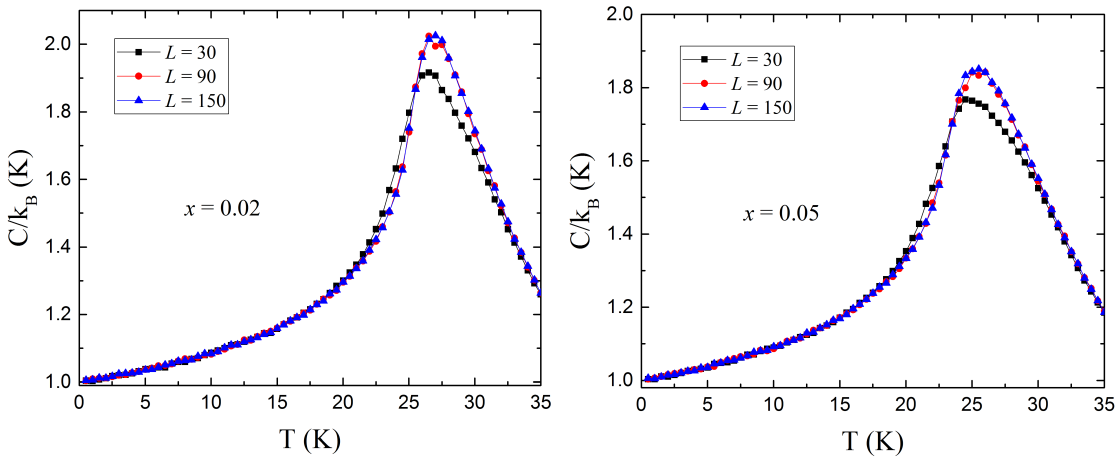

(a) $CuCr_{0.98}Ga_{0.02}O_2$

(b) $CuCr_{0.95}Ga_{0.05}O_2$

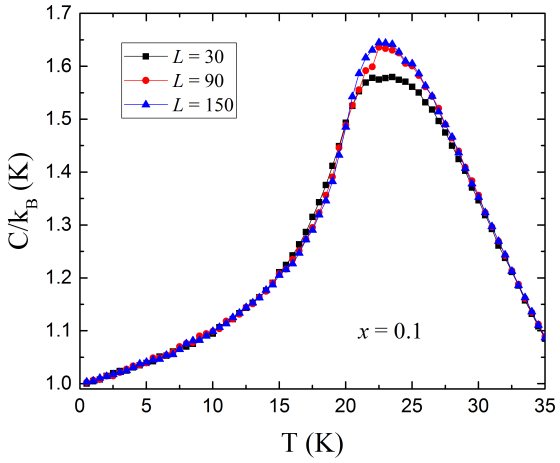

(c) $CuCr_{0.9}Ga_{0.1}O_2$

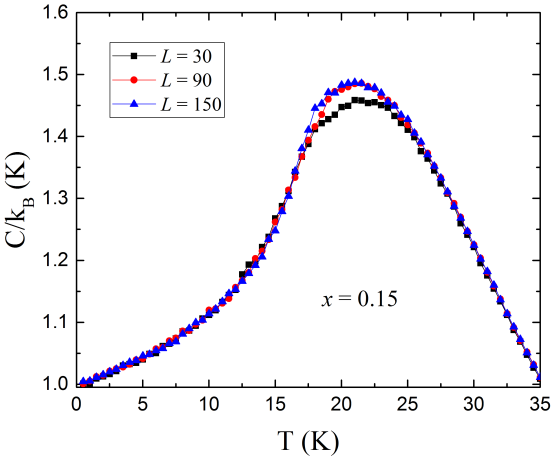

(d) $CuCr_{0.85}Ga_{0.15}O_2$

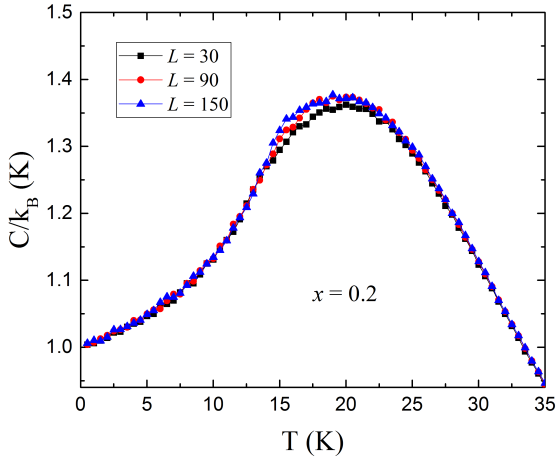

(e) $CuCr_{0.8}Ga_{0.2}O_2$

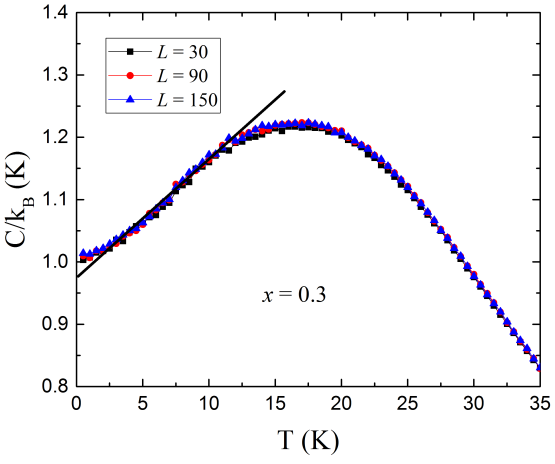

(f) $CuCr_{0.7}Ga_{0.3}O_2$

FIG. 4.8. Thermal variation of the specific heat per spin simulated with the set of $d = 0.003$ for various x in $CuCr_{1-x}Ga_xO_2$.

we define the parameter $\chi_\kappa = \langle\kappa^2\rangle - \langle\kappa\rangle^2$ according to Ref. [120] to be the chiral susceptibility which shows a peak at the spiral plane ordering temperature of the system. Fig. 4.11 shows the

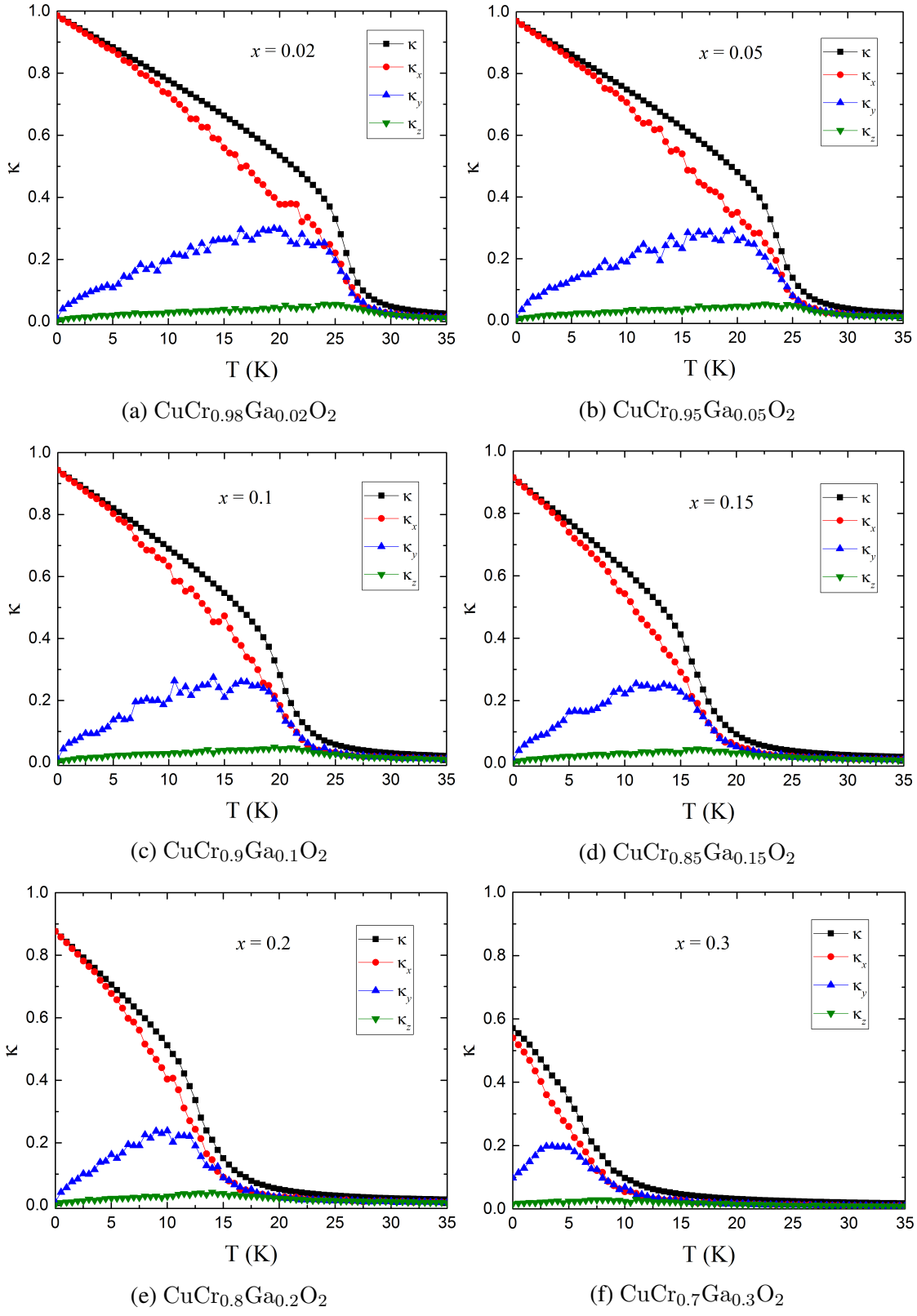

(a) $CuCr_{0.98}Ga_{0.02}O_2$ (b) $CuCr_{0.95}Ga_{0.05}O_2$

(c) $CuCr_{0.9}Ga_{0.1}O_2$ (d) $CuCr_{0.85}Ga_{0.15}O_2$

(e) $CuCr_{0.8}Ga_{0.2}O_2$ (f) $CuCr_{0.7}Ga_{0.3}O_2$

FIG. 4.9. Thermal variation of the spin chirality κ and its corresponding components $\kappa_{x,y,z}$ simulated with the set of $d = 0.003$ for various Ga^{3+} fractions in $CuCr_{1-x}Ga_xO_2$.

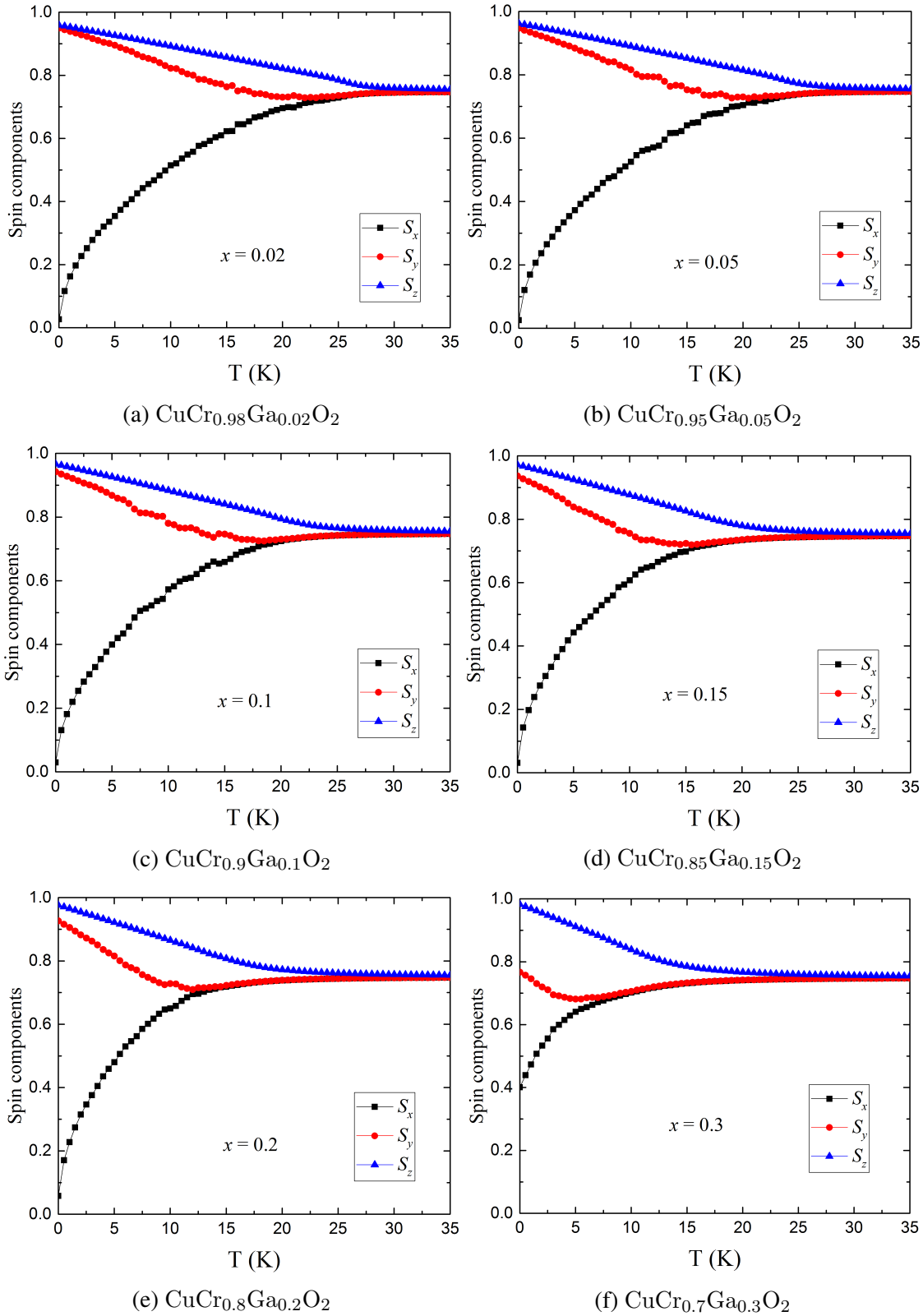

(a) $CuCr_{0.98}Ga_{0.02}O_2$ (b) $CuCr_{0.95}Ga_{0.05}O_2$

(c) $CuCr_{0.9}Ga_{0.1}O_2$ (d) $CuCr_{0.85}Ga_{0.15}O_2$

(e) $CuCr_{0.8}Ga_{0.2}O_2$ (f) $CuCr_{0.7}Ga_{0.3}O_2$

FIG. 4.10. Thermal variation of the average value of the x, y, z components of the spins simulated with the set of $d = 0.003$ for various Ga^{3+} fractions in $CuCr_{1-x}Ga_xO_2$.

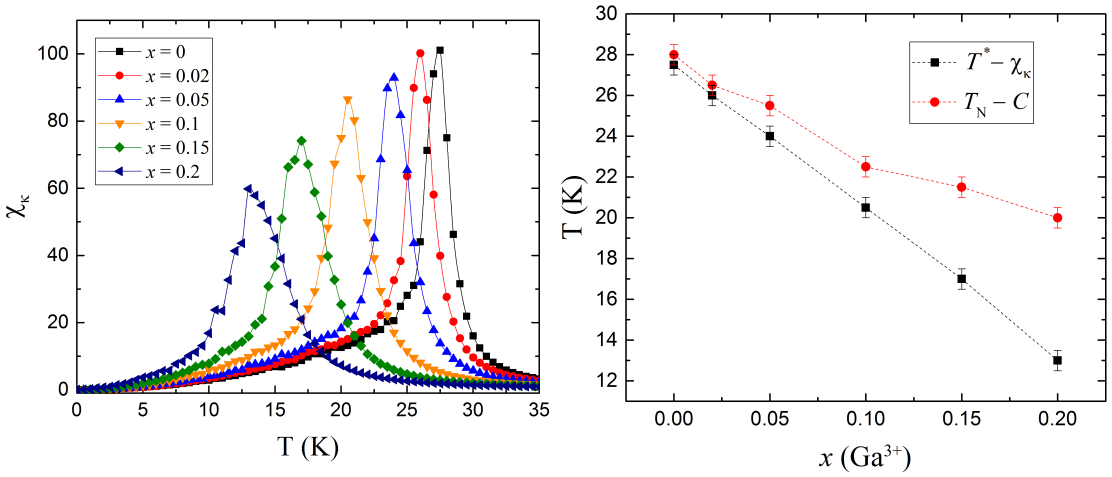

FIG. 4.11. Thermal variation of the chirality susceptibility χ_κ shows a peak at the ordering temperature (left panel), and the variation of the ordering temperature versus x deduced from χ_κ and C (right panel) simulated with the set of $d = 0.003$ for various Ga^{3+} fractions in $CuCr_{1-x}Ga_xO_2$.

thermal variation of χ_κ for $x \leq 0.2$ where we can see a clear peak at T^* when the spiral ordering starts to take place. T^* shows a linear variation with x (right panel of Fig. 4.11) which is roughly coherent with T_N deduced from the specific heat curves of Fig. 4.4 up to $x = 0.02$. At $x \geq 0.05$, $T_N > T^*$ which perhaps can be referred either to the presence of an antiferromagnetic state before spiral ordering or the presence of disordered states (for $x = 0.2$) and thus T_N deduced from C has no meaning. This needs the magnetization measurements to be validated.

Finally, we can say that $CuCr_{1-x}Ga_xO_2$ is antiferromagnetic when $x \leq 0.15$, disordered within the same spiral plane (yz plane) at $x = 0.2$ and shows a spin-glass-like behavior for $x = 0.3$.

4.1.2 Ferroelectric properties

As we show in the previous section, $CuCr_{1-x}Ga_xO_2$ preserves its spiral nature up to $x = 0.2$. Also since short range correlations still exist in the system, we can still apply the extended inverse DM model given by Eq.(1.53) to describe the emergence of spontaneous ferroelectricity in $CuCr_{1-x}Ga_xO_2$. For the same simulation parameters given in Table 4.1, we simulate the thermal variation of $P_{[110]}$ for the system when $x \leq 0.2$. Because here we perform our simulations on 2D lattices, it is not important to apply a poling electric field since the lattice will have a unique helicity. But since we average our results over many configurations, we then choose to average the absolute value of $P_{[110]}$ to avoid sum cancellations. Fig. 4.12 shows the temperature profile of $P_{[110]}$ simulated for each fraction x. It can be seen that $P_{[110]}$ decreases as x increases in the system. This decrease is caused by the loss of magnetic bonds and the destabilization

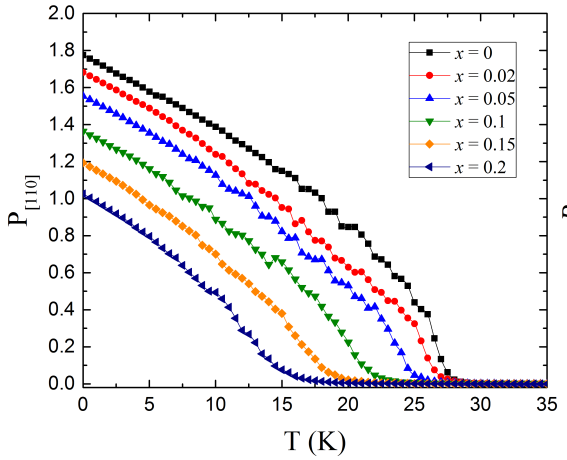

FIG. 4.12. Thermal variation of the ferroelectric polarization simulated along the [110] direction with the set of $d = 0.003$ in $CuCr_{1-x}Ga_xO_2$.

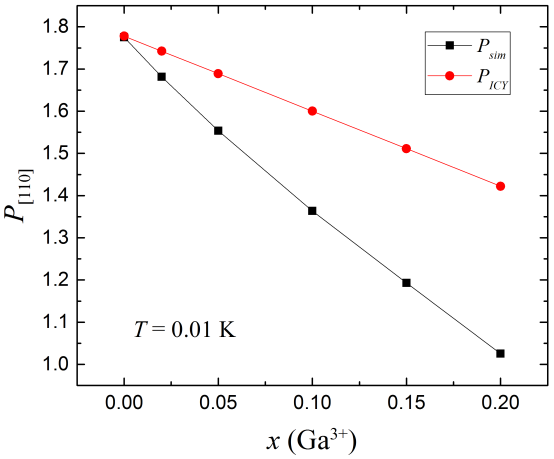

FIG. 4.13. Variation of $P_{[110]}$ versus Ga^{3+} fraction in comparison with P_{ICY} calculated in the ICY state in $CuCr_{1-x}Ga_xO_2$.

of the ICY state presented in the pure system. This can be seen clearly through the variation of $P_{[110]}(T_f)$ versus x in comparison to the theoretical value of $P_{[110]}$ in the infinite system as shown in Fig. 4.13. Denote by P_{ICY}, $P_{[110]}$ calculated in the ICY state of the infinite system according to

$$P_{ICY} = S^2(1-x)\,|\sin(4\pi k_{inf})| \tag{4.3}$$

with $k_{inf} = 0.3225$ is the value of propagation vector calculated in the infinite lattice as given in Sec. 2.3. Thus P_{ICY} represents the polarization in $CuCr_{1-x}Ga_xO_2$ assuming that magnetic dilution doesn't perturb the ICY state. However, we can clearly see that $P_{[110]}$ decreases linearly with x but it is well below P_{ICY} when $x \neq 0$. This reflects the fact that magnetic dilution destabilizes the ICY state of $CuCrO_2$ as previously seen.

Not only a decrease in the polarization is obtained, but also a decrease in the temperature at which ferroelectricity starts to emerge. Such temperature is directly related to the spiral plane ordering temperature T^*. Thus to confirm the values of T^* extracted from χ_κ, we calculate the electric susceptibility χ_e — the derivative of $P_{[110]}$ with respect to an applied electric field — through the following relation

$$\chi_e = \left(\frac{\partial P_{[110]}}{\partial E}\right)_{E=0} = \frac{\langle P^2_{[110]}\rangle_T - \langle P_{[110]}\rangle^2_T}{N_x k_B T^2} \tag{4.4}$$

where N_x is the number of magnetic bonds counted along the [110] direction. The thermal variation of χ_e for each $x \leq 0.2$, given in Fig. 4.14, shows a clear peak at $T = T^*$ extracted from χ_κ. This validates the value of the spiral plane ordering temperature T^* which is comparable

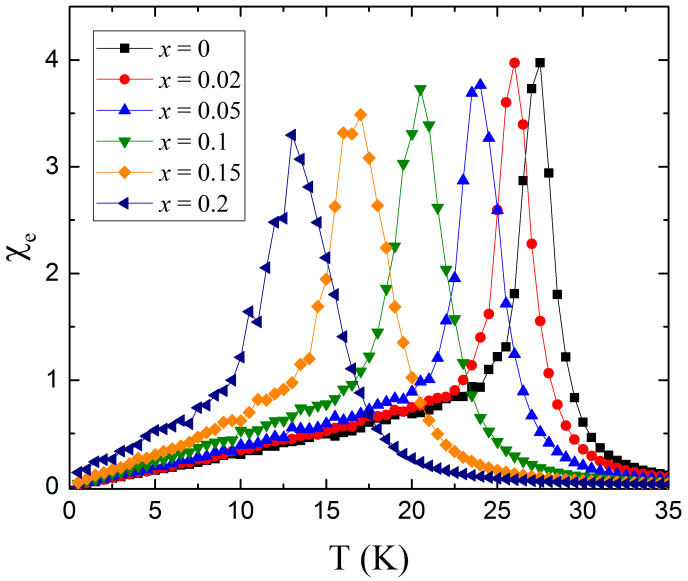

FIG. 4.14. Thermal variation of the electric susceptibility simulated with the set of $d = 0.003$ for various x in $CuCr_{1-x}Ga_xO_2$.

to T_N extracted from the C-curves for small fractions ($x \leq 0.02$) while it diverges from it for larger fractions. To characterize more precisely the ferroelectric nature in $CuCr_{1-x}Ga_xO_2$, we simulated the P-E hysteresis loops at $T = 5$ K for the various fractions of Ga^{3+} using the time step quantified MC method with the Metropolis algorithm for $R = 0.09$ given in Fig. 4.15. It can be seen that the saturation polarization decreases in the system as x increases which is normal due to the decrease in the number of magnetic bonds counted along the [110] direction and the induced disorder. Also, we can say that $CuCr_{1-x}Ga_xO_2$ for $x \leq 0.3$ still possesses ferroelectric

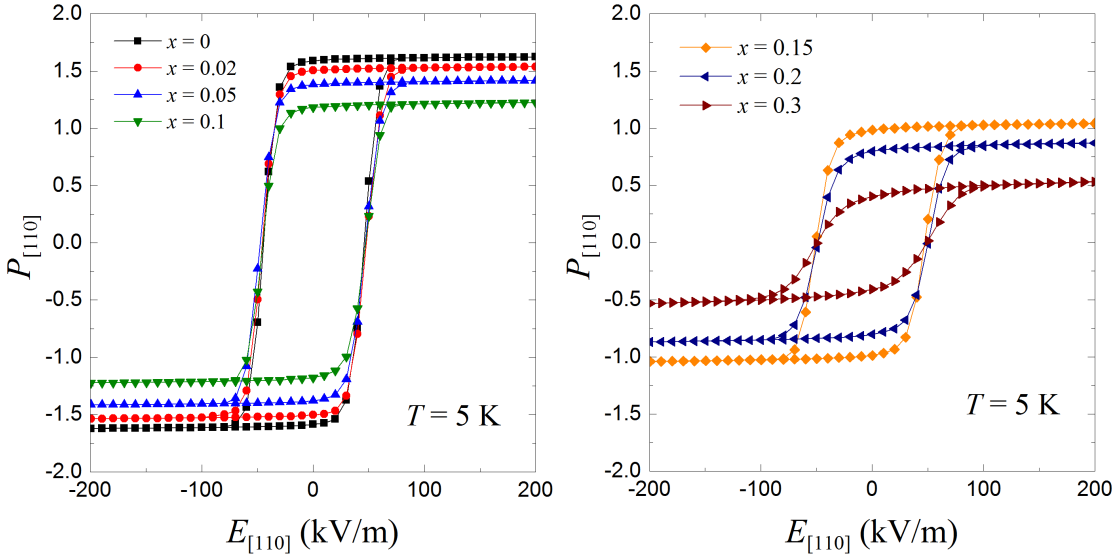

FIG. 4.15. P-E hysteresis loops simulated with the set of $d = 0.003$ along the [100] direction at $T = 5$ K for various fractions x in $CuCr_{1-x}Ga_xO_2$.

properties even when it loses its magnetic properties.

4.2 Study under a small applied magnetic field

In order to know the magnetic nature of each composition of $CuCr_{1-x}Ga_xO_2$ we investigate its magnetic properties under a small applied magnetic field. We start these sets of simulations from random spin configurations at $T_i = 300$ K and then we cool down to $T_f = 2$ K with a constant temperature step $\Delta T = 2$ K. At each temperature we perform $n_{MCS} = 1.05 \times 10^5$ MCS with discarding $n_0 = 5 \times 10^3$ MCS for thermal equilibration. The results are averaged over 112 different simulations with different random number sequences. The simulation parameters are given in Table 4.2. Magnetic properties under 0.3 T applied along the [110] directions were simulated between 300 K and 2 K to measure the magnetization per spin for each composition of $CuCr_{1-x}Ga_xO_2$ and to estimate their Curie-Weiss temperatures θ_{CW}. Fig. 4.16 shows the thermal variation of the magnetization per spin simulated for each fraction x. It can be seen that the high temperature region of M for all fractions do well obey the Curie-Weiss law and doesn't show significant x dependence, while the low temperature part does well depend on x

TABLE 4.2. MC simulation parameters used in the study of the magnetic properties of $CuCr_{1-x}Ga_xO_2$ under 0.3 T magnetic field.

Simulation parameters								
Size	N $(x = 0)$	T_i (K)	ΔT (K)	T_f (K)	n_{Temp}	n_{conf}	n_{MCS}	n_0
90×90	8 100	300	2	2	150	112	1.05×10^5	5×10^3

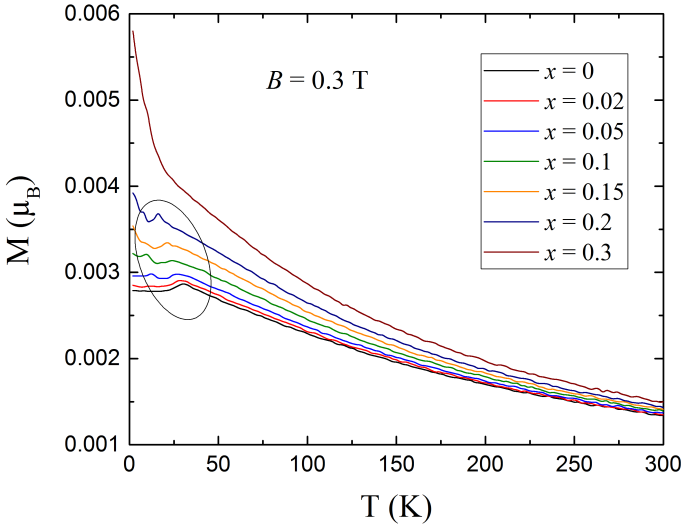

FIG. 4.16. Thermal variation of the magnetization per spin simulated with the set of $d = 0.003$ under $B = 0.3$ T magnetic field for various fractions x in $CuCr_{1-x}Ga_xO_2$.

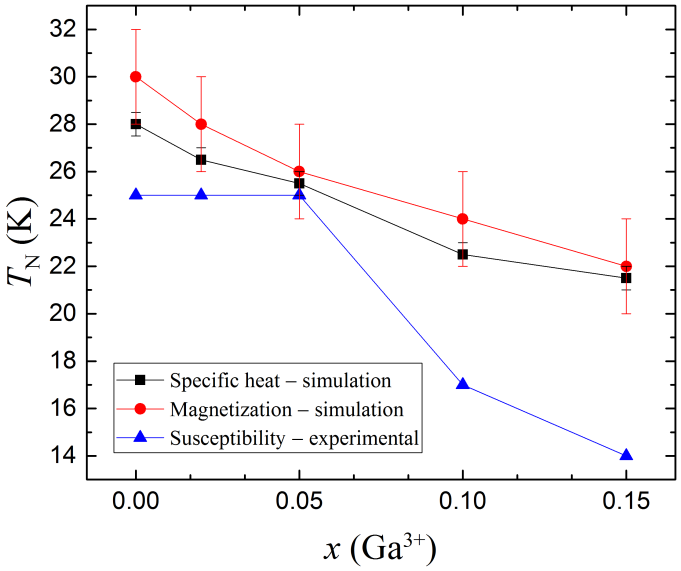

FIG. 4.17. Variation of the Néel temperature extracted from the simulated magnetization and specific heat curves from experimental magnetic susceptibility measurements as function of $x \leq 0.15$ in $CuCr_{1-x}Ga_xO_2$.

and more perturbed by statistical fluctuations. For $x \leq 0.15$, the magnetization curves possess a cusp consistent with the peak seen at the specifc heat curves as shown in Fig. 4.17. Below these cusps, M slightly decreases with temperature. This suggests that $CuCr_{1-x}Ga_xO_2$ still undergoes a phase transition to an antiferromagnetic state which is in agreement with the presence of long range order for $x \leq 0.15$ (Fig 4.5). Particularly for $x = 0.15$, we can say that the system undergoes a phase transition to an antiferromagnetic state before the spiral plane ordering takes place ($T^* < T_N$ Fig. 4.11). Our observations for $x \leq 0.15$ are consistent with the experimental results [98] in terms of the decrease of T_N as x increases without losing the antiferromagnetic nature of the system (Fig. 4.17). At $x = 0.2$, the small kink seen in the low temperature part of the M curve doesn't suggest any kind of a phase transition (but rather a statistical fluctuation) because its corresponding specific heat peak is broadened and doesn't respond to the size variation and that the long range order is lost at this fraction (Fig 4.5). For $x = 0.3$, the magnetization continuously increases under the effect of B as T decreases and doesn't show any cusp as the other compositions which confirms that a phase transition to an antiferromagnetic state does no more exist at this fraction. Such observation beside what is seen previously in terms of the loss in the long range ordering (disordered state), frustration and the quite linear behavior of the low temperature part of the specific heat curve (Fig. 4.8f) suggests that $CuCr_{0.7}Ga_{0.3}O_2$ possesses a spin-glass-like behavior.

The $1/\chi$ plots of $CuCr_{1-x}Ga_xO_2$ for the various fractions x are shown in Fig. 4.18. It can be seen that the $1/\chi$ curves for all compositions do well obey the Curie-Weiss law at high

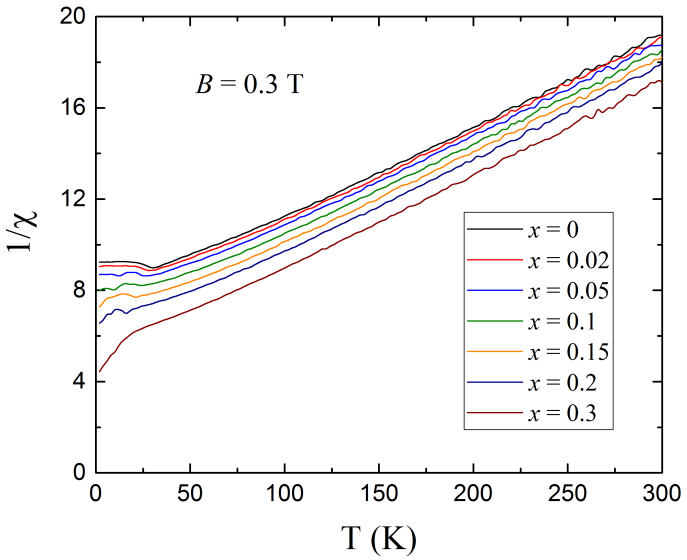

FIG. 4.18. Thermal variation of the inverse susceptibility per spin simulated with the set of $d = 0.003$ under $B = 0.3$ T magnetic field for various fractions x in $CuCr_{1-x}Ga_xO_2$.

temperatures. The extracted characteristic properties of the systems are shown in Fig. 4.19. We find that the Curie constant C per atom linearly decreases with increasing x (left panel of Fig. 4.19) which is comparable to the theoretical calculations of C. Such decrease is expected due to the decrease in the number of magnetic atoms per unit volume in the compositions. The theoretical expression of the Curie constant per atom is given as

$$C_{theo} = (1 - x)\left(\frac{3\mu_0\mu_B^2}{k_B}\right) \tag{4.5}$$

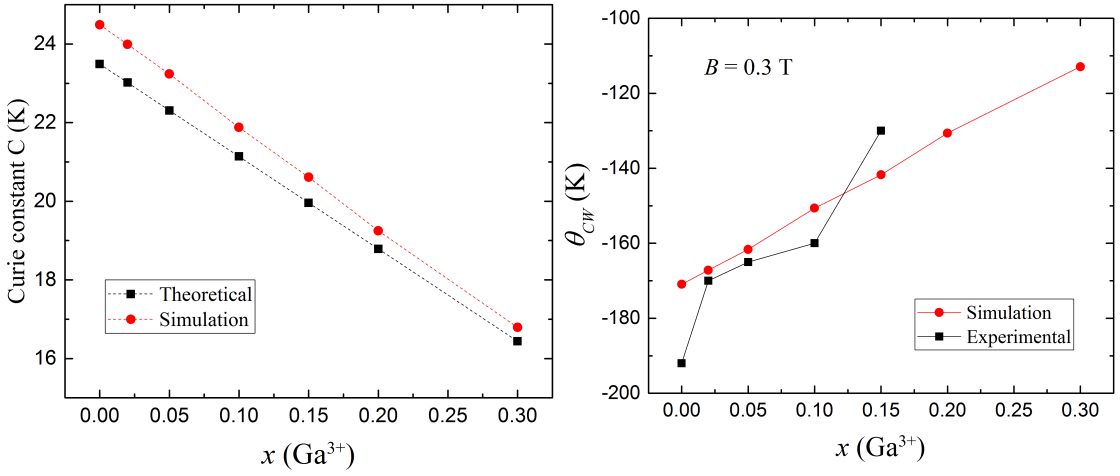

FIG. 4.19. Variation of the simulated Curie constant compared to the theoretical one (left) and the simulated Curie-Weiss temperature in comparison with the experimental one (right) as function of x in $CuCr_{1-x}Ga_xO_2$.

On the other hand, the extrapolation of the high temperature parts of the $1/\chi$ curves gives us the Curie-Weiss temperature θ_{CW} of each composition. It can be seen that θ_{CW} increases with the increase of x in the system due to the effect of magnetic dilution which is comparable to the experimental ones [98] as shown in the right panel of Fig. 4.19.

4.3 Magnetic history in $CuCr_{1-x}Ga_xO_2$: d.c. *ZFC−FC* measurements

In this part of the work we investigate the magnetic history dependence for the various fractions of Ga^{3+} in $CuCr_{1-x}Ga_xO_2$. As usual, we start our simulations from random spin configurations at $T_i = 35.01$ K. The system is then cooled down to $T_f = 0.01$ K with a constant temperature step $\Delta T = 1$ K. Now at $T = T_f$, we apply a magnetic field $B = 100$ Oe and we then start heating the system with a constant temperature step $\Delta T = 0.5$ K to reach $T = 35.01$ K. During the heating process, the *ZFC* magnetic measurements are collected. Now at $T = 35.01$ K, we start cooling the system again to $T = T_f$ with the same temperature step and under the same magnetic field. During the cooling process, the *FC* magnetic measurements are collected. The simulation parameters are given in Table 4.3. Note that during the first cooling where we don't make any magnetic measurements, we just use $n_{MCS} = 2.5 \times 10^4$ MCS with discarding $n_0 = 5 \times 10^3$ MCS for thermal equilibration.

It can be seen that the magnetization is reversible for $x \leq 0.05$ and thus it doesn't depend on the magnetic history of the system as shown in Fig. 4.20. This is because the system is long range ordered at these fractions as proved by the correlation functions given in Fig. 4.5. Also we previously said that the system preserves its antiferromagnetic nature up to $x = 0.15$. Then for $x = 0.1$ and $x = 0.15$, the long range magnetic ordering persists in the system with a small decrease from that of $x \leq 0.05$. This small decrease comes from the presence of some disorder in the system introduced by the defects.

TABLE 4.3. MC simulation parameters used in the *ZFC-FC* study of the magnetic history dependence in $CuCr_{1-x}Ga_xO_2$ studied under $B = 100$ Oe magnetic field.

Simulation parameters								
Size	$N\ (x=0)$	T_i (K)	ΔT (K)	T_f (K)	n_{Temp}	n_{conf}	n_{MCS}	n_0
90×90	8 100	35.01	0.5	0.01	141	280	8.05×10^5	5×10^3

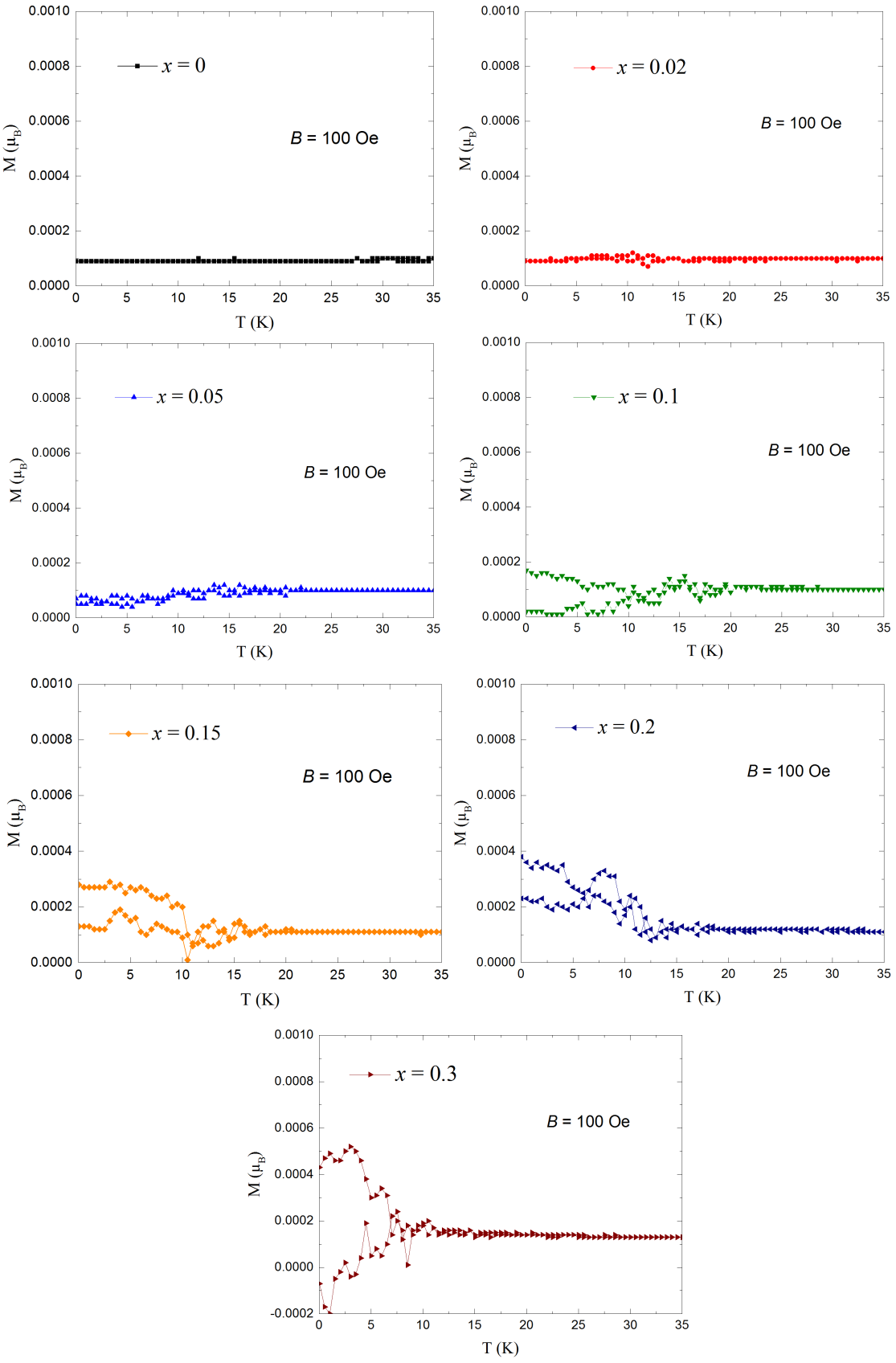

FIG. 4.20. d.c. *ZFC-FC* magnetization temperature dependence simulated under $B = 100$ Oe for each fraction x of Ga^{3+} in $CuCr_{1-x}Ga_xO_2$.

Such disorder increases the number of metastable states at low temperatures resulting in the irreversibility of the *ZFC-FC* magnetization measurements below T^* and thus a small magnetic history dependence exists as shown in Fig. 4.20. For $x = 0.2$, it is well known that the system is disordered (loss of long range ordering) and therefore the magnetic history dependence of the magnetization measurements seen in Fig. 4.20 is expected. However for $x = 0.3$, we have seen many features that suggest the presence of a spin-glass-like behavior in the system (frustration, disorder, loss of long range ordering, broadening of the specific heat peak, linear behavior of the low temperature part of the specific heat curve...). In addition, we can see a severe magnetic history dependence of the magnetization where the *ZFC* magnetization starts near zero and increases under the *FC* process. The temperature where the irreversibility takes place may give us an idea about the freezing temperature of the system which is around $T_{SG} \approx 7.5$ K. Further investigations such as the a.c. *ZFC-FC* meaurements are necessary to characterize well the freezing temperature of $CuCr_{0.7}Ga_{0.3}O_2$.

At the end of this work, we can say that if one aims to benefit from the good performance of the diluted semiconductor $CuCr_{1-x}Ga_xO_2$ with preserving its magnetic and ferroelectric properties, Ga^{3+} fraction should not exceed 0.15 otherwise the system is turned to become disordered with the possibilty of the appearance of a spin-glass-like behavior at higher fractions of Ga^{3+}.

Conclusions and perspectives

The aim of this thesis was to study the magnetoelectric properties of the multiferroic $CuCrO_2$ and the diluted $CuCr_{1-x}Ga_xO_2$ ($0 \leq x \leq 0.3$) by means of Monte Carlo simulations. By means of *ab initio* calculations*, we have estimated complete sets of exchange interactions and single ion anisotropy constants in the non-distorted and distorted crystal structures of $CuCrO_2$. We found that lattice distortion is the responsible of the incommensurate spin configuration and that it induces a weak in-plane hard-axis anisotropy along the distorted direction. We confirm that the $CuCrO_2$ has an incommensurate spin configuration with a propagation vector $\vec{q} = (0.322, 0.322, 0)$ pointing along the $[110]$ direction in agreement with the experimental spin configuration of $\vec{q} = (0.329, 0.329, 0)$. Also we showed that $CuCrO_2$ possesses a Néel temperature $T_N \approx 28.5$ K and a Curie-Weiss temperature $|\theta_{CW}| \approx 173.92$ K which are in a very good agreement with the experimental ones. We have also simulated the spontaneous ferroelectric polarization which can be described through the extended inverse DM model. The P-E hysteresis loop simulated at $T = 5$ K has an electric coercive field $E_r = 5.3 \times 10^{-2}$ MV/m consistent with that measured experimentally. Also our simulated P-E hysteresis loops at various temperatures confirm the electric control of spin helicity as reported experimentally.

On the other hand, DFT calculations showed that magnetic dilution by Ga^{3+} cations doesn't significantly affect the exchange interactions presented in the pure $CuCrO_2$ due to the close radii of Cr^{3+} and Ga^{3+}. This allowed us to investigate the effect of pure magnetic dilution without structural deformations. We found that $CuCr_{1-x}Ga_xO_2$ ($x \leq 0.15$) still possess antiferromagnetic ordering where T_N decreases as the fraction of Ga^{3+} increases in the system, while it turns to become disordered states for $x \geq 0.2$. We also found that Ga^{3+} substitution destabilizes the ICY state presented in the pure system. The spins in $CuCr_{1-x}Ga_xO_2$ for $x \leq 0.2$ lie in a unique spiral plane while that for $x = 0.3$ go out of the spiral plane and randomly oriented in all directions. Spin-glass-like behavior was expected for $x = 0.3$ due to the loss in the

*Done by Yaroslav Kvashnin at the "Department of Physics and Astronomy, Division of Materials Theory, Uppsala University, Sweden".

long range magnetic ordering in the system, the broadening and the linear behavior of the low temperature part of the specific heat curve and the presence of the main two ingredients of spin glasses: magnetic disorder and frustration. Also severe magnetic history dependence was seen in the magnetization measurements of $x = 0.3$ below $T_{SG} \approx 7.5$ K.

Further investigations are very important to have a complete and clear picture on the magnetoelectric properties of the multiferroic $CuCrO_2$. DM and biquadratic exchange interactions can be taken into account. Also the study of the high magnetic field phase diagram of $CuCrO_2$ is very important to understand the magnetization as well as exchange interaction dependences on high magnetic fields.

Within the study of magnetic dilution, it is very important to improve the *ZFC-FC* investigations in $CuCr_{1-x}Ga_xO_2$ and to model the a.c. magnetic susceptibility to characterize the spin glass transition temperature T_{SG}. Also it is important to study the effect of magnetic dilution by Al^{3+} and compare it with that of Ga^{3+}.

On the other hand, the effect of Ni^{3+} substitution in the Cr^{3+} sites was studied experimentally. It was found that Ni^{3+} enhances both ferroelectric and ferromagnetic properties in $CuCrO_2$. So MC investigations of $CuCr_{1-x}Ni_xO_2$ with the help of DFT calculations would be very interesting to confirm experimental observations.

The subject is still open for many other MC investigations such as the effect of Mg^{2+} hole doping in the Cr^{3+} sites, Ag^{+} doping in the Cu^{+} sites ... on the magnetoelectric properties of $CuCrO_2$ with the help of DFT calculations.

APPENDIX A

DFT calculations in $CuCr_{1-x}Ga_xO_2$

These calculations were done by Y. O. Kvashnin at the "Department of Physics and Astronomy, Division of Materials Theory, Uppsala University, Sweden".

This part of the work aims to study the effect of replacing some Cr^{3+} ions by Ga^{3+} on the exchange interactions presented in $CuCr_{1-x}Ga_xO_2$ using the DFT calculations. DFT calculations were performed using full-potential linear muffin-tin orbital (FP-LMTO) method as implemented in RSPt [121] software. The computational details are the same as those presented in Sec. 3.1.1. The Hubbard-U correction was applied on Cr $3d$ states. The U and J_H values were set to 2.3 and 0.96 eV, respectively. The FLL double-counting correction has been adopted. We construct a $3 \times 3 \times 1$ super-cell of $CuCrO_2$, which accommodates 9 formula units. Having 9 Cr atoms, we substitute one, two or three Cr atoms by Ga ones, which corresponds to the following dopant fractions: $x = 1/9, x = 2/9, x = 1/3$. Replacing some Cr sites with non-magnetic elements can affect the magnetic properties in two ways. First, it can cause a renormalization of the remaining Cr-Cr exchange couplings. Second, if the impurity ion has different effective radius compared to the host one, it can also distort the lattice, thus changing the positions of oxygen atoms. The latter can influence the crystal field splitting and other electronic structural properties of the adjacent Cr ions. In order to be able to disentangle the two mentioned contributions, we have considered two crystal structures:

1. Experimental crystal structure is taken from Ref. [111]. Here we just substitute certain Cr atoms with Ga ones. The effect of the lattice relaxation is not taken into account.

2. Here we make a full ionic and lattice relaxation of the undoped $CuCrO_2$ structure. For this purpose, we use another DFT code (VASP) and adopt a GGA functional, which usually

provides lattice constant values closer to experimental ones. Then, within the relaxed structure, we substitute one Cr atom by a Ga one (corresponding to $x = 1/9$) and relax the structure again. Note that experimental lattice constants might not correspond to the equilibrium structure within DFT calculations and thus it can contain forces acting on the atoms. Thus, in order to properly simulate the structural changes due to doping, one first needs to relax the structure of the parent compound.

To calculate the new values of the exchange interactions, we consider the Hamiltonian of Eq. 3.1 in a FM state. For simplicity we make our calculations in the non-distorted crystal structure. As a first step, we start with the first approach of the un-relaxed experimental crystal structure. The considered structural models are shown in Fig. A.1. The minimal concentration $x = 1/9$ is represented by a single configuration (I). For higher fractions, we construct several inequivalent models to simulate possible distributions of the impurity sites. For all considered configurations, the magnetic moments of Cr were close (within $0.02\ \mu_B$/Cr) to the value obtained for an undoped system, which was about $2.62\ \mu_B$/Cr. The calculated mean values of J_{ij}'s as well as the mean deviations for various Ga fractions are given in Table A.1. It can be seen that the mean values of J_2, J_3 and J_4 interactions are relatively more affected by the doping as compared to that of J_1. This is because the superexchange paths between Cr ions are not affected by Ga doping. Ga-doped system seems to remain insulating and thus there are no other mechanisms (e.g.

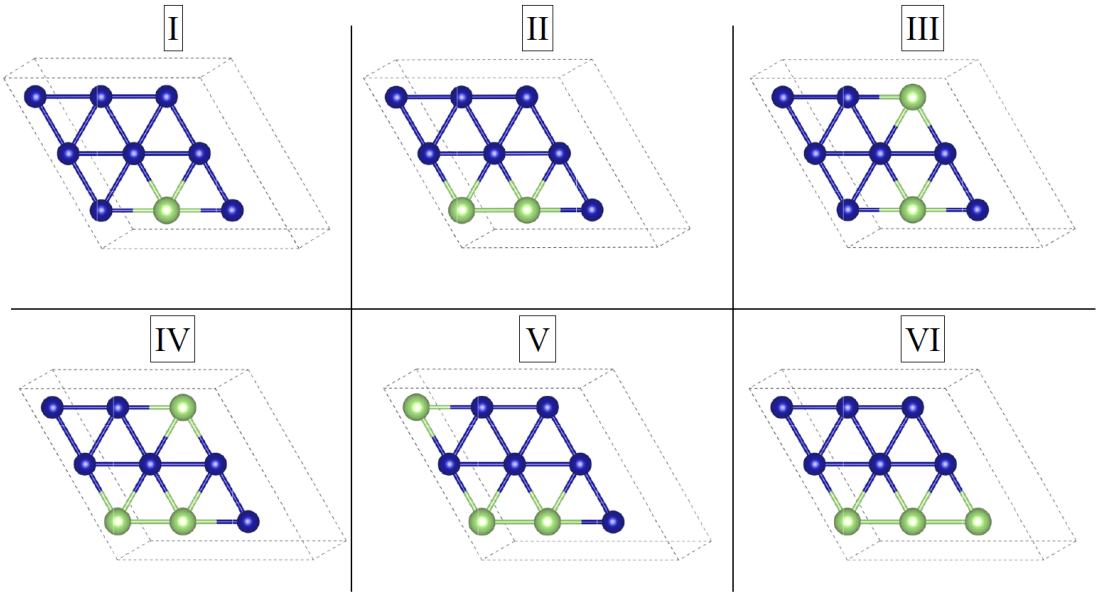

FIG. A.1. Considered structural configurations. Cr (Ga) atoms are represented by blue (green) spheres. Configuration I corresponds to $x = 1/9$; II, III correspond to $x = 2/9$; and IV,V,VI correspond to $x = 1/3$.

TABLE A.1. Statistical averages ($\langle J_{ij} \rangle$) and standard deviations from the mean (σ) of the exchange interactions for various considered configurations in $\mathrm{CuCr_{1-x}Ga_xO_2}$. The values are given in meV.

Configuration	$\langle J_1 \rangle \pm \sigma_1$	$\langle J_2 \rangle \pm \sigma_2$	$\langle J_3 \rangle \pm \sigma_3$	$\langle J_4 \rangle \pm \sigma_4$
I ($x = 1/9$)	-2.708 ± 0.052	-0.007 ± 0.169	-0.340 ± 0.054	-0.068 ± 0.005
II ($x = 2/9$)	-2.680 ± 0.078	-0.204 ± 0.246	-0.354 ± 0.068	-0.054 ± 0.009
III ($x = 2/9$)	-2.708 ± 0.272	-0.245 ± 0.185	-0.367 ± 0.068	-0.054 ± 0.009
IV ($x = 1/3$)	-2.653 ± 0.059	-0.367 ± 0.273	-0.381 ± 0.054	-0.054 ± 0.014
V ($x = 1/3$)	-2.599 ± 0.078	-0.259 ± 0.182	-0.367 ± 0.054	-0.054 ± 0.011
VI ($x = 1/3$)	-2.694 ± 0.083	-0.286 ± 0.411	-0.408 ± 0.054	-0.041 ± 0.012

RKKY), which might have potential contributions. And because the most dominant exchange interaction in the system is J_1 and the others are very small compared to it, we will neglect these small fluctuations around the mean values of J_{ij}'s in our MC simulations. It is important to note that these calculations were repeated for the relaxed crystal structure where we found roughly the same results with no pronounced effects of the Ga ions on the exchange interactions of $\mathrm{CuCr_{1-x}Ga_xO_2}$ (the results are not shown here).

Bibliography

[1] M. A. Ruderman and C. Kittel. Indirect exchange coupling of nuclear magnetic moments by conduction electrons. *Phys. Rev.*, 96:99–102, Oct 1954. doi: 10.1103/PhysRev.96.99. URL https://link.aps.org/doi/10.1103/PhysRev.96.99.

[2] T. Kasuya. A theory of metallic ferro- and antiferromagnetism on zener's model. *Progress of Theoretical Physics*, 16(1):45, 1956. doi: 10.1143/PTP.16.45. URL http://dx.doi.org/10.1143/PTP.16.45.

[3] K. Yosida. Magnetic properties of cu-mn alloys. *Phys. Rev.*, 106:893–898, Jun 1957. doi: 10.1103/PhysRev.106.893. URL https://link.aps.org/doi/10.1103/PhysRev.106.893.

[4] P. W. Anderson. Antiferromagnetism. theory of superexchange interaction. *Phys. Rev.*, 79: 350–356, Jul 1950. doi: 10.1103/PhysRev.79.350. URL https://link.aps.org/doi/10.1103/PhysRev.79.350.

[5] A. Crépieux and C. Lacroix. Dzyaloshinsky–moriya interactions induced by symmetry breaking at a surface. *Journal of Magnetism and Magnetic Materials*, 182(3): 341 – 349, 1998. ISSN 0304-8853. doi: http://dx.doi.org/10.1016/S0304-8853(97)01044-5. URL http://www.sciencedirect.com/science/article/pii/S0304885397010445.

[6] H. A. Kramers. L'interaction entre les atomes magnétogènes dans un cristal paramagnétique. *Physica*, 1(1):182 – 192, 1934. ISSN 0031-8914. doi: http://dx.doi.org/10.1016/S0031-8914(34)90023-9. URL http://www.sciencedirect.com/science/article/pii/S0031891434900239.

[7] P. W. Anderson. New approach to the theory of superexchange interactions. *Phys. Rev.*, 115:2–13, Jul 1959. doi: 10.1103/PhysRev.115.2. URL https://link.aps.org/doi/10.1103/PhysRev.115.2.

[8] G. H. O. Daalderop, P. J. Kelly, and M. F. H. Schuurmans. Magnetocrystalline anisotropy and orbital moments in transition-metal compounds. *Phys. Rev. B*, 44:12054–12057, Dec 1991. doi: 10.1103/PhysRevB.44.12054. URL http://link.aps.org/doi/10.1103/PhysRevB.44.12054.

[9] C. Kittel. Physical theory of ferromagnetic domains. *Rev. Mod. Phys.*, 21:541–583, Oct 1949. doi: 10.1103/RevModPhys.21.541. URL https://link.aps.org/doi/10.1103/RevModPhys.21.541.

[10] M. Yun and G. S. Jeon. Classical heisenberg antiferromagnet on a triangular lattice in the presence of single-ion anisotropy. *J. Phys.: Conf. Ser.*, 592:012111, 2015. doi: 10.1088/1742-6596/592/1/012111. URL http://iopscience.iop.org/article/10.1088/1742-6596/592/1/012111/pdf.

[11] A. Herpin. *Théorie du magnétisme*. Bibliothèque des Sciences et Techniques Nucléaires. Institut national des sciences et techniques nucléaires, 1968. URL https://books.google.fr/books?id=L8vvAAAAMAAJ.

[12] M. Soda, K. Kimura, T. Kimura, M. Matsuura, and K. Hirota. Electric control of spin helicity in multiferroic triangular lattice antiferromagnet $CuCrO_2$ with proper-screw order. *Journal of the Physical Society of Japan*, 78(12):124703, 2009. doi: 10.1143/JPSJ.78.124703. URL http://dx.doi.org/10.1143/JPSJ.78.124703.

[13] M. Soda, K. Kimura, T. Kimura, and K. Hirota. Domain rearrangement and spin-spiral-plane flop as sources of magnetoelectric effects in delafossite $CuCrO_2$. *Phys. Rev. B*, 81:100406, Mar 2010. doi: 10.1103/PhysRevB.81.100406. URL http://link.aps.org/doi/10.1103/PhysRevB.81.100406.

[14] M. Frontzek, G. Ehlers, A. Podlesnyak, H. Cao, M. Matsuda, O. Zaharko, N. Aliouane, S. Barilo, and S. V. Shiryaev. Magnetic structure of $CuCrO_2$: a single crystal neutron diffraction study. *Journal of Physics: Condensed Matter*, 24(1):016004, 2012. doi: 10.1088/0953-8984/24/1/016004. URL http://stacks.iop.org/0953-8984/24/i=1/a=016004.

[15] M. Poienar, F. Damay, C. Martin, V. Hardy, A. Maignan, and G. André. Structural and magnetic properties of $CuCr_{1-x}Mg_xO_2$ by neutron powder diffraction. *Phys. Rev. B*, 79:014412, Jan 2009. doi: 10.1103/PhysRevB.79.014412. URL http://link.aps.org/doi/10.1103/PhysRevB.79.014412.

[16] M. Poienar, F. Damay, C. Martin, J. Robert, and S. Petit. Spin dynamics in the geometrically frustrated multiferroic $CuCrO_2$. *Phys. Rev. B*, 81:104411, Mar 2010. doi: 10.1103/PhysRevB.81.104411. URL http://link.aps.org/doi/10.1103/PhysRevB.81.104411.

[17] J. E. Greedan. Geometrically frustrated magnetic materials. *J. Mater. Chem.*, 11:37–53, 2001. doi: 10.1039/B003682J. URL http://dx.doi.org/10.1039/B003682J.

[18] A. P. Ramirez. Strongly geometrically frustrated magnets. *Annual Review of Materials Science*, 24:453–480, 1994. doi: 10.1146/annurev.ms.24.080194.002321. URL https://doi.org/10.1146/annurev.ms.24.080194.002321.

[19] J. S. Smart. *Effective Field Theories of Magnetism*. Studies in Physics and Chemistry. Philadelphia: W. B. Saunders, 1966. URL http://www.worldcat.org/title/effective-field-theories-of-magnetism/oclc/474196598?referer=di&ht=edition.

[20] J.M.D. Coey. *Magnetism and Magnetic Materials*. EngineeringPro collection. Cambridge University Press, 2010. ISBN 9780521816144. URL https://books.google.fr/books?id=Ie72CFd-eSEC.

[21] V. Cannella and J. A. Mydosh. Magnetic ordering in gold-iron alloys. *Phys. Rev. B*, 6:4220–4237, Dec 1972. doi: 10.1103/PhysRevB.6.4220. URL https://link.aps.org/doi/10.1103/PhysRevB.6.4220.

[22] K. Binder and A. P. Young. Spin glasses: Experimental facts, theoretical concepts, and open questions. *Rev. Mod. Phys.*, 58:801–976, Oct 1986. doi: 10.1103/RevModPhys.58.801. URL https://link.aps.org/doi/10.1103/RevModPhys.58.801.

[23] H. Maletta and W. Zinn. Chapter 84 spin glasses. *Handbook on the Physics and Chemistry of Rare Earths*, 12:213 – 356, 1989. ISSN 0168-1273. doi: http://dx.doi.org/10.1016/S0168-1273(89)12008-X. URL http://www.sciencedirect.com/science/article/pii/S016812738912008X.

[24] Y. Tokura and S. Seki. Multiferroics with spiral spin orders. *Advanced Materials*, 22(14):1554–1565, 2010. ISSN 1521-4095. doi: 10.1002/adma.200901961. URL http://dx.doi.org/10.1002/adma.200901961.

[25] Y. Tokura, S. Seki, and N. Nagaosa. Multiferroics of spin origin. *Reports on Progress in Physics*, 77(7):076501, 2014. doi: 10.1088/0034-4885/77/7/076501. URL http://stacks.iop.org/0034-4885/77/i=7/a=076501.

[26] N. Terada. Spin and orbital orderings behind multiferroicity in delafossite and related compounds. *Journal of Physics: Condensed Matter*, 26(45):453202, 2014. doi: 10.1088/0953-8984/26/45/453202. URL http://stacks.iop.org/0953-8984/26/i=45/a=453202.

[27] S. W. Cheong and M. Mostovoy. Multiferroics: a magnetic twist for ferroelectricity. 6(1): 13–20, 2007. ISSN 1476-1122. doi: 10.1038/nmat1804. URL http://dx.doi.org/10.1038/nmat1804.

[28] T. Arima. Spin-driven ferroelectricity and magneto-electric effects in frustrated magnetic systems. *Journal of the Physical Society of Japan*, 80(5):052001, 2011. doi: 10.1143/JPSJ.80.052001. URL http://dx.doi.org/10.1143/JPSJ.80.052001.

[29] M. Fiebig, T. Lottermoser, D. Meier, and M. Trassin. The evolution of multiferroics. 1: 16046, 2016. doi: doi:10.1038/natrevmats.2016.46. URL http://dx.doi.org/10.1038/natrevmats.2016.46.

[30] D. Khomskii. Classifying multiferroics: Mechanisms and effects. *Physics*, 2(20), March 2009. doi: 10.1103/Physics.2.20. URL http://link.aps.org/doi/10.1103/Physics.2.20.

[31] T. Kimura, T. Goto, H. Shintani, K. Ishizaka, T. Arima, and Y. Tokura. Magnetic control of ferroelectric polarization. 426(6962):55–58, 2003. ISSN 0028-0836. doi: 10.1038/nature02018. URL http://dx.doi.org/10.1038/nature02018.

[32] J. Wang, J. B. Neaton, H. Zheng, V. Nagarajan, S. B. Ogale, B. Liu, D. Viehland, V. Vaithyanathan, D. G. Schlom, U. V. Waghmare, N. A. Spaldin, K. M. Rabe, M. Wuttig, and R. Ramesh. Epitaxial $BiFeO_3$ multiferroic thin film heterostructures. *Science*, 299(5613):1719–1722, 2003. ISSN 0036-8075. doi: 10.1126/science.1080615. URL http://science.sciencemag.org/content/299/5613/1719.

[33] H. Schmid, H. Rieder, and E. Ascher. Magnetic susceptibilities of some 3d transition metal boracites. *Solid State Communications*, 3(10):327 – 330, 1965. ISSN 0038-1098. doi: http://dx.doi.org/10.1016/0038-1098(65)90088-8. URL http://www.sciencedirect.com/science/article/pii/0038109865900888.

[34] E. Ascher, H. Rieder, H. Schmid, and H. Stössel. Some properties of ferromagnetoelectric nickel-iodine boracite, $Ni_3B_7O_{13}I$. *Journal of Applied Physics*, 37(3):1404–1405, 1966. doi: 10.1063/1.1708493. URL http://dx.doi.org/10.1063/1.1708493.

[35] G. A. Smolenskii and I. E. Chupis. Ferroelectromagnets. *Soviet Physics Uspekhi*, 25(7): 475, 1982. doi: 10.1070/PU1982v025n07ABEH004570. URL http://stacks.iop.org/0038-5670/25/i=7/a=R02.

[36] H. Schmid. Multi-ferroic magnetoelectrics. *Ferroelectrics*, 162(1):317–338, 1994. doi: 10.1080/00150199408245120. URL http://dx.doi.org/10.1080/00150199408245120.

[37] M. Fiebig. Revival of the magnetoelectric effect. *Journal of Physics D: Applied Physics*, 38(8):R123, 2005. doi: 10.1088/0022-3727/38/8/R01. URL http://stacks.iop.org/0022-3727/38/i=8/a=R01.

[38] J. P. Rivera. On definitions, units, measurements, tensor forms of the linear magnetoelectric effect and on a new dynamic method applied to $Cr - Cl$ boracite. *Ferroelectrics*, 161(1): 165–180, 1994. doi: 10.1080/00150199408213365. URL http://dx.doi.org/10.1080/00150199408213365.

[39] D. N. Astrov. The magnetoelectric effect in antiferromagnetics. *Sov. Phys. JETP*, 11(3):708, 1960. URL http://www.jetp.ac.ru/cgi-bin/dn/e_011_03_0708.pdf.

[40] V. J. Folen, G. T. Rado, and E. W. Stalder. Anisotropy of the magnetoelectric effect in Cr_2O_3. *Phys. Rev. Lett.*, 6:607–608, Jun 1961. doi: 10.1103/PhysRevLett.6.607. URL https://link.aps.org/doi/10.1103/PhysRevLett.6.607.

[41] H. Raebiger, S. Lany, and A. Zunger. Origins of the p-type nature and cation deficiency in Cu_2O and related materials. *Phys. Rev. B*, 76:045209, Jul 2007. doi: 10.1103/PhysRevB.76.045209. URL http://link.aps.org/doi/10.1103/PhysRevB.76.045209.

[42] C. Friedel. A combination of natural iron oxides and copper and reproduction of actamides. *Sciences Academy*, 77:211, 1873.

[43] R. D. Shannon, D. B. Rogers, and C. T. Prewitt. Chemistry of noble metal oxides. i. syntheses and properties of ABO_2 delafossite compounds. *Inorganic Chemistry*, 10(4): 713–718, 1971. doi: 10.1021/ic50098a011. URL http://dx.doi.org/10.1021/ic50098a011.

[44] R. D. Shannon, C. T. Prewitt, and D. B. Rogers. Chemistry of noble metal oxides. ii. crystal structures of platinum cobalt dioxide, palladium cobalt dioxide, coppper iron dioxide, and silver iron dioxide. *Inorganic Chemistry*, 10(4):719–723, 1971. doi: 10.1021/ic50098a012. URL http://dx.doi.org/10.1021/ic50098a012.

[45] R. D. Shannon, D. Robert, D. B. Rogers, C. T. Prewitt, and J. L. Gillson. Chemistry of noble metal oxides. iii. electrical transport properties and crystal chemistry of ABO_2 compounds with the delafossite structure. *Inorganic Chemistry*, 10(4):723–727, 1971. doi: 10.1021/ic50098a013. URL http://dx.doi.org/10.1021/ic50098a013.

[46] H. Takatsu, S. Y. Onezawa, S. M. Ouri, S. Nakatsuji, K. T. Anaka, and Y. Maeno. Roles of high-frequency optical phonons in the physical properties of the conductive delafossite $PdCoO_2$. *Journal of the Physical Society of Japan*, 76(10):104701, 2007. doi: 10.1143/JPSJ.76.104701. URL http://dx.doi.org/10.1143/JPSJ.76.104701.

[47] C. W. Hicks, A. S. Gibbs, A. P. Mackenzie, H. Takatsu, Y. Maeno, and E. A. Yelland. Quantum oscillations and high carrier mobility in the delafossite $PdCoO_2$. *Physical Review Letters*, 109(11):116401, 2012. doi: 10.1103/PhysRevLett.109.116401. URL http://dx.doi.org/10.1103/PhysRevLett.109.116401.

[48] C. W. Hicks, A. S. Gibbs, L. Zhao, P. Kushwaha, H. Borrmann, A. P. Mackenzie, H. Takatsu, S. Yonezawa, M. Maeno, and E. A. Yelland. Quantum oscillations and magnetic reconstruction in the delafossite $PdCoO_2$. *Physical Review. B, Condensed matter and materials physics*, 92(1):014425, 2015. doi: 10.1103/PhysRevB.92.014425. URL http://dx.doi.org/10.1103/PhysRevB.92.014425.

[49] P. Kushwaha, V. Sunko, P. J. W. Moll, L. Bawden, J. M. Riley, N. Nandi, H. Rosner, M. P. Schmidt, F. Arnold, E. Hassinger, T. K. Kim, M. Hoesch, A. P. Mackenzie, and P. D. C. King. Nearly-free electrons in a 5d delafossite oxide metal. *Science Advances*, 1(9):1500692, 2015. doi: 10.1126/sciadv.1500692. URL http://dx.doi.org/10.1126/sciadv.1500692.

[50] H. Kawazoe, M. Yasukawa, H. Hyodo, M. Kurita, H. Yanagi, and H. Hosono. P-type electrical conduction in transparent thin films of $CuAlO_2$. *Nature*, 389(6654):939–942, 1997. doi: 10.1038/40087. URL http://www.nature.com/nature/journal/v389/n6654/full/389939a0.html.

[51] R. Daou, R. Frésard, S. Hébert, and A. Maignan. Large anisotropic thermal conductivity of the intrinsically two-dimensional metallic oxide $PdCoO_2$. *Phys. Rev. B*, 91:041113, Jan 2015. doi: 10.1103/PhysRevB.91.041113. URL http://link.aps.org/doi/10.1103/PhysRevB.91.041113.

[52] T. Okuda, N. Jufuku, S. Hidaka, and N. Terada. Magnetic, transport, and thermoelectric properties of the delafossite oxides $CuCr_{1-x}Mg_xO_2$ $(0 \leqslant x \leqslant 0.04)$. *Phys. Rev. B*, 72:144403, Oct 2005. doi: 10.1103/PhysRevB.72.144403. URL http://link.aps.org/doi/10.1103/PhysRevB.72.144403.

[53] T. Nozaki, K. Hayashi, and T. Kajitani. Thermoelectric properties of delafossite-type oxide $CuFe_{1-x}Ni_xO_2$ $(0 \leqslant x \leqslant 0.05)$. *J. Chem. Eng. Japn.*, 40(13):1205–1209, 2007.

doi: 10.1252/jcej.07WE146.

[54] A. Maignan, V. Eyert, C. Martin, S. Kremer, R. Frésard, and D. Pelloquin. Electronic structure and thermoelectric properties of $CuRh_{1-x}Mg_xO_2$. *Phys. Rev. B*, 80:115103, Sep 2009. doi: 10.1103/PhysRevB.80.115103. URL http://link.aps.org/doi/10.1103/PhysRevB.80.115103.

[55] S. Kremer and R. Frésard. Thermoelectric transport properties of an apparent fermi liquid: Relation to an analytic anomaly in the density of states and application to hole-doped delafossites. *Annalen der Physik*, 524(1):21–36, 2012. ISSN 1521-3889. doi: 10.1002/andp.201100165. URL http://dx.doi.org/10.1002/andp.201100165.

[56] M. Mekata, N. Yaguchi, T. Takagi, S. Mitsuda, and H. Yoshizawa. Magnetic ordering in delafossite $CuFeO_2$. *Journal of Magnetism and Magnetic Materials*, 104:823 – 824, 1992. ISSN 0304-8853. doi: http://dx.doi.org/10.1016/0304-8853(92)90377-Z. URL http://www.sciencedirect.com/science/article/pii/030488539290377Z.

[57] M. Mekata, N. Yaguchi, T. Takagi, T. Sugino, S. Mitsuda, H. Yoshizawa, N. Hosoito, and T. Shinjo. Successive magnetic ordering in $CuFeO_2$ – a new type of partially disordered phase in a triangular lattice antiferromagnet. *Journal of the Physical Society of Japan*, 62 (12):4474–4487, 1993. doi: 10.1143/JPSJ.62.4474. URL http://dx.doi.org/10.1143/JPSJ.62.4474.

[58] O. A. Petrenko, G. Balakrishnan, M. R. Lees, D. McK. Paul, and A. Hoser. High-magnetic-field behavior of the triangular-lattice antiferromagnet $CuFeO_2$. *Phys. Rev. B*, 62:8983–8988, Oct 2000. doi: 10.1103/PhysRevB.62.8983. URL http://link.aps.org/doi/10.1103/PhysRevB.62.8983.

[59] T. Kimura, J. C. Lashley, and A. P. Ramirez. Inversion-symmetry breaking in the noncollinear magnetic phase of the triangular-lattice antiferromagnet $CuFeO_2$. *Phys. Rev. B*, 73:220401, Jun 2006. doi: 10.1103/PhysRevB.73.220401. URL http://link.aps.org/doi/10.1103/PhysRevB.73.220401.

[60] F. Ye, Y. Ren, Q. Huang, J. A. Fernandez-Baca, Pengcheng Dai, J. W. Lynn, and T. Kimura. Spontaneous spin-lattice coupling in the geometrically frustrated triangular lattice antiferromagnet $CuFeO_2$. *Phys. Rev. B*, 73:220404, Jun 2006. doi: 10.1103/PhysRevB.73.220404. URL http://link.aps.org/doi/10.1103/PhysRevB.73.220404.

[61] V. Eyert, R. Frésard, and A. Maignan. Long-range magnetic order and spin-lattice coupling in delafossite $CuFeO_2$. *Phys. Rev. B*, 78:052402, Aug 2008. doi: 10.1103/PhysRevB.78.052402. URL http://link.aps.org/doi/10.1103/PhysRevB.78.052402.

[62] A. Maignan, C. Martin, R. Frésard, V. Eyert, E. Guilmeau, S. Hébert, M. Poienar, and D. Pelloquin. On the strong impact of doping in the triangular antiferromagnet $CuCrO_2$. *Solid State Communications*, 149(23–24):962 – 967, 2009. ISSN 0038-1098. doi: http://dx.doi.org/10.1016/j.ssc.2009.02.026. URL http://www.sciencedirect.com/science/article/pii/S003810980900088X.

[63] J. Xue-Fan, L. Xian-Feng, W. Yin-Zhong, and H. Jiu-Rong. Exchange coupling and helical spin order in the triangular lattice antiferromagnet $CuCrO_2$ using first principles. *Chinese Physics B*, 21(7):77502, 2012. doi: 10.1088/1674-1056/21/7/077502. URL http://stacks.iop.org/1674-1056/21/i=7/a=077502.

[64] M. Frontzek, J. T. Haraldsen, A. Podlesnyak, M. Matsuda, A. D. Christianson, R. S. Fishman, A. S. Sefat, Y. Qiu, J. R. D. Copley, S. Barilo, S. V. Shiryaev, and G. Ehlers. Magnetic excitations in the geometric frustrated multiferroic $CuCrO_2$. *Phys. Rev. B*, 84:094448, Sep 2011. doi: 10.1103/PhysRevB.84.094448. URL http://link.aps.org/doi/10.1103/PhysRevB.84.094448.

[65] K. Kimura, H. Nakamura, K. Ohgushi, and T. Kimura. Magnetoelectric control of spin-chiral ferroelectric domains in a triangular lattice antiferromagnet. *Phys. Rev. B*, 78:

140401, Oct 2008. doi: 10.1103/PhysRevB.78.140401. URL http://link.aps.org/doi/10.1103/PhysRevB.78.140401.

[66] M. Poienar, V. Hardy, B. Kundys, K. Singh, A. Maignan, F. Damay, and C. Martin. Revisiting the properties of delafossite $CuCrO_2$: A single crystal study. *Journal of Solid State Chemistry*, 185:56 – 61, 2012. ISSN 0022-4596. doi: http://dx.doi.org/10.1016/j.jssc.2011.10.047. URL http://www.sciencedirect.com/science/article/pii/S0022459611005895.

[67] S. Seki, Y. Onose, and Y. Tokura. Spin-driven ferroelectricity in triangular lattice antiferromagnets $ACrO_2$ ($A = Cu,\ Ag,\ Li$ or Na). *Phys. Rev. Lett.*, 101:067204, Aug 2008. doi: 10.1103/PhysRevLett.101.067204. URL http://link.aps.org/doi/10.1103/PhysRevLett.101.067204.

[68] O. Aktas, G. Quirion, T. Otani, and T. Kimura. First-order ferroelastic transition in a magnetoelectric multiferroic: $CuCrO_2$. *Phys. Rev. B*, 88:224104, Dec 2013. doi: 10.1103/PhysRevB.88.224104. URL http://link.aps.org/doi/10.1103/PhysRevB.88.224104.

[69] X. L. Wang, J. Horvat, H. K. Liu, J. N. Li, and S. X. Dou. Anomalous magnetization peak effect in spiral-grown $Bi_2Sr_2CaCu_2O_y$ crystals. *Phys. Rev. B*, 55:R3402–R3405, Feb 1997. doi: 10.1103/PhysRevB.55.R3402. URL https://link.aps.org/doi/10.1103/PhysRevB.55.R3402.

[70] V. N. Timofeev and I. G. Gorlova. Growth defects in {BSCCO} (2212) single crystal whiskers. *Physica C: Superconductivity*, 309(1–2):113 – 119, 1998. ISSN 0921-4534. doi: http://dx.doi.org/10.1016/S0921-4534(98)00562-0. URL http://www.sciencedirect.com/science/article/pii/S0921453498005620.

[71] M. Oussena, P. A. J. de Groot, S. J. Porter, R. Gagnon, and L. Taillefer. Vortex channeling along twin planes in $YBa_2Cu_3O_{7-x}$. *Phys. Rev. B*, 51:1389–1392, Jan 1995. doi: 10.1103/PhysRevB.51.1389. URL https://link.aps.org/doi/10.1103/PhysRevB.51.1389.

[72] I. Monot-Laffez, M. Dominiczak, F. Giovannelli, A. Ruyter, M. D. Rossell, and G. V. Tendeloo. Correlation between structural defects and properties in large {La-Sr-Mn-O} single crystals. *Journal of Applied Physics*, 101(5):053502, 2007. doi: 10.1063/1.2710439. URL http://dx.doi.org/10.1063/1.2710439.

[73] H. Kadowaki, H. Kikuchi, and Y. Ajiro. Neutron powder diffraction study of the two-dimensional triangular lattice antiferromagnet $CuCrO_2$. *Journal of Physics: Condensed Matter*, 2(19):4485, 1990. doi: 10.1088/0953-8984/2/19/014. URL http://stacks.iop.org/0953-8984/2/i=19/a=014.

[74] K. Kimura, T. Otani, H. Nakamura, Y. Wakabayashi, and T. Kimura. Lattice distortion coupled with magnetic ordering in a triangular lattice antiferromagnet $CuCrO_2$. *Journal of the Physical Society of Japan*, 78(11):113710, 2009. doi: 10.1143/JPSJ.78.113710. URL http://dx.doi.org/10.1143/JPSJ.78.113710.

[75] H. Kadowaki, H. Takei, and K. Motoya. Double-Q 120 degrees structure in the heisenberg antiferromagnet on rhombohedrally stacked triangular lattice $LiCrO_2$. *Journal of Physics: Condensed Matter*, 7(34):6869, 1995. doi: 10.1088/0953-8984/7/34/011. URL http://stacks.iop.org/0953-8984/7/i=34/a=011.

[76] E. Rastelli and A. Tassi. The rhombohedral heisenberg antiferromagnet: infinite degeneracy of the ground state and magnetic properties of solid oxygen. *Journal of Physics C: Solid State Physics*, 19(19):L423, 1986. doi: 10.1088/0022-3719/19/19/006. URL http://stacks.iop.org/0022-3719/19/i=19/a=006.

[77] P. Curie. Sur la symétrie dans les phénomènes physiques, symétrie d'un champ électrique et d'un champ magnétique. *J. Phys. Theor. Appl.*, 3(1):393–415, 1894. doi: 10.1051/jphystap:018940030039300. URL https://doi.org/10.1051/jphystap:

018940030039300.

[78] I.E. Dzyaloshinskii. On the magneto-electrical effect in antiferromagnets. *J. Exptl. Theoret. Phys.*, 37(3):881–882, 1959. URL http://www.jetp.ac.ru/cgi-bin/e/index/e/10/3/p628?a=list.

[79] M. Mostovoy. Ferroelectricity in spiral magnets. *Phys. Rev. Lett.*, 96:067601, Feb 2006. doi: 10.1103/PhysRevLett.96.067601. URL https://link.aps.org/doi/10.1103/PhysRevLett.96.067601.

[80] H. Katsura, N. Nagaosa, and A. V. Balatsky. Spin current and magnetoelectric effect in noncollinear magnets. *Phys. Rev. Lett.*, 95:057205, Jul 2005. doi: 10.1103/PhysRevLett.95.057205. URL https://link.aps.org/doi/10.1103/PhysRevLett.95.057205.

[81] I. A. Sergienko and E. Dagotto. Role of the dzyaloshinskii-moriya interaction in multiferroic perovskites. *Phys. Rev. B*, 73:094434, Mar 2006. doi: 10.1103/PhysRevB.73.094434. URL https://link.aps.org/doi/10.1103/PhysRevB.73.094434.

[82] C. Jia, S. Onoda, N. Nagaosa, and J. H. Han. Bond electronic polarization induced by spin. *Phys. Rev. B*, 74:224444, Dec 2006. doi: 10.1103/PhysRevB.74.224444. URL https://link.aps.org/doi/10.1103/PhysRevB.74.224444.

[83] C. Jia, S. Onoda, N. Nagaosa, and J. H. Han. Microscopic theory of spin-polarization coupling in multiferroic transition metal oxides. *Phys. Rev. B*, 76:144424, Oct 2007. doi: 10.1103/PhysRevB.76.144424. URL https://link.aps.org/doi/10.1103/PhysRevB.76.144424.

[84] T. Arima. Ferroelectricity induced by proper-screw type magnetic order. *Journal of the Physical Society of Japan*, 76(7):073702, 2007. doi: 10.1143/JPSJ.76.073702. URL http://dx.doi.org/10.1143/JPSJ.76.073702.

[85] T. A. Kaplan and S. D. Mahanti. Canted-spin-caused electric dipoles: A local symmetry theory. *Phys. Rev. B*, 83:174432, May 2011. doi: 10.1103/PhysRevB.83.174432. URL https://link.aps.org/doi/10.1103/PhysRevB.83.174432.

[86] N. Aliouane, K. Schmalzl, D. Senff, A. Maljuk, K. Prokeš, M. Braden, and D. N. Argyriou. Flop of electric polarization driven by the flop of the Mn spin cycloid in multiferroic $\mathrm{TbMnO_3}$. *Phys. Rev. Lett.*, 102:207205, May 2009. doi: 10.1103/PhysRevLett.102.207205. URL https://link.aps.org/doi/10.1103/PhysRevLett.102.207205.

[87] T. Kimura, G. Lawes, and A. P. Ramirez. Electric polarization rotation in a hexaferrite with long-wavelength magnetic structures. *Phys. Rev. Lett.*, 94:137201, Apr 2005. doi: 10.1103/PhysRevLett.94.137201. URL https://link.aps.org/doi/10.1103/PhysRevLett.94.137201.

[88] K. Taniguchi, N. Abe, S. Ohtani, H. Umetsu, and T. Arima. Ferroelectric polarization reversal by a magnetic field in multiferroic Y-type hexaferrite $\mathrm{Ba_2Mg_2Fe_{12}O_{22}}$. *Applied Physics Express*, 1(3):031301, 2008. doi: 10.1143/APEX.1.031301. URL http://stacks.iop.org/1882-0786/1/i=3/a=031301.

[89] S. Ishiwata, Y. Taguchi, H. Murakawa, Y. Onose, and Y. Tokura. Low-magnetic-field control of electric polarization vector in a helimagnet. *Science*, 319(5870):1643–1646, 2008. ISSN 0036-8075. doi: 10.1126/science.1154507. URL http://science.sciencemag.org/content/319/5870/1643.

[90] Y. Tokunaga, Y. Kaneko, D. Okuyama, S. Ishiwata, T. Arima, S. Wakimoto, K. Kakurai, Y. Taguchi, and Y. Tokura. Multiferroic M-type hexaferrites with a room-temperature conical state and magnetically controllable spin helicity. *Phys. Rev. Lett.*, 105:257201, Dec 2010. doi: 10.1103/PhysRevLett.105.257201. URL https://link.aps.org/doi/10.1103/PhysRevLett.105.257201.

[91] K. Kimura, H. Nakamura, S. Kimura, M. Hagiwara, and T. Kimura. Tuning ferroelectric polarization reversal by electric and magnetic fields in $CuCrO_2$. *Phys. Rev. Lett.*, 103: 107201, Sep 2009. doi: 10.1103/PhysRevLett.103.107201. URL https://link.aps.org/doi/10.1103/PhysRevLett.103.107201.

[92] H. Yamaguchi, S. Ohtomo, S. Kimura, M. Hagiwara, K. Kimura, T. Kimura, T. Okuda, and K. Kindo. Spiral-plane flop probed by ESR in the multiferroic triangular-lattice antiferromagnet $CuCrO_2$. *Phys. Rev. B*, 81:033104, Jan 2010. doi: 10.1103/PhysRevB.81.033104. URL https://link.aps.org/doi/10.1103/PhysRevB.81.033104.

[93] U. Nowak and K. D. Usadel. Diluted antiferromagnets in a magnetic field: A fractal-domain state with spin-glass behavior. *Phys. Rev. B*, 44:7426–7432, Oct 1991. doi: 10.1103/PhysRevB.44.7426. URL https://link.aps.org/doi/10.1103/PhysRevB.44.7426.

[94] C. M. Soukoulis, Gary S. Grest, Charles Ro, and K. Levin. Irreversibility in diluted antiferromagnets. *Journal of Applied Physics*, 57(8):3300–3302, 1985. doi: 10.1063/1.335128. URL http://dx.doi.org/10.1063/1.335128.

[95] U. Daniel, B. Radu, and V. Nicolae. Photovoltaic performance of (Al, Mg)-doped $CuCrO_2$ for p-type dye-sensitized solar cells application. *Nanoscience and Nanotechnology*, 6(1A): 71–76, 2016. doi: 10.5923/c.nn.201601.14. URL http://article.sapub.org/10.5923.c.nn.201601.14.html.

[96] M. Han, K. Jiang, J. Zhang, W.i Yu, Y. Li, Z. Hu, and J. Chu. Structural, electronic band transition and optoelectronic properties of delafossite $CuCr_{1-x}Ga_xO_2$ $(0 \leqslant x \leqslant 1)$ solid solution films grown by the sol-gel method. *J. Mater. Chem.*, 22:18463–18470, 2012. doi: 10.1039/C2JM33027J. URL http://dx.doi.org/10.1039/C2JM33027J.

[97] D. Xiong, Q. Zhang, S. K. Verma, H. Li, W. Chen, and X. Zhao. Use of delafossite oxides $CuCr_{1-x}Ga_xO_2$ nanocrystals in p-type dye-sensitized solar cell. *Journal of Alloys and Compounds*, 662:374 – 380, 2016. ISSN 0925-8388. doi: https://doi.org/10.1016/j.jallcom.2015.12.044. URL http://www.sciencedirect.com/science/article/pii/S0925838815318351.

[98] E. Pachoud, K. Singh, Y. Bréard, C. Martin, G. André, V. Hardy, Ch. Simon, and A. Maignan. Magnetic dilution and steric effects in the multiferroic delafossite $CuCrO_2$. *Phys. Rev. B*, 86:054437, Aug 2012. doi: 10.1103/PhysRevB.86.054437. URL https://link.aps.org/doi/10.1103/PhysRevB.86.054437.

[99] T. Elkhouni, C. Colin, P. Strobel, A. Ben Salah, and M. Amami. Effect of Ga substitution on the magnetic state of delafossite $CuCrO_2$ with antiferromagnetic triangular sublattice. *Journal of Superconductivity and Novel Magnetism*, 26(6):2125 – 2134, 2013. ISSN 15571939. doi: 10.1007/s10948-012-1807-7.

[100] N. Metropolis, A. W. Rosenbluth, M. N. Rosenbluth, A. H. Teller, and E. Teller. Equation of state calculations by fast computing machines. *The Journal of Chemical Physics*, 21(6): 1087–1092, 1953. doi: 10.1063/1.1699114. URL http://dx.doi.org/10.1063/1.1699114.

[101] U. Nowak, R. W. Chantrell, and E. C. Kennedy. Monte carlo simulation with time step quantification in terms of langevin dynamics. *Phys. Rev. Lett.*, 84:163–166, Jan 2000. doi: 10.1103/PhysRevLett.84.163. URL https://link.aps.org/doi/10.1103/PhysRevLett.84.163.

[102] S. Kirkpatrick, C. D. Gelatt, and M. P. Vecchi. Optimization by simulated annealing. *Science*, 220(4598):671–680, 1983. ISSN 00368075, 10959203. URL http://www.jstor.org/stable/1690046.

[103] S. Kirkpatrick. Optimization by simulated annealing: Quantitative studies. *Journal of Statistical Physics*, 34(5):975–986, 1984. ISSN 1572-9613. doi: 10.1007/BF01009452. URL http://dx.doi.org/10.1007/BF01009452.

[104] A. M. Ferrenberg, D. P. Landau, and K. Binder. Statistical and systematic errors in monte carlo sampling. *Journal of Statistical Physics*, 63(5):867–882, 1991. ISSN 1572-9613. doi: 10.1007/BF01029988. URL http://dx.doi.org/10.1007/BF01029988.

[105] K. Binder and D. W. Heermann. *Monte Carlo Simulation in Statistical Physics*. Graduate Texts in Physics. Springer Berlin Heidelberg, 5 edition, 2010. ISBN 978-3-642-03163-2. doi: 10.1007/978-3-642-03163-2. URL http://www.springer.com/gp/book/9783642031625.

[106] D. W. Heermann. *Computer Simulation Methods in Theoretical Physics*. Graduate Texts in Physics. Springer-Verlag Berlin Heidelberg, 2 edition, 1990. ISBN 978-3-540-52210-2. doi: 10.1007/978-3-642-75448-7. URL http://www.springer.com/us/book/9783540522102.

[107] Ahmed Albaalbaky, Yaroslav Kvashnin, Denis Ledue, Renaud Patte, and Raymond Frésard. Magnetoelectric properties of multiferroic $CuCrO_2$ studied by means of *ab initio* calculations and Monte Carlo simulations. *Phys. Rev. B*, 96:064431, Aug 2017. doi: 10.1103/PhysRevB.96.064431. URL https://link.aps.org/doi/10.1103/PhysRevB.96.064431.

[108] A. I. Liechtenstein, M. I. Katsnelson, V. P. Antropov, and V. A. Gubanov. Local spin density functional approach to the theory of exchange interactions in ferromagnetic metals and alloys. *Journal of Magnetism and Magnetic Materials*, 67(1):65 – 74, 1987. ISSN 0304-8853. doi: http://dx.doi.org/10.1016/0304-8853(87)90721-9. URL http://www.sciencedirect.com/science/article/pii/0304885387907219.

[109] M. I. Katsnelson and A. I. Lichtenstein. First-principles calculations of magnetic interactions in correlated systems. *Phys. Rev. B*, 61:8906–8912, Apr 2000. doi: 10.1103/PhysRevB.61.8906. URL https://link.aps.org/doi/10.1103/PhysRevB.61.8906.

[110] H. Dreyssé. Electronic structure and physical properties of solids: the uses of the LMTO method. *Springer Berlin Heidelberg*, 535:148 – 167, 2000. ISSN 3540672389. doi: 10.1007/3-540-46437-9. URL http://archive.org/details/springer_10.1007-3-540-46437-9.

[111] Y. Ono, K. I. Satoh, T. Nozaki, and T. Kajitani. Structural, magnetic and thermoelectric properties of delafossite-type oxide, $CuCr_{1-x}Mg_xO_2$ $(0 \leqslant x \leqslant 0.05)$. *Japanese Journal of Applied Physics*, 46(3R):1071, 2007. doi: 10.1143/JJAP.46.1071. URL http://stacks.iop.org/1347-4065/46/i=3R/a=1071.

[112] T. Arnold, D. J. Payne, A. Bourlange, J. P. Hu, R. G. Egdell, L. F. J. Piper, L. Colakerol, A. De Masi, P. A. Glans, T. Learmonth, K. E. Smith, J. Guo, D. O. Scanlon, A. Walsh, B. J. Morgan, and G. W. Watson. X-ray spectroscopic study of the electronic structure of $CuCrO_2$. *Phys. Rev. B*, 79:075102, Feb 2009. doi: 10.1103/PhysRevB.79.075102. URL https://link.aps.org/doi/10.1103/PhysRevB.79.075102.

[113] D. O. Scanlon, A. Walsh, B. J. Morgan, G. W. Watson, D. J. Payne, and R. G. Egdell. Effect of Cr substitution on the electronic structure of $CuAl_{1-x}Cr_xO_2$. *Phys. Rev. B*, 79:035101, Jan 2009. doi: 10.1103/PhysRevB.79.035101. URL https://link.aps.org/doi/10.1103/PhysRevB.79.035101.

[114] A. Rohrbach, J. Hafner, and G. Kresse. Ab initio. *Phys. Rev. B*, 70:125426, Sep 2004. doi: 10.1103/PhysRevB.70.125426. URL https://link.aps.org/doi/10.1103/PhysRevB.70.125426.

[115] I. I. Mazin. Electronic structure and magnetism in the frustrated antiferromagnet $LiCrO_2$: First-principles calculations. *Phys. Rev. B*, 75:094407, Mar 2007. doi: 10.1103/PhysRevB.75.094407. URL https://link.aps.org/doi/10.1103/PhysRevB.75.094407.

[116] M. T. Czyzyk and G. A. Sawatzky. Local-density functional and on-site correlations: The electronic structure of La_2CuO_4 and $LaCuO_3$. *Phys. Rev. B*, 49:14211–14228, May 1994. doi: 10.1103/PhysRevB.49.14211. URL https://link.aps.org/doi/10.1103/PhysRevB.49.14211.

[117] A. G. Petukhov, I. I. Mazin, L. Chioncel, and A. I. Lichtenstein. Correlated metals and the $LDA + U$ method. *Phys. Rev. B*, 67:153106, Apr 2003. doi: 10.1103/PhysRevB.67.153106. URL https://link.aps.org/doi/10.1103/PhysRevB.67.153106.

[118] Y. O. Kvashnin, O. Grånäs, I. Di Marco, M. I. Katsnelson, A. I. Lichtenstein, and O. Eriksson. Exchange parameters of strongly correlated materials: Extraction from spin-polarized density functional theory plus dynamical mean-field theory. *Phys. Rev. B*, 91:125133, Mar 2015. doi: 10.1103/PhysRevB.91.125133. URL https://link.aps.org/doi/10.1103/PhysRevB.91.125133.

[119] T. Okuda, R. Kajimoto, M. Okawa, and T. Saitoh. Effects of hole-doping and disorder on the magnetic states of delafossite $CuCrO_2$ having a spin-3/2 antiferromagnetic triangular sublattice. *International Journal of Modern Physics B*, 27(05):1330002, 2013. doi: 10.1142/S0217979213300028. URL http://www.worldscientific.com/doi/abs/10.1142/S0217979213300028.

[120] S. Zagoulaev and I. I. Tupitsyn. Electronic structure and magnetic properties of the spin-peierls compound $cugeo_3$. *Phys. Rev. B*, 55:13528–13541, May 1997. doi: 10.1103/PhysRevB.55.13528. URL https://link.aps.org/doi/10.1103/PhysRevB.55.13528.

[121] J. M. Wills, O. Eriksson, M. Alouani, and D. L. Price. *Full-Potential LMTO Total Energy and Force Calculations*, pages 148–167. Springer Berlin Heidelberg, Berlin, Heidelberg, 2000. ISBN 978-3-540-46437-2. doi: 10.1007/3-540-46437-9_4. URL https://doi.org/10.1007/3-540-46437-9_4.

Normandie Université

THÈSE

Pour obtenir le diplôme de doctorat

Spécialité SCIENCES DES MATÉRIAUX

Préparée au sein de l'Université de Rouen-Normandie

Modeling of the magnetoelectric properties of anisotropic transition metal oxides

by

Ahmed Al Baalbaky

Abstract

Transition metal oxides are widely used due to their interesting fundamental properties and important applications. In particular, $CuCrO_2$ is of special interest because it enters the multiferroic state in zero magnetic fields. In this thesis we model the magnetoelectric properties of $CuCrO_2$ using Monte Carlo simulations with the help of *ab initio* calculations. We also investigate the effect of Ga doping on the magnetoelectric properties of $CuCr_{1-x}Ga_xO_2$ $(0 \leq x \leq 0.3)$. Our results are well comparable to the experimental observations.

Keywords: Multiferroic, proper-screw, spiral ordering, Monte Carlo simulations, spin glass.

Résumé

Les oxydes de métaux de transition sont largement utilisés en raison de leurs propriétés fondamentales intéressantes et de leurs applications importantes. En particulier, $CuCrO_2$ est d'un intérêt particulier parce qu'il possède un état multiferroïque en absence de champ magnétique. Dans cette thèse, nous modélisons les propriétés magnéto-électriques de $CuCrO_2$ par simulations Monte Carlo basées sur des paramètres magnétiques déterminés par calculs *ab initio*. Nous étudions également l'effet du dopage du Ga sur les propriétés magnéto-électriques du composé $CuCr_{1-x}Ga_xO_2$ $(0 \leq x \leq 0.3)$. Nos résultats sont qualitativement en accord avec les observations expérimentales.

Mots clés: Multiferroïque, ordre hélimagnétique, simulations Monte Carlo, verre de spin.

December 21, 2017.